MIKES

Applied Diode Laser Spectroscopy and Characterization of Optical Fiber Nonlinearity

Tuomas Hieta

Doctoral Dissertation
Aalto University, School of Electrical Engineering

Espoo 2011

Applied diode laser spectroscopy and characterization of optical fiber nonlinearity

Doctoral Dissertation

Tuomas Hieta

Abstract

This thesis describes work and progress on accurate nonlinearity measurements of optical fibers, design and characterization of external cavity diode lasers, and spectroscopic measurement of air temperature and humidity for accurate determination of the refractive index of air.

The first part of the thesis describes measurement of the nonlinear coefficient of standard and erbium-doped single-mode fibers, commonly used in telecommunications. A simulation tool was developed to model the previously neglected effects of dispersion in the continuous-wave self-phase modulation method. The simulation can be included in already existing measurement set-ups increasing their versatility and reducing their uncertainty. It is shown that reliable erbium-doped fiber nonlinearity measurements are possible even for very short fibers when the whole measurement system is carefully characterized for nonlinearity. With the help of the dispersion simulation and a carefully optimized fiber optic power measurement, an expanded uncertainty of 2.0 % (k =2) was achieved for the nonlinearity of a single-mode fiber. The Expanded uncertainty for measurement of an erbium-doped fiber was found to be 3.0 % (k =2).

Applied diode laser spectroscopy is covered in the second part of this thesis. External-cavity diode laser based on non-dispersive holographic volume grating was designed and characterized in this work. The use of a non-dispersive element for feedback eliminates beam directional variations and enables compact design with good wavelength reproducibility. Laser designs for applications in metrology, molecular spectroscopy and for multicomponent absorption spectroscopy were developed.

This thesis describes accurate measurement of temperature and humidity using diode laser spectroscopy, which is crucial for refractive index compensation in demanding interferometric length measurements. The measurement system was tested both in laboratory and outdoor environment successfully over distances up to 130 m. The standard deviation of temperature measurement in laboratory environment was 7 mK using a 120 s sample time, which is the best spectroscopic value ever reported. Performance of the system was found to be excellent when a commercial interferometer was compensated in an environment with local temperature variations, demonstrating the suitability of the method for industrial dimensional measurements. A portable and robust temperature measurement set-up was developed for long-distance geodetic applications. The set-up was tested successfully in harsh outdoor conditions.

Tiivistelmä
Tässä väitöskirjassa kuvatussa tutkimustyössä on keskitytty luotettaviin ja tarkkoihin valokuidun epälineaarisuusmittauksiin, ulkokaviteettilasereiden karakterisointiin, ja ilman lämpötilan ja kosteuden mittaamiseen ilman taitekertoimen määrittämiseen laser-spektroskopian avulla.

Väitöskirjan ensimmäisessä osassa käsitellään tietoliikenteessä käytettyjen yksimuotokuitujen ja erbium-seostettujen kuitujen epälineaarisen kertoimen mittaamista. Työssä kehitetyllä simulointityökalulla voidaan mallintaa ongelmallisen kuitudispersion vaikutuksia mittaukseen käytettäessä yleistä itseisvaihemodulaatioon perustuvaa mittaustapaa. Simulointityökalua voidaan käyttää jo olemassa olevien mittausjärjestelmien rinnalla lisäämään niiden monikäyttöisyyttä ja pienentämään mittausepävarmuutta. Työssä osoitetaan, että jopa erittäin lyhyiden erbium-seostettujen kuitujen epälineaarisuuden mittaus on mahdollista, kun koko mittausjärjestelmän epälineaarisuus on tarkasti karakterisoitu. Simuloinnin ja tarkan tehomittauksen avulla yksimuotokuidun mittausepävarmuudeksi saatiin 2.0 % ($k = 2$). Erbium-seostetun kuidun mittausepävarmuus on 3.0 % ($k = 2$).

Väitöskirjan toinen osa käsittelee sovellettua laser-spektroskopiaa. Holografiseen volyymihilaan perustuva ulkokaviteettilaser suunniteltiin ja karakterisoitiin osana väitöskirjatyötä. Ei-dispersiivisen hilan käyttö takaisinkytkentäelementtinä poistaa säteen ulostulosuunnan vaihtelun ja mahdollistaa kompaktin rakenteen käytön toistettavalla aallonpituudella. Työssä tutkittuja lasereita voidaan hyödyntää useissa mittaustekniikan ja molekyylispektroskopian sovelluksissa, ja monikomponentti-spektroskopiassa.

Väitöskirjatyön viimeisessä osassa esitetään mittausjärjestelmä, jolla voidaan mitata diodilaser-spektroskopian avulla ilman lämpötila ja kosteus, mikä on välttämätöntä jotta ilman taitekerroin voidaan kompensoida vaativissa pituusmittauksissa. Järjestelmä testattiin onnistuneesti laboratoriossa ja ulkona mittausmatkan ollessa jopa 130 m. Lämpötilamittauksen keskihajonnaksi mitattiin 7 mK käyttäen 120 sekunnin mittausaikaa, mikä on tiettävästi paras ikinä raportoitu tulos käyttäen spektroskopisia menetelmiä. Järjestelmän käytännöllinen suorituskyky paikallisten lämpötilavaihteluiden kompensoimiseen havaittiin erittäin hyväksi interferometrisissä pituusmittauksissa, mahdollistaen järjestelmän käytön myös vaativissa teollisuussovelluksissa. Työssä esitetty geodeettisiin sovelluksiin suunniteltu kannettava, ja rakenteeltaan yksinkertaisempi järjestelmä, testattiin ulkona hankalissa olosuhteissa 240 metrin matkalla.

Preface

The research work presented in this thesis has been carried out at the Centre for Metrology and Accreditation (MIKES) and at the Metrology group of Aalto University.

I am most grateful to my supervisor, Professor Erkki Ikonen, for his guidance from the very beginning to the very end.

I am very grateful to my instructor, Dr. Mikko Merimaa, for excellent support and encouragement during my time in MIKES. It has been a privilege to work with such a passionate researcher and relentless problem solver. I want to thank Dr. Ville Ahtee for valuable discussions on a daily basis while sharing an office during my time in MIKES. Dr. Heikki Isotalo and Dr. Antti Lassila are thanked for the possibility to carry out research and project development at MIKES Metrology. Dr. Kaj Nyholm and Jere Seppä are thanked for their scientifical and non-scientifical contribution.

My special thanks goes to Dr. Markku Vainio for co-authoring, experimental help, sharing a room, fruitful discussions, off-work activities, etc. Your impact on this work has been most valuable.

From Metrology group I would like to thank Dr. Farshid Manoocheri, Dr. Petri Kärhä, Dr. Jouni Envall, Dr. Maija Ojanen, Meelis Sildoja, Petteri Ahonen, Ilkka Kotamäki, Juhana Lano, Marko Laurila and Ari Kesänen for scientific contribution and for keeping it real! Special thanks goest to Dr. Antti Lamminpää for guidance in the very early stages of my work when I did not know much about anything.

Dr. Ilkka Salomaa, Dr. Timo Rajamäki and Mika Mänttäri from Gasmet Technologies are thanked for their patience.

I also acknowledge my co-authors Dr. Chris Moser, Dr. Florian Pollinger, Dr. Karl Meiners-Hagen, Dr. Nicolae R Doloca and Dr. Ahmed Abou-Zeid.

The preliminary examiners of the thesis, Dr. Jan Petersen and Dr. Juha Toivonen, are highly appreciated for their efforts.

The financial support by the Finnish Cultural Foundation and Jenny and Antti Wihuri Foundation is greatly appreciated.

I would like to thank my friends and family for their support throughout my studies. Mega special acknowledgement for their love and support goes to my wife Leila and our newborn Tessa!

Espoo, November 2011

Tuomas Hieta

Errata

Publication IV "Spectroscopic measurement of air temperature"

p. 1712, paragraph after Eq. 3

"The third term in Eq. 2" should be " The third term in Eq. 3".

Contents

List of Publications

This thesis consists of an overview and the following publications.

I. A. Lamminpää, T. Hieta, J. Envall and E. Ikonen, "Reliable determination of optical fiber nonlinearity using dispersion simulations and improved power measurements," IEEE J. Lightwave Tech. **25**, 527-532 (2007).

II. T. Hieta and E. Ikonen, "Measurement of Er-doped fiber nonlinearity using continuous-wave self-phase modulation method," IEEE J. Lightwave Tech. **27**, 2977-2982 (2009).

III. T. Hieta, M. Vainio, C. Moser and E. Ikonen, "External-cavity lasers based on a volume holographic grating at normal incidence for spectroscopy in the visible range," Opt. Commun. **282**, 3119-3123 (2009).

IV. T. Hieta and M. Merimaa, "Spectroscopic measurement of air temperature," Int. J. Thermophys. **31**, 1710-1718 (2010).

V. T. Hieta, M. Merimaa, M. Vainio, S. Seppä and A. Lassila, "High-precision diode-laser-based temperature measurement for air refractive index compensation," Appl. Opt. **50**, 5990-5998 (2011).

VI. F. Pollinger, T. Hieta, M. Vainio, N.R. Doloca, A. Abou-Zeid, K. Meiners-Hagen and M. Merimaa, "Effective humidity in length measurements: comparison of three approaches," MIKES Report J1/2011.

Author's contribution

All publications included in the thesis are results of team work. The author has prepared the manuscripts for Publications II, III, IV and V.

In the work reported in Publication I the author has been responsible for the measurements done and for the development of the simulation environment. He has also analyzed all the measurements presented in this publication.

In the work reported in Publication II the author has done all the measurements, simulations and data analysis presented in this publication.

The author has designed and characterized the device presented in Publication III. He has carried out and analyzed most of the measurements presented in this publication.

In the work presented in Publications IV, V and VI the author was involved in the planning of the project, made most of the measurements except those measured outdoor at the Nummela baseline of the Finnish Geodetic Institute (FGI). He also was responsible for all of the simulations and analyzed all the measurements presented in these publications expect for the measurement related to the PTB set-up.

1 Introduction

1.1 Background

Accurate and reliable measurements are the crucial in characterization and commercialization of novel products and technologies. As the requirements for the manufactured components are becoming more and more stringent, the margin for error is diminishing. Costly operational failures are directly proportional to high uncertainty in each component in a complex system involving various components. Therefore it is crucial to be able to characterise individual components and complete measurement systems accurately and reliably. Standardisation is a time consuming process that involves many steps. Before the process can even start, there must be reproducible methods available that are traceable to known physical phenomena, or more preferably to the international system of units (SI).

In telecommunications, the transition from high loss copper cables to silica fibers has been very rapid and today the use of optical fibers to provide reliable, high data rate long-haul transmission is a well-established standard. The cornerstones of the optical telecommunications systems are all-optical erbium-doped fiber amplifier (EDFA) and wavelength division multiplexing (WDM) that were invented already over two decades ago [1,2,3]. Though the achievable capacity is enormous compared to competing technologies, there are still many limiting factors preventing the use of the full potential of the optical fiber. A straightforward way to meet the requirements for ever increasing demand for higher bandwidth is to use more channels with narrower wavelength spacing or to use more power to get better signal-to-noise ratio. Unfortunately both of the mentioned methods increase the total optical power in the fiber, thus resulting in degradation of the system performance mainly due to nonlinearities [4,5]. Without knowing the magnitude of the nonlinear effect which is caused by the intrinsic properties of the silica fiber, the effects of the nonlinearities to the system performance are impossible to predict.

One of the key parameters in evaluation of the magnitude of the nonlinear effects is the nonlinear coefficient (n_2/A_{eff}), where n_2 is the nonlinear refractive index and A_{eff} is the effective area of the fiber. A reliable method to determine the nonlinear coefficient was introduced already over a decade ago for a standard single-mode telecom fiber [6]. Since then many laboratories have done measurements of the nonlinear coefficient of a fiber, but the agreement between the laboratories has been far from acceptable. One possible reason can be dispersion effects which were not taken into account in these measurements.

Since the demonstration of the first ruby laser in 1960 [7], lasers and especially diode lasers have been widely used for example in metrology, communications and spectroscopy in both commercial and scientific applications. The popularity of diode laser arises from ease of use, compactness, reliability, and relatively low price. A common laser diode is a p-n junction semiconductor that converts external injection current into emitted photons through stimulated emission process. Although the properties of a solitary diode lasers are fairly good, many applications need better performance usually in a form of spectral purity and accurate tunability. So called external-cavity diode lasers (ECDL) use frequency selective optical feedback from an external grating to improve spectral properties [8,9,10]. Antireflection coated diode with strong optical feedback results in single-mode operation and much narrower linewidth and enable wide mode-hop free tuning range, which is ideal e.g. for spectroscopy. With respect to tunability, weather it is for frequency locking of a laser to an atomic or molecular transition in metrology, operating inside a limited wavelength window in WDM system or probing the right transition in molecular spectroscopy, ECDLs are far superior compared to solitary laser diodes.

Dimensional measurements are an essential part of fundamental metrology. Accurate dimensional measurements are crucial for industry, research and international trade. In addition to product manufacturing, also product development and quality control, both in micro- and macro-scale require accurate dimensions. Refractive index of a medium, usually air, must be known accurately in length measurements, because the length scale is derived from the speed of light. Parameter-based Edlen and Ciddor equations are

conventionally used to calculate the refractive index of air and can reach an uncertainty in the 10^{-8}-range [11,12,13]. Parameters affecting the refractive index of air include temperature, pressure, water vapour concentration, and CO_2 concentration. At short distances, the ambient conditions affecting the refractive index can be measured accurately. However, when measuring over long distances in non-homogenous environment e.g. in industrial or outdoor environment, local variations especially in temperature can cause significant error in the measured distance [14]. Sophisticated schemes have been developed to measure the effective temperature along the beam path, ranging from methods based on dispersion [15,16,17], over acoustic density measurements [18] up to spectroscopic temperature measurements [19,20,21].

1.2   Thesis outline

The first research topic of the thesis is covered in Chapter 2 where, measurement of fiber nonlinearity is briefly reviewed. The effects of dispersion to the commonly used continuous-wave self-phase modulation (CW-SPM) method to determine the nonlinearity of a standard single-mode fiber (SMF) are described in Publication I. It is shown that the effects of dispersion can be difficult to estimate a priori and can cause a significant error if not taken into account. A simulation tool based on Nonlinear Schrödinger Equation (NLSE) was developed to study effects of dispersion to propagation of optical signals in a fiber. The NLSE is a nonlinear partial differential equation that does not have analytical solutions except for some special cases. Therefore, numerical approach is often necessary to model nonlinear effects in optical fibers. In this work split-step Fourier method was used to evaluate the NLSE. The method obtains an approximate solution by assuming that dispersive and nonlinear effects act independently over a small propagation distance.

Chapter 2 also summarizes the work done at Metrology Research Institute in Aalto University to determine the nonlinearity of an amplifying erbium-doped fiber, which is described in Publication II. As compared to the measurement of a standard SMF, where the fiber length is usually hundreds of meters, the length of the erbium-doped fiber must be significantly shorter because of the high attenuation. First, the erbium-doped fiber

must be modelled to be able to distinguish which part of the signal is originating from the nonlinearity and what is the contribution of the amplification. The erbium-doped fiber was tested both in pumped amplifying mode and in passive mode with no pump. Due to the complex nature of amplifying operation of erbium-doped fiber, the measurement was done in passive mode for a fiber length of only a few meters. It is shown that the CW-SPM method together with careful characterization of the erbium-doped fiber can be used to determine the nonlinearity accurately using standard laboratory equipment.

Chapter 3 is devoted to external cavity diode lasers. After a brief outlook of the fundamental properties of diode lasers, the chapter focuses on spectral properties of diode lasers especially from a practical spectroscopic point of view. Two laser designs using volume holographic gratings as their feedback elements are presented in Publication III. Conventionally the strong feedback required for proper laser operation is obtained from a reflection grating. Littrow configuration is probably the most commonly used configuration to provide optical feedback due to its simplicity. The wavelength selection is done by adjusting the angle of the grating, which also unfortunately affects the beam direction. The use of a novel non-dispersive volume holographic grating at normal incidence overcomes this problem. The first design, operating around 635 nm, utilizes a long cavity designed for narrow linewidth and good long-term stability. It has a mode-hop free tuning range of 28 GHz making it suitable for e.g. multicomponent spectroscopy. The grating in the second design is positioned very close to the laser diode making it compact and robust. It has a mode-hop free tuning range of 145 GHz near 658 nm.

Chapter 4 describes a work done at MIKES in the field of applied laser spectroscopy. The goal of the research was to design, build and characterize a laser based system capable of measuring ambient temperature and humidity over a long distance to compensate the refractive index of air required in dimensional measurements. The system can be used jointly with an interferometer with very good spatial and temporal overlap.

The concept of laser based thermometer is presented in Publication IV. Two transitions from the oxygen A-band were used for the thermometer designed to measure average air temperature. Two distributed feedback (DFB) lasers were used as sources operating around 762 nm. Ambient temperature can be determined from the ratio of two absorption peaks for a limited temperature range near 293 K. The measurement results over 67 m path length are well within the accuracy required to reduce the relative uncertainty originating from ambient temperature below a level of 10^{-7}.

An integrated spectroscopic system measuring both temperature and humidity was developed for effective compensation of the refractive index of air. An improved temperature set-up, humidity measurement set-up and measurements performed to characterize and demonstrate the system performance are given in Publications V and VI. The lowest reported root-mean-square (RMS) noise of 7 mK was demonstrated in laboratory for 67 m path length using a sample time of 120 s. Further, it was demonstrated that an interferometric length measurement can be effectively compensated when rapid and local temperature variations are induced, a situation that was found to be impossible to compensate with an ensemble of conventional temperature sensors. The system was also tested in outdoor environment over broader temperature range. To reach the lowest possible uncertainty level, the effects of ambient temperature and pressure to the linewidth were taken into account, which is crucial when measuring broad temperature variations. In addition, humidity measurements and the effects of humidity to the compensation and measurement both in indoor and outdoor environment are discussed in this chapter. Finally, a design for a simplified spectroscopic thermometer is described and results of long distance outdoor measurements are presented.

1.3 Scientific contribution

This thesis contains the following new scientific results:

1. A fiber dispersion model for CW-SPM method nonlinearity measurements was successfully implemented. The new model developed in this work allows quantification of the effects of dispersion, thus reducing measurement uncertainty.

2. The nonlinearity of a very short amplifying erbium-doped fiber is measured using the conventional CW-SPM method and standard laboratory equipment. Criteria for fiber length and input power enabling measurement uncertainty close to that of a standard single-mode fiber are presented.

3. A new ECDL design is presented using non-dispersive volume holographic grating at normal incidence to provide optical feedback. The constructed ECDL has a tuning range suitable for spectroscopy, and it does not suffer from beam pointing problems as compared to conventional Littrow configuration ECDLs.

4. A system for average ambient temperature and relative humidity determination is presented to compensate the refractive index of air over a long path. The achieved temperature resolution is to our knowledge the best ever reported. The system was used to effectively compensate laser interferometric dimensional measurements in challenging environment and it was found to be applicable also to measurements done in outdoor environment. A portable and more robust temperature sensor designed and validated for long distance measurement is also presented.

2 Fiber nonlinearity measurements

Various nonlinear phenomena can occur in optical fibers giving rise to either harmful or beneficial effects. There are two categories of nonlinear effects. Nonlinear effects originating due to the dependence of the refractive index on the intensity of the electric field are in the first category. The second category of nonlinear effects comprises of two phenomena resulting from the interaction of light with phonons. The most important nonlinear effects in the first category are self-phase modulation (SPM), four-wave mixing (FWM) and cross-phase modulation (XPM).

2.1 Optical fiber nonlinearities

Self-phase modulation occurs when high-intensity pulses propagate in long fibers. In SPM, the nonlinear refractive index causes an induced phase shift that is proportional to the intensity. Different parts of the pulse undergo different phase shifts, which leads to pulse broadening [22]. Four-wave mixing gives rise to new signals due to interaction of three signals at different frequencies. The effect can be extremely harmful in WDM systems with equal channel spacing [23]. In a WDM system all the channels contribute to the total intensity inside the fiber. The effect of other channels to the phase shift of one particular channel is referred as XPM [24].

When the interaction occurs between light and acoustic phonons, the optical scattering phenomenon is referred as stimulated Brillouin scattering (SBS). More complex interaction between the light and optical phonon is referred as stimulated Raman Scattering (SRS). Both of these phenomena can be practically neglected if the power level is kept below a threshold level [25].

2.2 Nonlinear refractive index

A conventional optical fiber used in telecommunications is almost entirely made of SiO_2. Dopants, such as GeO_2, Al_2O_3 and Er, are used to alter the refractive index or to

provide amplification. At low optical power levels, the interaction between the fiber material and the electric field can be assumed linear. The response of any dielectric material to light becomes nonlinear for intense electromagnetic fields. The total polarization **P** depends upon the applied optical field **E** according to [5]

$$\mathbf{P} = \varepsilon_0 \left(\chi^{(1)} \cdot \mathbf{E} + \chi^{(2)} \cdot \mathbf{E} \cdot \mathbf{E} + \chi^{(3)} \cdot \mathbf{E} \cdot \mathbf{E} \cdot \mathbf{E} + \ldots \right), \tag{1}$$

where ε_0 is the vacuum permittivity and $\chi^{(j)}$ ($j = 1,2,\ldots$) is the jth order susceptibility. Dominant contributor to the total polarization is the linear susceptibility $\chi^{(1)}$. The linear part of the refractive index n and the absorption coefficient α are related to the real and imaginary parts of the linear susceptibility, respectively. Nonlinear optical phenomena that originate from the second-order susceptibility $\chi^{(2)}$ include second-harmonic generation, sum-frequency generation and difference-frequency generation to name a few. These phenomena arise from the lack of inversion symmetry of the material. As SiO_2 is a symmetric molecule, $\chi^{(2)}$ vanishes for silica glasses.

Third-order susceptibility $\chi^{(3)}$ is responsible for most of the nonlinear effects in the fiber as discussed earlier in this chapter. The nonlinear refractive index is related to the third-order susceptibility by the relation

$$n_2 = \frac{3}{8n} \operatorname{Re}\left(\chi^{(3)}_{xxxx} \right), \tag{2}$$

where Re stands for the real part and the optical field is assumed to be linearly polarized so that only one component of the fourth-rank tensor contributes to the refractive index. The intensity dependence of the refractive index is commonly formulated as

$$n = n_0 + n_2 I = n_0 + \left(\frac{n_2}{A_{\mathrm{eff}}} \right) P, \tag{3}$$

where the first part is the wavelength dependent linear part of the refractive index and A_{eff} is the effective area of the optical fiber that has originally been defined for the purposes of calculating nonlinear effects in a fiber. The nonlinear coefficient is defined as n_2/A_{eff}.

Most equation governing nonlinear effects found in literature use so called nonlinear parameter γ to express nonlinearity, which is related to the nonlinear refractive index as

$$\gamma = \frac{n_2 \omega_0}{c_0 A_{eff}},$$ (4)

where ω_0 is the angular frequency and c_0 is the speed of light in vacuum.

Effective area of the fiber must be known accurately to be able to determine the nonlinear refractive index. The effective area is required to due to non-uniform distribution of the intensity inside the fiber. The effective area is defined as

$$A_{eff} = \frac{2\pi \left(\int\limits_0^\infty I(r) r dr \right)^2}{\int\limits_0^\infty I(r)^2 r dr},$$ (5)

where $I(r)$ is the intensity of the optical field at radius r from the fiber axis.

The problem with the effective area is that it is not commonly directly measured for a fiber [26]. Another parameter describing the distribution of the intensity of the optical field is mode field diameter (MFD) [27,28]. It is used to evaluate e.g. splice loss and bending loss and it is usually measured for each fiber [26]. In conventional step-index fibers the intensity distribution is well approximated by a Gaussian function and the effective area can be calculated using the MFD. For different types of fibers this approximation is not valid. MFD can be used to calculate the effective area by using a widely used Namihira correction factor that has been defined for various types of fibers [29,30]. Fortunately, the same techniques that are used to determine the MFD can be also used to determine the effective area, since both parameters require the knowledge of the near field [26]. Most common technique for determining the near field distribution is a far field scanning technique, where the near field is calculated from the far field using an inverse Hankel transform [26,31,32].

It should be noted that in Publication II, the effective area is calculated without the Namihira correction factor, which will induce some error. The reported value for the nonlinear coefficient in Publication II should be increased by 3-4% when the correction factor recommended by the International Telecommunication Union (ITU) is applied [33].

2.3 Light propagation in nonlinear fiber using numerical methods

Different nonlinear effects, namely SPM, FWM and XPM, originating from the nonlinear refractive index of the fiber are usually indistinguishable in a WDM system where channels are packed closely. Such system is governed by Maxwell's equations. Using certain approximations, a general Nonlinear Schrödinger Equation (NLSE) describing light propagation in an optical fiber can be derived [5]. In its simplest form, the NLSE can be written as

$$i\frac{\partial A}{\partial z} + \frac{i\alpha}{2}A - \frac{\beta_2}{2}\frac{\partial^2 A}{\partial T^2} + \gamma|A|^2 A = 0 ,$$ (6)

where A is the envelope of the electric field such that $|A|^2$ is equal to the optical power. T is retarded time variable defined as

$$T = t - \beta_1 z ,$$ (7)

where t is time, β_1 is the first order propagation constant and z is the distance along the propagation axis. Parameter β_2 is the second order propagation constant or so called group-velocity dispersion (GVD) parameter. It is related to the derivatives of refractive index and to the widely used dispersion parameter D [5] through relation

$$\beta_2 = \frac{1}{c_0}\left(2\frac{dn}{d\omega} + \omega\frac{d^2 n}{d\omega^2}\right) = -D\frac{\lambda^2}{2\pi c_0} ,$$ (8)

where λ is the wavelength of the light.

The NLSE in a more general form includes also terms related to Raman scattering [34], self-steepening [35] and higher order derivatives of the propagation constant [36]. For long pulses of width $T_0 > 5$ ps, these terms can be neglected.

Generally, a numerical approach is necessary to solve Eq. 6, as it does not have analytical solutions except for some special cases. Split-step Fourier method which belongs to the category of pseudospectral methods is accurate and fast, making it one of the most commonly used method to solve the NLSE. Equation 6 can be divided into differential operator $\hat{D}$ that accounts for dispersion and absorption and to nonlinear operator $\hat{N}$ that governs the effects of nonlinearities. These operators are given by

$$\hat{D} = -\frac{i\beta_2}{2}\frac{\partial^2}{\partial T^2} - \frac{\alpha}{2}, \tag{9}$$

$$\hat{N} = i\gamma|A|^2, \tag{10}$$

Using these operators, the NLSE can be written in the form

$$\frac{\partial A}{\partial z} = \left(\hat{D} + \hat{N}\right)A. \tag{11}$$

The split-step Fourier method (SSFM) assumes that the two operators act independently over a small distance Δz, which means that the propagation is done in two steps. The accuracy of the SSFM can be improved by adopting a different procedure to propagate the optical pulse over one segment from z to $z + \Delta z$. Mathematically this is expressed as

$$A(z + \Delta z, T) \approx \exp\left(\Delta z\hat{D}\right)\exp\left(\Delta z\hat{N}\right)A(z, T). \tag{12}$$

The operator $\hat{D}$ can be evaluated in Fourier domain, which makes computations relatively fast. A trade-off between computational speed and accuracy must be made when choosing the step size. The accuracy of the SSFM can be improved by adopting different procedures to propagate the optical pulse over one segment [5].

The numerical approximation of NLSE using SSFM was implemented using MATLAB software. The developed software was used to simulate the effects of dispersion when using the CW-SPM method to determine the nonlinear coefficient of standard single-mode fibers of different lengths.

2.4   Erbium doped fiber characteristics

Erbium-doped fiber is undoubtedly one of the key elements in modern telecommunication networks. Without erbium-doped fiber amplifiers (EDFAs) the internet as we know it would not exist. An erbium-doped fiber can be used as a light amplifier if population inversion in erbium-ions is achieved when pumped with higher energy photons. A simple erbium doped fiber amplifier can be built from a piece of erbium doper fiber, a pump source, which is usually a diode laser, and from a coupler that combines the two [2,3]. With this all-optical amplifier, it is possible to amplify several channels within the ~40 nm amplification band of an common EDFA simultaneously without affecting the properties of the signal significantly. The EDFAs operate around 1550 nm, which is very close to the region where telecom fibers have their loss minimum. This makes the EDFA by far the most important fiber amplifier especially in telecom applications. Another commonly used optical amplifier in telecommunication network is Raman amplifier. Raman amplifiers enable distributed amplification, which is especially important in long-haul and ultralong-haul fiber networks [37].

Compared to a standard 2-level or 3-level systems, the operational principle of EDFA is different due to Stark-split energy levels [38]. Rather than having discrete energy levels as in typical laser system, the energy levels of EDFA are essentially continuums, yielding a broad amplification band [39]. Three energy levels of Er^{3+} ions in silica glass host crystal are shown in Fig. 1. The $^4I_{13/2}$ metastable state is the initial level for the transition producing wideband gain around 1550 nm. This state is directly available using 1480 nm pump. Another commonly used pump wavelength is 980 nm, which excites Er^{3+} ions from their ground level $^4I_{15/2}$ to the $^4I_{11/2}$ level. The population density at level $^4I_{11/2}$ is fairly low due to its short lifetime. Even if the 980 nm pump wavelength

is used, the system can be closely approximated as a two-level system due to the fast nonradiative decay from level $^4I_{11/2}$ to level $^4I_{13/2}$ [40].

$\tau_0 \approx 1\ \mu s$

$^4I_{11/2}$

$\tau_0 \approx 10\ ms$

$^4I_{13/2}$

980 nm   1480 nm   1520 nm–
1570 nm

$^4I_{15/2}$
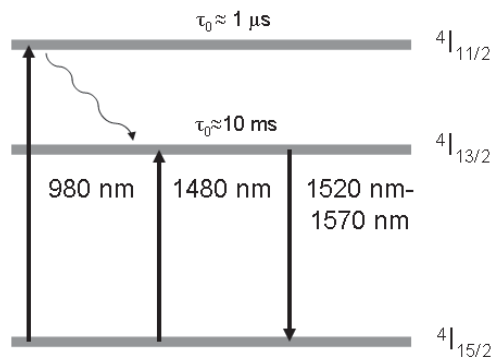
Figure 1. Schematical illustration of the three most important energy levels of Er^{3+} ions in silica glass.

An extensive scientific effort has been given to accurately model erbium-doped fibers and fiber amplifiers. Consequently, a wide variety of symbols, notations, assumptions, approximations, and experimental data are used [39]. One of the simplest solutions to the complex problem is based on two parameters that can be determined from monochromatic absorption data [41]. The model predicts signal gain and absorption at each wavelength bin k using absorption constant α_k and intrinsic saturation power P_k^{IS}.

2.5   Continuous-wave self-phase modulation method

Continuous-wave self-phase modulation (CW-SPM) method for measuring the nonlinear coefficient of optical fibers was introduced in 1996 [6]. It is likely the most commonly used method to measure fiber nonlinearity [42,43]. The naming of the method is arguably ambiguous. The same principle could be viewed also as four-wave mixing method [44,45]. The reason for the naming is probably due to the measurement setup presented in a paper published partly by the same authors around the same time [46]. In general SPM and FWM can be considered as different phenomena, but they originate form the same source, the nonlinear refractive index. Therefore in both cases

the nonlinear refractive index can be deduced from the results using NLSE as in Publications I and II.

In addition to CW-SPM and FWM methods, there are also various other methods available. Self-phase modulation method using pulsed laser (P-SPM) has been used since 1978 to determine the nonlinear refractive index of an optical fiber [47,48,49]. In the XPM, method the nonlinearity is deduced from the phase shift caused by high power signal to the weak probe signal [50]. Modulation instability (MI) can also be used to determine n_2 based on dispersion by measuring the generated spectral sidebands in time domain [51]. In addition, methods using interferometers have also been presented [52,53]. Contrary to the measurement of standard fibers where the fiber lengths are normally from 100 m up to 1 km, the measurement of an erbium-doped fiber has to be made using a relatively short fiber because of the high losses. A novel method based on induced grating autocorrelation (IGA) has shown the greatest promise for accurate measurement of erbium-doped fibers [54]. However, comparisons have shown that no method is clearly superior compared to others and consequently, no standard method is recommended by the International Telecommunication Union (ITU) [33,42].

In this work the CW-SPM method has been used to measure the nonlinear coefficient of an erbium-doped fiber. The strength of CW-SPM is in its simplicity; it can be implemented with standard laboratory equipment. The measurement set-up used in Publication I is shown in Fig. 2. Two continuous-wave external-cavity diode lasers are operated around 1550 nm with wavelength spacing around 0.3 nm. The laser beams are set to have the same linear polarization using polarization controllers and a polarizer after the beams are combined. The signal is then amplified using commercial EDFA and launched into the fiber under test (FUT). The optical power is measured with integrating sphere (ISP) detector at the end of the FUT using the 99% branch of the coupler. Optical spectrum analyzer (OSA) after an attenuator at the 1% branch of the coupler is used to measure the spectrum. Splices were used between the FUT and the ISP to minimize uncertainty. The total attenuations of the coupler, splice connection, and tested fiber are taken into account by carefully characterizing their attenuation as well as the reflection from the fiber end. The uncertainty related to splice loss was estimated to

be ~0.03 dB (~0.7%) for the erbium doped fiber and ~0.01 dB for the single-mode fiber. The splice loss measurement for the erbium doped fiber showed good correlation between the estimates from the fusion splicer and the measured values with a small offset that needed to be added to the estimated splice loss.
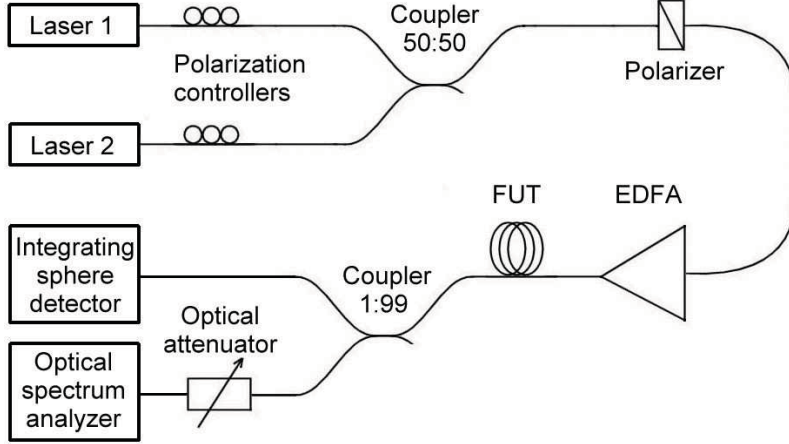
Figure 2. Continuos-wave self-phase modulation method measurement setup. [Publication I].

Equation 13 shows how the nonlinear phase shift φ_{SPM} (in radians) is related to the ratio of the intensity of the first sideband I_1 to the intensity of the fundamental wavelength I_0 [6],

$$\frac{I_1}{I_0} = \frac{J_1^2(\varphi_{SPM}/2) + J_2^2(\varphi_{SPM}/2)}{J_0^2(\varphi_{SPM}/2) + J_1^2(\varphi_{SPM}/2)}, \tag{13}$$

where J_n is the Bessel function of nth order. Using only the first order factors from the Taylor expansion, Eq. 13 can be expressed more illustratively for small φ_{SPM}.

$$\frac{I_1}{I_0} \cong \frac{\varphi_{SPM}^2}{16}. \tag{14}$$

The nonlinear coefficient can then be determined from the linear relation

$$\varphi_{SPM} = \frac{2\omega_0}{c_0} \frac{n_2}{A_{eff}} L_{eff} P_{AVG}, \tag{15}$$

where L_{eff} is the effective fiber length, and P_{AVG} is the average optical power of the dual-frequency beat signal. The fiber length L is related to the effective length by

$$L_{\text{eff}} = \frac{1 - e^{-\alpha L}}{\alpha},$$ (16)

where α is the absorption coefficient of the fiber.

For a standard single-mode fiber with a loss of 0.2 dB/km ($\alpha \approx 0.046$ 1/km), the effective lengths for 500 m and 1000 m fibers are 494 and 977 m, respectively. However, in the case of an erbium doped fiber, the effective length can differ significantly from the actual length even for a short fiber due to much higher attenuation as shown in Publication II.

A typical spectrum of the CW-SPM measurement is shown in Fig. 3. The nonlinear coefficient is conventionally determined by fitting the φ_{SPM} deduced from the measured spectra at different optical input powers to Eq. 15.

A typical fiber does not maintain its polarization due to small imperfections in the core and in the cladding. All the equations presented in this chapter assume a linear polarization state, which is not true in even short fibers. By assuming a random polarization along the fiber, a coefficient of 8/9 is found to be accurate for single-mode fibers [55]. The process in which the material density increases in response to the intensity of an applied optical field is called electrostriction. Therefore, increased light intensity will increase the nonlinear refractive index in the same manner as the nonlinear susceptibility [56]. Electrostriction can be measured directly using external electric field and its contribution to the total nonlinearity in typical single-mode fiber is around 20% [56,57]. The measured values of nonlinear refractive index presented in Publications I and II are for random polarization and they include the contribution from the electrostriction.
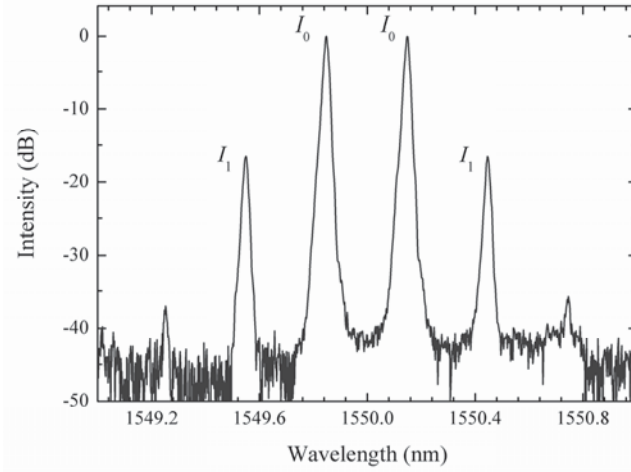
Figure 3. Optical spectrum of the SPM generated first and second order sidebands. The fundamental signals are separated by 0.3 nm from each other.

2.6 Effects of dispersion

The original CW-SPM method omits the effects of dispersion [6]. It has been shown that this can cause a measurement error of several percent, depending on the measurement conditions [43,58]. Fiber length, used wavelength spacing and optical power are required to determine the optimal area for the measurement. The simulated effect of fiber dispersion using NLSE and SSFM on nonlinear phase shift curves based on Eq. 15 is shown in Fig. 4 for three different values of dispersion parameter. The zero dispersion case corresponds to the standard CW-SPM measurement. It is evident that the dispersion has a significant effect on the nonlinear phase shift especially at high power levels even in a standard single-mode fiber.
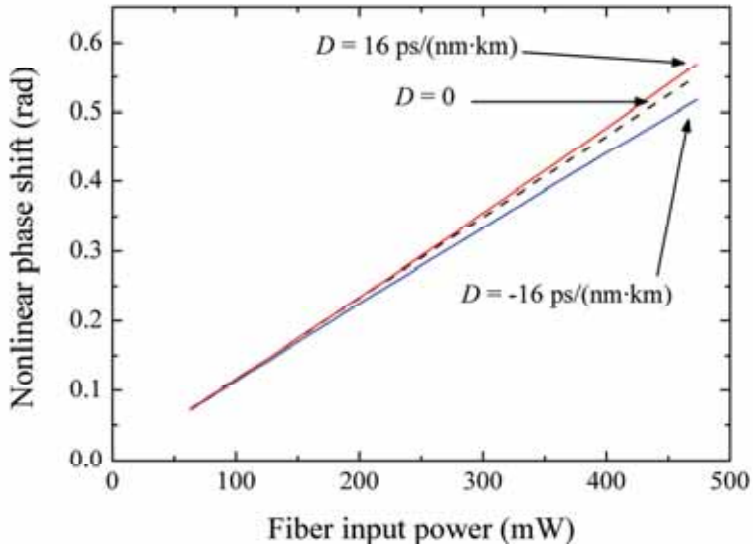
Figure 4. Simulated effects of dispersion on nonlinear phase shift. In all simulations, fiber length was set to 500 m, wavelength difference to 0.3 nm. [Publication I].

Physically more feasible solution to the dispersion problem can be achieved by combining NLSE simulation to the measurement data presented in Publication I thus taking dispersion into account. An example of 500 m standard single-mode fiber measurement using the dispersion model is shown in Fig. 5. The measured phase shift as a function of input power is marked with crosses and the fit based using least-squares method is shown in green. If the value for nonlinear coefficient obtained from the fit is used to estimate the nonlinear phase curve according to Eq. 15, marked by black line in the Fig. 5, an error of several percent is possible. Without using the dispersion simulation, the value of the nonlinear coefficient would be overestimated by approximately 2.3 %.
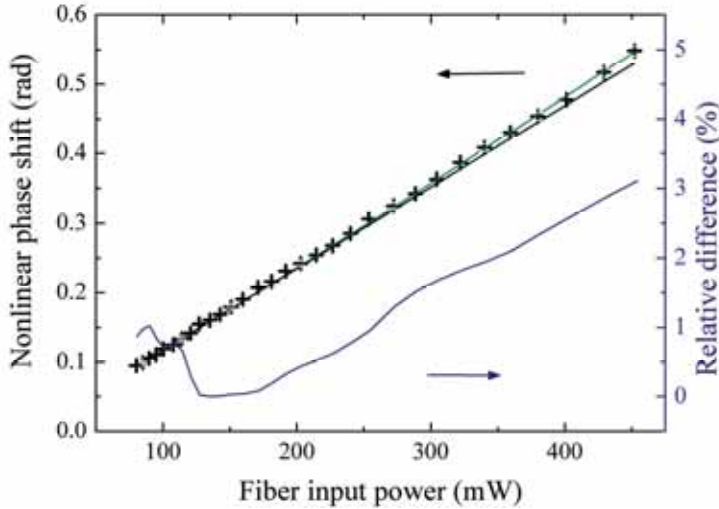
Figure 5. Relative difference (blue line) between the nonlinear phase shift determined using the dispersion simulation tool (green line) and by using the value obtained from the fit and the conventional linear model (black line). Crosses represent the measured nonlinear phase shift as a function of fiber input power. [Publication I].

The major source of uncertainty in determination of fiber nonlinearity is usually uncertainty in the measurement of fiber optic power [58]. An elegant way to accurately and reliably measure high fiber optic powers is to use integrating sphere (ISP) detectors that have uniform angular responsivity over wide solid angle [59,60]. The ISP can be considered as an angle-independent attenuator which enables measurement of high fiber optic power with conventional photodiodes. By using this approach, the fiber optic power is not restricted anymore to low powers. In general it is beneficial to use high power levels to increase the signal-to-noise ratio of the measurement. In order to extend the fiber optic power scale, the linearity of the existing sphere was studied using the ac/dc method [59,61]. The nonlinearity of the ISP detector is shown in Fig. 6. The expanded uncertainty (k=2, 95% confidence interval) for the developed fiber nonlinear coefficient measurement configuration including the dispersion simulation is 2.0 %. The total power measurement uncertainty of 1.5 % (k=2), which includes the uncertainty of the coupler and the splice between the FUT and the ISP, remains the dominant uncertainty component in the measurement configuration.
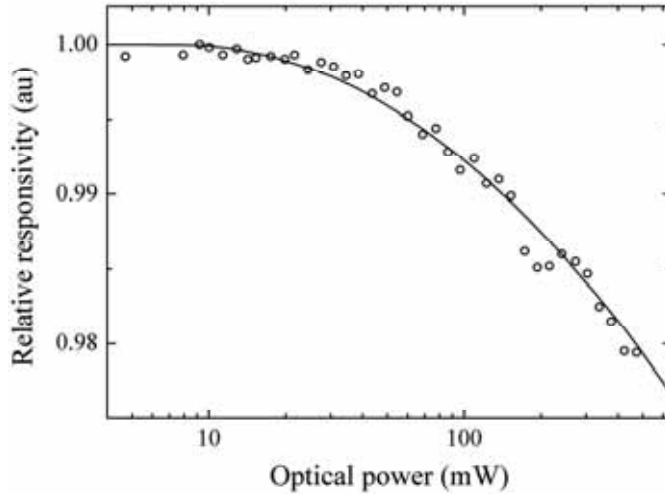
Figure 6. Second order polynomial fit to the measured relative responsivity values (circles) of the integrating sphere detector at high power levels. [Publication I].

2.7   Erbium-doped fiber measurements

As indicated in Publication II, the original goal was to use the erbium-doped fiber as an amplifier and use CW-SPM to determine the nonlinear coefficient from the amplified sidebands. An accurate model of the fiber gain characteristics is required to identify which part of the sideband signal is caused by the fiber nonlinearity and which part is amplified. Although the fiber was characterized carefully using reliable power sensors [59], good agreement with the experimental data and the simulations was not found. This is due to two reasons. First, spectral hole burning in erbium-doped fibers was not taken into account [62]. Spectral hole burning is not well characterized in erbium-doped fibers and it depends on gain compression. It would be therefore very difficult to map it along the fiber length. Another problematic phenomenon is pump-induced nonlinear refractive index change [63]. Both of these phenomena are difficult to model accurately and consequently, a more straightforward approach was adopted. In this work, nonlinearity of an erbium-doped fiber was measured in passive mode i.e. without using a pump signal.

In Publication II, the erbium-doped fiber operation in passive mode was estimated based on the fraction of the measured signal power to the total optical power. This fraction was determined from the measured broadband spectra at different fiber lengths. Figure 7 shows sample broadband spectra after 8 m and 16 m of erbium-doped fibers marked with red and black lines, respectively. The main difference between the two spectra is the increase of amplified spontaneous noise (ASE) at longer wavelengths. This is caused by the absorption of signal power and ASE at short wavelengths as in L-band EDFAs [64,65]. Based on these considerations, the maximum fiber length was limited to 8 m, which is estimated to be short enough to avoid significant amplification of CW-SPM signals.
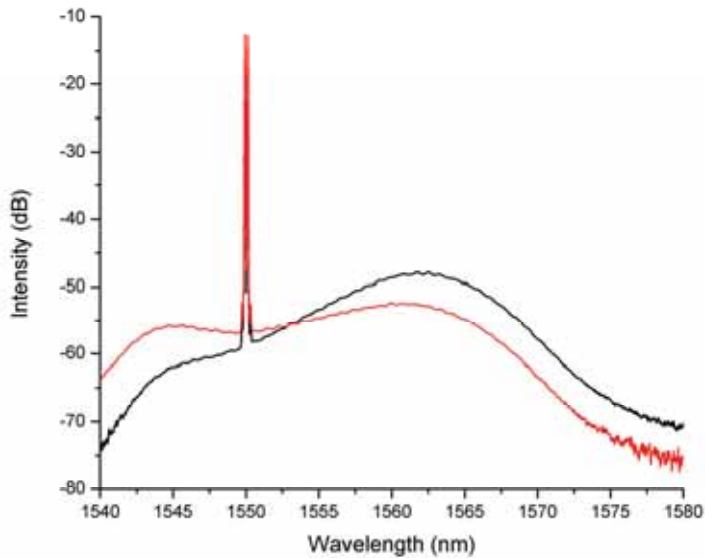
Figure 7. Broadband spectra of signals and ASE after erbium doped fiber. The erbium-doped fiber lengths were 8m and 16m, which are marked with red and black lines, respectively.

When measuring the nonlinear phase shift of a very short fiber it is crucial to characterize all the components in the set-up, which could affect the results. In Publication II, the total measured phase shift φ_{TOT} was split in to three components according to

$$\varphi_{\text{TOT}} = \varphi_{\text{SYS}} + \varphi_{\text{FUT}} + \varphi_{\text{END}}, \tag{17}$$

where the φ_{SYS} included all the contribution before the FUT, φ_{FUT} is the contribution of the FUT and φ_{END} consist of the contribution between the FUT and the 1:99 coupler. The φ_{FUT} can be determined by varying the fiber length, thus eliminating the contribution from the φ_{SYS} and the φ_{END}.

The nonlinear contribution of the erbium-doped fiber nonlinearity measurement system is essentially the same as the measurement system that was used to measure standard single-mode fibers. Therefore, the values for nonlinear coefficients presented in Publication I are approximately 3 % higher for the 500 m fibers and approximately 1.5 % higher for 1000 m fibers. This difference appears because the nonlinear contribution of the measurement system is omitted in Publication I. It is not possible to evaluate the exact magnitude of the effect, since the fiber after the FUT and 1:99 coupler was not measured at the time of the single-mode fiber measurements. The expanded uncertainty (k=2) for the erbium-doped fiber measurement configuration is 3.0 %, which is higher compared to the standard single-mode fiber measurement configuration mainly because of the lower signal-to-noise ratio in the sideband intensity measurement.

The developed simulation tool and the characterised ISP for high fiber optic powers in this work enable accurate fiber nonlinearity measurements using CW-SPM of various single-mode fibers without restrictions in fiber length, used power or wavelength spacing. It is shown that the widely used CW-SPM method using standard laboratory equipment can be adopted also in erbium-doped fiber measurements enabling high accuracy. By being able to characterize accurately the nonlinearity of both standard single-mode fibers and erbium-doped fibers, it is possible to model the existing telecommunication network even more accurately resulting in more efficient operation.

3 External-cavity diode lasers for molecular spectroscopy

The impact of lasers on spectroscopy can hardly be overestimated. Most of our knowledge about structure of atoms and molecules is based on spectroscopy. Compared to incoherent light sources, lasers represent intense light sources with much higher spectral intensities. Another superior characteristic is their narrow bandwidth, which allows the investigation of molecules and atoms in more detail. Since the first demonstration of laser action in ruby in 1960 [7], several types of lasers have been developed, including dye lasers, gas lasers, fiber lasers, solid-state lasers, and semiconductor diode lasers.

3.1 Diode laser characteristics

Semiconductor lasers or diode lasers are arguably the most widely used type of laser because of their robustness, compactness, good efficiency, tunability and low price. Lasing in diode lasers, as in any other laser, requires a gain mechanism and a resonant cavity. A diode laser is essentially a p-n junction semiconductor device. When positive bias is applied to the p-type material and negative bias to the n-type material, electrons from the n-type region drift to the p-type region. When this so called forward bias is equal to the potential gap of the semiconductor, an active region is created within the junction. Stimulated emission occurs due to electron-hole recombination in this region. At low bias currents, the optical radiation from the semiconductor originates from spontaneous emission thus being incoherent and broadband. When the current is increased, laser operation begins at the wavelength of the highest gain. The cavity in semiconductor material can be simply formed by cleaving both facets. Reflectance at the semiconductor-air interface is sufficiently high due to the high refractive index of a typical semiconductor material [66].

Both the active region and the laser mode are confined within the same region in a modern index-guided heterostructure design [67]. The active area thickness and width are usually in a range of micrometers, the width being wider than the thickness. This

small non-symmetric structure results in highly diverging output beam with an elliptical shape. The linewidth of the laser is fundamentally limited by fluctuations in phase due to spontaneous emission, which will lead to a Lorentzian line shape [68]. The resulting full width at half maximum (FWHM) linewidth Δv_0 can be calculated using the modified Schawlow-Townes formula [69]

$$\Delta v_0 = \frac{\pi h v_0 (\Delta v_c)^2}{P_i} n_s \left(1 + \alpha_{enh}^2\right),$$ (18)

where h is the Planck's constant, v_0 is the center frequency of the laser, Δv_c is the cold cavity linewidth, P_i is the intra-cavity power, n_s is the spontaneous emission factor and α_{enh} is the linewidth enhancement factor. The spontaneous emission factor n_s results from absorption and re-emission of laser photons in the semiconductor. A typical value for semiconductor materials is around 2.5 [69].

The gain of the medium is affected by the carried density, which will vary due to spontaneous emission. The fluctuations of gain will cause variations in the refractive index according Kramers-Kronig dispersion relation [70], which will lead to change of the phase that results in broadened linewidth described by the factor $(1 + \alpha_{enh}^2)$. The linewidth enhancement factor depends on the semiconductor material and on several parameters related to the structure of the laser diode. A typical value for α_{enh} varies from 2 to 8 [70]. The cold cavity linewidth Δv_c is related to the photon lifetime t_c according to [8]

$$\Delta v_c = \frac{1}{2\pi\tau_c} = \frac{c}{2\pi n_d L_d} \left(\alpha_d L_d - \ln\sqrt{R_1 R_2}\right),$$ (19)

where n_d is the refractive index of the cavity medium, L_d is the length of the cavity medium, α_d included for the optical losses in the cavity and R_1 and R_2 are the power reflectivities of the front and rear facets of the diode, respectively. The calculated linewidth Δv_0 for a typical laser diode is usually several MHz [8]. In practice, the Lorentzian linewidth calculated using Eq. 18 is broadened by various mechanisms. The extrinsic noise sources include current source noise, temperature noise, and acoustic noise, which result in a Gaussian line shape [71].

3.2   Diode lasers with optical feedback

Spectral purity and tuneability of a solitary diode laser are generally insufficient for spectroscopy. A typical diode laser operates in multiple longitudinal modes with varying power distribution due to mode competition. Tuning of a solitary diode by either varying its injection current or by changing the temperature will lead to mode-hops that are hysteretic and not accurately reproducible. Fortunately, optical feedback enables accurate wavelength tuning using an externally controlled feedback element.

The effect of optical feedback to the diode laser depends strongly on the strength and phase of the feedback. Five clearly distinguishable operational regimes have been characterized [72]. The fifth regime is the regime of the highest feedback. In this regime the laser operates as a long cavity laser with short active region. By using a wavelength selective element in the cavity, single-mode operation can be achieved with narrow linewidth as the number of photons in the lasing mode is increased. This kind of diode laser configuration is commonly referred as external-cavity diode laser (ECDL).

The cold cavity linewidth given by Eq. 19 can be applied to ECDLs by assuming that the reflectivity of the facet of the emissive end of the diode (R_2) is zero, according to

$$\Delta v_{\text{ECDL,c}} = \frac{c}{2\pi(n_d L_d + L_e)}\left(\alpha_d L_d - \ln\sqrt{R_1 R_3}\right),$$ (20)

where L_e is the length of the external cavity and R_3 is the power reflectivity of the external feedback element. The linewidth reduction in an ideal ECDL is according to Eqs. 18-20 given by

$$\frac{\Delta v_{\text{ECDL}}}{\Delta v_0} = \left(\frac{\Delta v_{\text{ECDL,c}}}{\Delta v_c}\right)^2,$$ (21)

where Δv_{ECDL} is the linewidth of the ECDL. In practice, the linewidth can be reduced by a factor of more than 1000 [73].

The most common ECLD uses diffractive grating as the feedback element [8,71,73,74,75]. Various other elements such as mirrors [76], acousto-optic modulator filters [77], and liquid crystal arrays [78] have also been used as the wavelength

selective element. The motivation behind using an acousto-optic modulator or liquid crystal is the possibility to tune the wavelength selection electronically instead of mechanically turning the grating. Most ECLD designs are based on either Littrow [8,74] or Littman-Metcalf configuration [73,79]. These two designs are schematically shown in Fig. 8. Littrow configuration is simpler compared to Littman-Metcalf configuration, which has an extra mirror. However, the Littrow configuration suffers from beam direction variation when the ECDL is tuned by adjusting the angle of the diffraction grating. Use of an additional mirror in Littman-Metcalf configuration eliminates this problem but adds complexity in the structure. Another way to overcome the output beam pointing problem is to use a transmission grating in the Littrow configuration [80]. If the wavelength is tuned by only rotating the diffraction grating, the mode defined by the cavity length remains fixed, which will lead to mode-hops. To obtain broad mode-hop free tuning range, the angle and the position of the diffraction grating must be synchronously varied to match the lasing mode of the cavity and the dispersion curve of the grating. In practice, the wavelength is tuned by using a combination adjustment screws for roughly setting the right wavelength and piezoelectric transducers (PZT) for fine tuning.
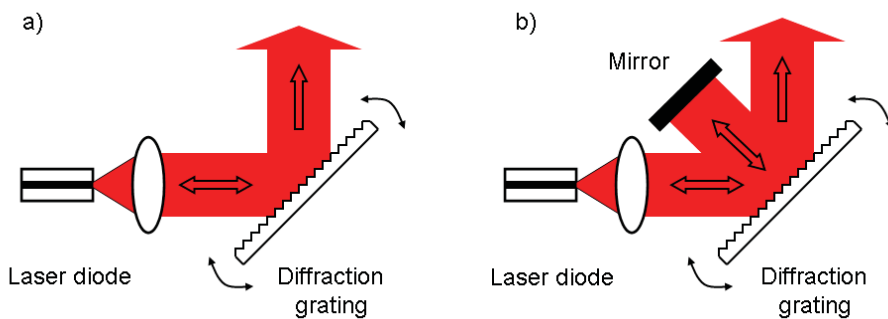

Figure 8. External-cavity diode laser (a) in Littrow configuration and (b) in Littman-Metcalf configuration.

Accurate wavelength tuning characteristics can be achieved also by using integrated optical feedback elements. Distributed feedback (DFB) lasers [66] have a periodic

variation in their gain medium. Wavelength tuning in DFB lasers is done by adjusting the current and/or the temperature, which cause thermal expansion and variations in the refractive index. Current tuning, which primarily affects the refractive index, is preferred at high frequencies due to fast response. Temperature tuning is often used to find the correct wavelength, because of its wider tuning range. The grating in DFB lasers is constructed so as to reflect only a narrow band of wavelengths, and thus produce a single longitudinal lasing mode. The DFB lasers are widely used in scientific and commercial applications, including the work presented in publication IV, V and VI, due to their robustness and good spectral properties. Distributed feedback lasers are available roughly from 750 nm up to 2.8 μm. A variant of the DFB laser is the Distributed Bragg reflector (DRB) laser in which the gain medium and the distributed reflector are separated [81]. In this way the wavelength and the output power can be controlled independently. However the tuning range of an ECDL is potentially much wider compared to a typical DFB laser and even 240 nm tuning range has been demonstrated in the visible wavelength region [82]. This, combined with the narrow linewidth, motivates the use of ECDLs in spectroscopic applications.

3.3 External-cavity lasers based on a volume holographic grating at normal incidence

Most of the reported ECDL geometries lead to a large mechanical structure, which makes the laser susceptible to acoustic and mechanical vibrations, thermal expansions and thermal gradients. In publication III, we present a novel ECDL configuration based on a volume holographic grating (VHG). Volume holographic grating was used already in 1985 to provide wavelength selective feedback to a diode laser [83]. Recent advances in material technology have enabled production of stable and compact VHGs that have found applications in frequency stabilization of lasers [84,85,86]. A typical VHG is essentially a Bragg grating [87] manufactured by recording the interference pattern of two coherent light fields into a thick photosensitive media. Photosensitive glasses are available from 350 nm to 2500 nm covering both visible and near infra-red wavelength regions.

As compared to diffraction grating that angularly spreads the incoming spectrum, the VHG diffracts only wavelengths satisfying the Bragg condition. One of the most important parameters of VHGs and diffraction gratings is their spectral resolution. Unlike diffraction gratings, whose resolution is inversely proportional to the beam diameter, the resolution of a VHG is inversely proportional to the interaction length [88]. The principle of the novel ECDL developed in this work, the "long-cavity ECDL" and an alternative design of Ref. [84], the "short-cavity ECDL", are schematically shown in Fig. 9. The strength of the designs lies in their simplicity, making very compact ECDL designs possible.
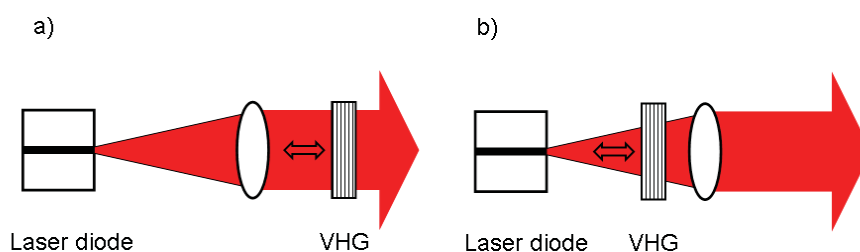
Figure 9. Schematic drawings of the operation principles of the ECDLs. The volume holographic grating (VHG) provides strong feedback for the collimated beam in long-cavity design (a), while in short-cavity design (b), the Bragg condition is satisfied only for a small portion of the beam perpendicular to the VHG.

The detailed structure of the long-cavity design is shown in Fig. 10. To ensure stable performance, the laser cavity is designed to be robust, rigid and symmetrical with respect to the optical axis. The diode laser, which is not shown in Fig. 10, is a commercially available antireflection-coated InGaAlP device with an AR-coated front facet with low reflectance. The nominal power and the nominal wavelength of the laser diode are 10 mW and 635 nm, respectively. Both ECDLs use similar VHG manufactured by Ondax Inc. having a reflectance around 35 %. The thickness of the VHGs is 1.5 mm, corresponding to a nominal reflection bandwidth (FWHM) of 75 GHz. Since the output beam is transmitted through the VHG, beam pointing is always parallel to the output beam of the laser diode, independent of the VHG angle. The lateral displacement of the output beam as a function of the VHG angle is

approximately 0.47 μm/mrad. The actual displacement in our design is negligible since the tilting angle around normal incidence is limited to some tenths of a mrad. It is worth noting that the diffraction efficiency of a conventional diffraction grating depends on the light polarization and the laser diode orientation has to be adjusted accordingly or a half-wave plate must be put inside a laser cavity. In comparison, the reflectance of a VHG is polarization independent at normal incidence, thus eliminating this problem [89].
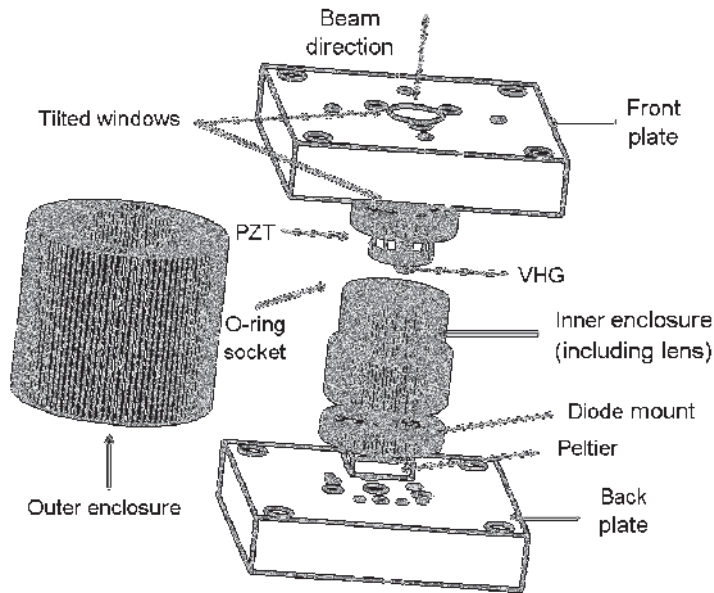
Figure 10. Exploded view of the long-cavity ECDL structure. All the components are in scale. [Publication III].

Passive stability of the long-cavity design was evaluated by measuring both the short-term and long-term frequency stability. Practical 1-s linewidth of 900 kHz was measured using a Fabry–Perot interferometer (FPI) as a frequency discriminator. To determine the long-term stability of the free running laser, the laser frequency was tuned to the linear part of the slope of an iodine absorption line at low pressure that was used as a frequency-to-amplitude converter. An 8-hour measurement done in a temperature controlled laboratory showed good passive long-term stability with the maximum deviation of the laser frequency being only 80 MHz. The linewidth of the short-cavity

ECDL is around 30 MHz measured by scanning FPI, which is due to the very short cavity length. Typical side-mode suppression ratios (SMSR) of both lasers were 35 dB. Continuous and mode-hop free tuning range of 28 GHz was achieved for the long-cavity ECDL, demonstrating that synchronous tuning of the ECDL cavity length and grating angle works well also with VHGs despite their non-dispersive nature. The total tuning range of the long-cavity ECDL was found to be 70 GHz, which is in agreement with the 75 GHz bandwidth of the VHG. A mode-hop free tuning range of 145 GHz was achieved with the short-cavity ECDL by varying the laser temperature.

The novel ECDL design developed in this work using VHG at normal incidence had good passive stability and narrow linewidth, making it suitable for various applications in molecular spectroscopy. It was shown that non-dispersive VHG can be used in a simple tunable ECDL design with practically fixed output beam direction as a function of wavelength tuning.

4 Air refractive index compensation using laser spectroscopy of oxygen and water

Refractive index of air must be known accurately in optical length measurements, as the length scale is derived from the speed of light. Ambient temperature and humidity are the most important parameters required for accurate determination of air refractive index based on parametric equations. Spectroscopy is a complicated tool and therefore strong motivation is required for its use in temperature and humidity measurements. Ambient parameters are easily measured and can be considered stable over a short distance. However, when measuring over long distances in industrial or outdoor environment, local and rapid variations in ambient parameters are likely to occur. The use of spectroscopic temperature and humidity measurement allows good spatial and temporal overlap with the actual dimensional measurement, making it a feasible choice compared to conventional sensor networks.

4.1 Absorption spectroscopy theory

The Beer-Lambert law is the fundamental equation that relates the transmitted intensity I to the dimensionless optical depth τ and to the initial intensity I_0, according to

$$I = I_0 e^{-\tau}. \tag{22}$$

For a single transition at frequency $v_{\eta\eta'}$ between lower and upper states η and η', the optical thickness for a gas at pressure p, temperature T, and at frequency v, is calculated as [90]

$$\tau_{\eta\eta'}(v,T,p) = u\,S_{\eta\eta'}(T)\,f(v,v_{\eta\eta'},T,p) = u\,k_{\eta\eta'}(v,T,p), \tag{23}$$

where $S_{\eta\eta'}$ is the line intensity, f is the normalized line profile function, $k_{\eta\eta'}$ is the monochromatic absorption coefficient and u is the number density of absorbing molecules per unit path length. Various notations for the fundamental parameters used

in absorption spectroscopy are found in literature [19,20,91] and there is even a discrepancy between the notations used in Publications IV and V. The notation as used by Rothman et al. [90] is adopted here that is compatible with the newest HITRAN 2008 database [92], which is used for calculations in the Publications IV, V and VI.

It should be noted that the absorption path length is not explicitly given in Eq. 23. To obtain the transmission given by Eq. 22, the optical thickness must be multiplied by the path length. The monochromatic absorption coefficient $k_{\eta\eta'}$ is the product of normalized line profile function and the line intensity. The line profile function, which is characterised by line halfwidth γ, is in general affected by both Doppler and pressure broadening. Doppler broadening is characterized by a Gaussian line profile and pressure broadening by a Lorentzian line profile.

The Lorentzian profile without the transition dependent pressure shift δ is defined as

$$f\left(v, v_{\eta\eta'}, T, p\right) = \frac{1}{\pi} \frac{\gamma(p,T)}{\gamma(p,T)^2 + \left(v - v_{\eta\eta'}\right)^2} . \tag{24}$$

The Doppler profile is defined as

$$f\left(v, v_{\eta\eta'}, T\right) = \frac{1}{\gamma_D(T)\sqrt{\pi}} e^{-\left(\frac{v - v_{\eta\eta'}}{\gamma_D(T)}\right)^2} , \tag{25}$$

where the FWHM Doppler-width in frequency units (Hz) can be directly calculated according to [93]

$$\gamma_D(T) = 7.16 \cdot 10^{-7} v_{\eta\eta'} \sqrt{T/M} , \tag{26}$$

where M is the molar mass.

The actual line profile is obtained as a convolution of these two [93], which results in a Voigt line profile. The normalized (area = 1) Lorentzian, Gaussian and Voigt line profiles of equal halfwidths are shown in Fig. 11. In the lower atmosphere the oxygen and water line profile functions are dominated by Lorentzian profiles. To reduce algorithmic complexity, we have used an approximate solution [94] for Voigt line

profile in spectral simulations and convoluted solution in all calculations in this thesis. The effect of collisional, or Dicke, narrowing was investigated using a Galatry line profile in the calculations [95,96]. The effect was found insignificant when compared to the results obtained using the convoluted Voigt profile.
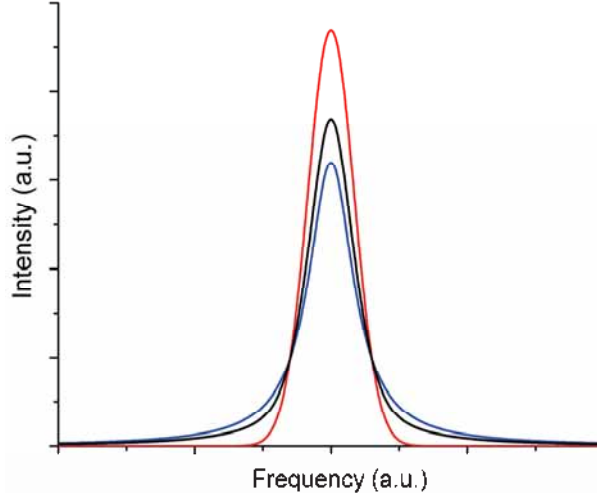
Figure 11. The normalized Gaussian (red), Lorentzian (blue) and Voigt (black) line profiles of equal halfwidths.

The line halfwidth γ is a function of temperature, pressure, collisions between similar molecules called self-broadening γ_{self}, collisions between the molecules in surrounding air γ_{air} described as air-broadening and partial pressure p_s according to [90]

$$\gamma(p,T) = \left(\frac{T_{ref}}{T}\right)^n \left(\gamma_{air}(p_{ref},T_{ref})(p - p_s) + \gamma_{self}(p_{ref},T_{ref})p_s\right), \quad (27)$$

where n is the transition specific empiric coefficient of temperature, where the reference pressure p_{ref} is 1 atm (101.3 kPa) and T_{ref} is the reference temperature (296 K). The self-broadened width of water is approximately five times larger than the air-broadened width for the used water transition in the humidity measurements. The absolute humidity can be determined from the number density using ideal gas law.

4.2 Spectroscopic thermometry

The line intensity of a transition is affected by the Boltzmann distribution of population among the initial states [97]. Therefore, it is possible to deduce the gas temperature from the measured transition line intensity. The temperature dependent line intensity $S_{\eta\eta'}(T)$ can be calculated from the tabulated line intensity at reference temperature $S_{\eta\eta'}(T_{ref})$ according to [90]

$$S_{\eta\eta'}(T) = S_{\eta\eta'}(T_{ref}) \frac{Q(T_{ref})}{Q(T)} \exp\left(-\frac{hcE_\eta}{k}\left(\frac{1}{T} - \frac{1}{T_{ref}}\right)\right) \left(\frac{1 - \exp\left(\frac{-hc\nu_{\eta\eta'}}{kT}\right)}{1 - \exp\left(\frac{-hc\nu_{\eta\eta'}}{kT_{ref}}\right)}\right), \quad (28)$$

where $Q(T)$ is the total internal partition sum, E_η is the lower state energy, h is the Planck constant, k is the Boltzmann constant and c is the speed of light. The third term in Eq. 28 accounts for the ratio of Boltzmann populations between temperature T and the reference temperature T_{ref}, and the last term for the effects of stimulated emission, which is negligible at visible wavelength region.

Although, the temperature can be determined directly using Eq. 28, most laser based temperature measurements are based on the measurement of intensity ratio of two absorption lines [19,20,21,98,99,100]. The ratio measurement is especially useful, when measuring gaseous compounds with varying concentration. In addition, this approach eliminates all errors that affect the absorption of individual transitions in similar manner. The path length independent ratio of line intensities of two transitions is given by [19,20]

$$R = R_0 \exp\left[-\frac{hc\Delta E}{k}\left(\frac{1}{T} - \frac{1}{T_{ref}}\right)\right], \quad (29)$$

where ΔE is the difference in their lower state energies and R_0 is the ratio of S_1 and S_2 at a reference temperature.

The simplest method to obtain line intensity for a single transition would be to measure over the whole absorption feature and integrate the area. The area is equal to the line

intensity, because the line profile function is normalized to unit area. In theory, thermometry using the whole absorption feature is relatively easy, since broadening effects do not affect the area of the normalized line profile function. Other solution would be to fit Voigt profile to the measured absorption feature and use thus obtained Voigt line profile parameters to calculate the total area. Unfortunately we were unable to achieve low uncertainty using Voigt fitting approach in our very early tests. We aimed at real-time analysis and used pure Lorentzian and approximate Voigt profiles [94], which explain the problems. We chose another approach in which only the peak absorption and baseline are measured. In this approach, the ambient temperature and pressure affect the relative contributions of the Gaussian and Lorentzian components in the Voigt line profile, which changes the peak value of the line profile function as discussed in Publication V. Both the temperature and pressure will have significant effects on the measured values if not taken into account in high accuracy thermometry.

We report also on a test done using a simplified set-up based on a measurement of a single oxygen transition using a single DFB laser. To achieve low uncertainty, absorption over the whole line profile has to be measured and fitted to a Voigt line profile to obtain accuracy in the 100 mK range. The parameters obtained from the Voigt fit are used to calculate the monochromatic absorption coefficient $k_{\eta\eta'}$, which is related to the temperature through Eqs. 23 and 28. It is necessary to know also the absorption path length l and partial pressure of oxygen, which depends on the varying water content of air.

4.3   Line selection of oxygen and water transitions based on HITRAN simulations

An obvious choice for a database for obtaining oxygen and water transition in air at normal temperature and pressure conditions is the widely adopted comprehensive HITRAN database [101]. Simulation program based on HITRAN 2008 database was developed in this work to find the optimal transitions and the positions for baseline measurement in temperature and humidity measurements. It can be used to simulate absorption spectra of one or multiple molecules tabulated in the HITRAN database.

Parameters such as species concentration, ambient pressure, ambient temperature, path length and resolution can be adjusted for various applications. The program is implemented using MATLAB software.

The program was used in all the simulations presented in Publications IV, V and VI. It has also been used e.g. in the mid infra-red region to verify the photoacoustic spectroscopy measurements of methane [102].

Selection of a line pair or multiple transitions for thermometry and humidity measurements is not trivial. Much of the research on optical thermometry has been focused on combustion applications at elevated temperatures. Water vapor is one of the most important hydrocarbon combustion products making its transitions an obvious choice for thermometry in combustion process measurements [19,21,98,99,100,103,104]. Oxygen has also been used in thermometry in similar applications [20,105,106].

Optimal line selection depends on whether only one laser is used or if it is possible to multiplex two or more lasers to the same absorption path. Additional lasers add complexity and price, but also improve the achievable sensitivity. In practice, the line selection is limited by the availability of laser sources. DFB lasers are commonly used especially in the near-infrared region. Absorbance of the two lines should be comparable and the transmission over the desirable path length should be in the ideal case e^{-1} ($\approx$37 %) based on Eq. 22 for two lines of equal strength and by assuming that the noise in independent of path length. If the absorbance is higher, saturation decreases the achievable temperature sensitivity. At low absorbance levels, noise becomes a significant degrading factor to the overall performance. Within the tuning range of the used diode(s), there should be a free spectral window ideally with zero absorbance, which could be used to provide baseline information on internal losses and non-idealities of the system. Based on simulations, free spectral windows are practically nonexistent at ambient conditions when the medium is standard air, but there are still regions where the absorbance is low enough to allow measurement of the baseline with low uncertainty.

For the measurement of the refractive index of air, water would be a convenient choice for thermometry, since only one line pair would be sufficient to measure both the temperature and the humidity of the air. The most critical parameter in determining the refractive index of air is ambient temperature, as discussed in Publication V. Compared to water, which has multiple strong features in visible and near infra-red regions, the oxygen mole fraction can be assumed to stay relatively stable when temperature, humidity, or pressure vary. Although not studied, the large and possibly rapid variations in the water concentration are likely to cause problems in the measurements.

The A-band of oxygen near 762nm is well-suited for two-line thermometry near room temperature at atmospheric pressure. The A-band has a selection of well-isolated transitions with weak and strong absorbances, making it good for both short- and long-distance thermometry. The band is also practically free from interfering molecular absorption. The A-band is still accessible using DFB lasers, which enables the design of robust and cost-effective measurement systems.

The simulated spectrum using a 67 m path length of the oxygen R-branch of the A-band is shown in Fig. 12 at 20 $^{\circ}$C temperature and for a standard 20.95 % oxygen concentration. The relative changes in the transmissions for a one kelvin change in temperature calculated using Eq. 28 are also shown in the figure for the strongest transitions. The transitions used in Publications IV and V are marked in Fig. 12 together with the point of the baseline measurement. The laser operating at longer wavelength is used to probe both the transition and the baseline.

The simplified set-up was originally designed for absorption path lengths up to 1000 m. Therefore much weaker transition had to be chosen because of saturation. A transition at 769.23 nm from the P-branch was chosen having a relative change in transmittance of 1.7 %·K^{-1}. The line intensity $S_{\eta\eta'}$ of this transition is only ~3 % as compared to the line intensity of the transitions used in the ratio measurement shown in Fig. 12. The simulated absorption of the transition at 769.23 nm for a 1000 m path length is approximately 43 %, which is fairly close to the optimal.
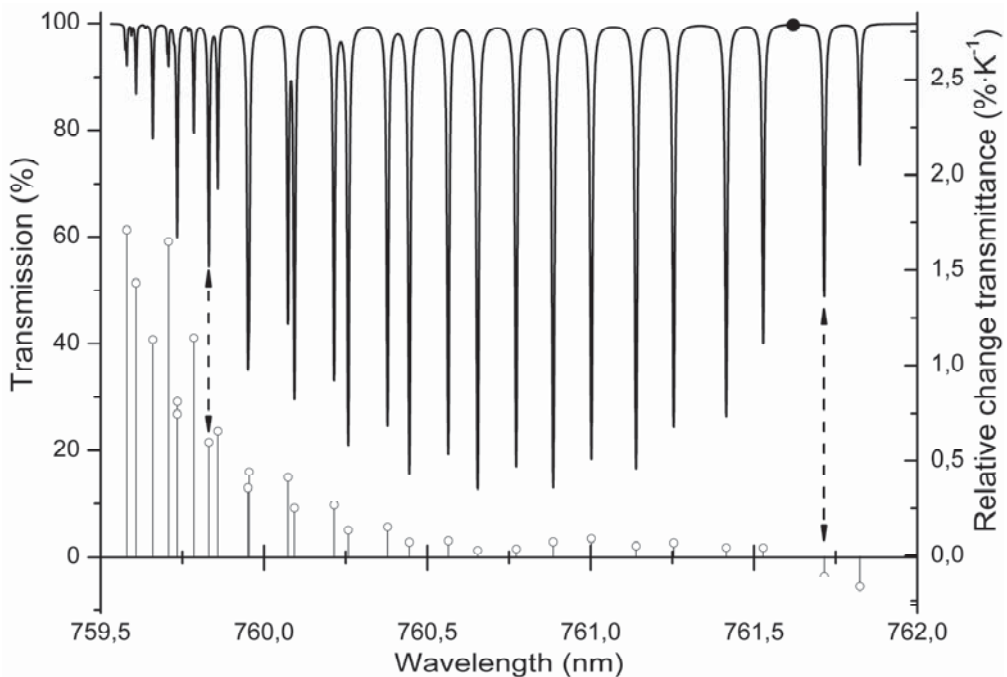
Figure 12. The R-branch of the Oxygen A-band transmission spectrum for a 67 m path in ambient air and relative change in absorption for the strongest transitions. The transitions used in Publication IV and V are marked with dashed double arrows and the black dot marks the position of the baseline. [Publication V].

In the ideal case the wavelength of the water transition would be as close as possible to the oxygen lasers to minimize chromatic errors in optics in our system. Water transitions around 816 nm are virtually free from interfering molecular transitions and several transitions suitable for long distance measurement as well as areas for baseline measurement can be found.

Figure 13 shows simulated transmission spectra of ambient air between 815 nm and 818 nm having 50 % relative humidity at 20 °C over a path length of 67 m. The transition used for the humidity measurement and the position of the baseline measurement are marked with black dots. There are many transitions that are suitable for humidity measurement close to the chosen transition shown in Fig. 13.
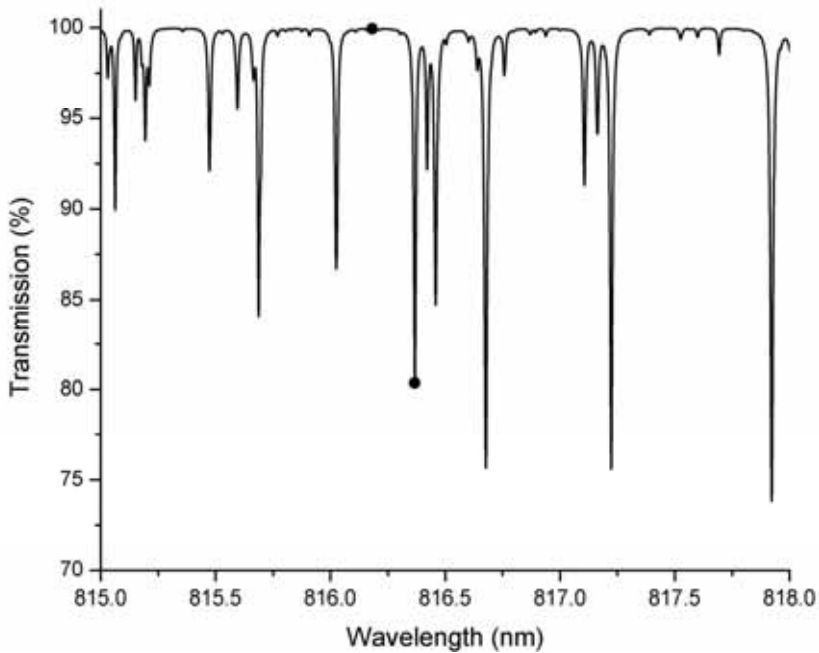
Figure 13. Water transmission spectrum for a 67 m path in ambient air. The transition and the point of the baseline measurement used in Publication VI are marked with black dots.

4.4 Experimental set-ups and measurement routine

The original measurement set-up presented in Publication IV was designed solely for spectroscopic laser thermometry. The refined set-up used in Publications V and VI is essentially similar, except for the added water spectroscopy part making this an integrated solution for determination of the refractive index of air. The refined set-up is shown in Fig. 14. The most significant modifications were the added grating for one oxygen laser and the replacement of achromatic lens with aspheric lens to collimate the output beam. Also an active control to stabilize the beam direction using a position sensitive detector was added. Diffraction grating was added to suppress spurious emissions from the laser that were discovered during the measurements. At the end of the measurement period another grating, which is not shown in Fig. 14, was added to the other oxygen laser for the same reason with good results. The achromatic lens used in the first set-up was not able to collimate both the 760 nm and the 816 nm beams

properly over a long distance. The use of high quality aspheric lens enabled good collimation of both beams simultaneously over long distances without any observable pattern in the beam profile due to aberrations. A single-mode fiber connects the measurement head to the rest of the set-up. An active control of the beam direction, based on piezoelectric transducers and a position sensitive detector is left out of Fig. 14 for clarity.
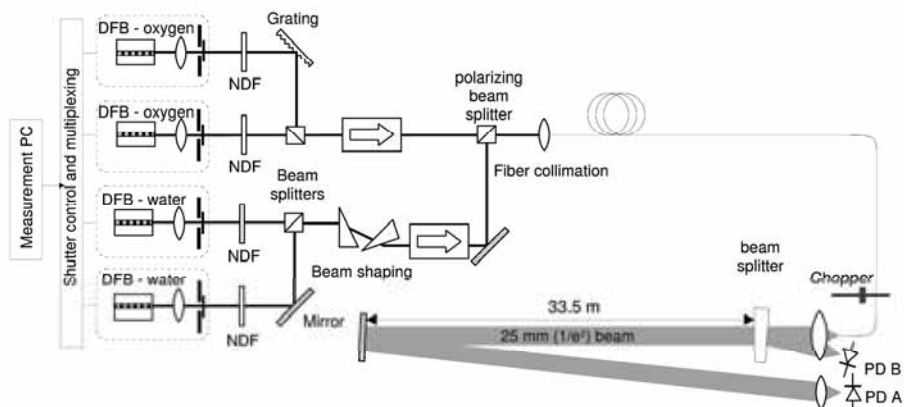
Figure 14. Schematic temperature and humidity measurement setup using a 67 m path length. [Publication V].

The measurement routine is thoroughly explained in Publications IV, V and VI. In short, the measurement is based on measuring the peak absorption and the baseline over a narrow wavelength region near to the line center and close to the point of the baseline measurement, respectively. The peak absorption is determined to be the minimum value of the moving average of the measured data points. The wavelength is loosely stabilized by adjusting the bias current based on the difference of the peak absorption position to the center of the sweep. In the case of baseline measurement, the value of the baseline is simply the arithmetic average of all the measurement points.

In the simultaneous temperature and humidity measurement, the sequence of the peak absorption and the baseline measurements can be varied. The use of one oxygen laser to measure both the peak absorption and the baseline limits the achievable time resolution due to the time needed for wavelength tuning using laser temperature. Typical sample

time for the complete system is over two minutes, whilst the sample time for the humidity measurement that does not require temperature tuning alone is on the order of tens of seconds. In Publication V, we propose a method of decreasing the sample time by locking the wavelengths of the lasers to oxygen absorption peaks using e.g. the third harmonic scheme. The line intensity could be then deduced from the second harmonic signal [20,99,100].

The simplified set-up for thermometry is shown in Fig. 15. The design was done with minimal number of components to ensure good beam quality, which is essential when measuring over long path lengths. A single-mode fiber coupler acts as both spatial filter and provides signal for the reference detector. As only a single line is measured, an electro-optic intensity modulator operating at 20 kHz is used for modulation. The same active control of beam presented in Publication V, was used in the simplified set-up but was left out of Fig. 15 for clarity. The whole set-up shown in Fig. 15 was fit to a portable measurement head.
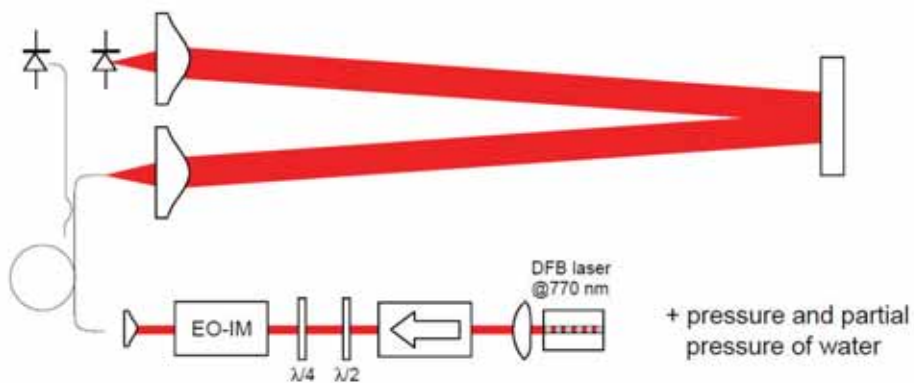
Figure 15. Simplified spectroscopic thermometer using single oxygen transition for thermometry.

The measurement strategy is to measure transmission over the whole absorption. The Voigt profile using database values for the linewidth parameters was fit to the average of several individual sweeps. Each individual sweep had a sample time of 1 s in outdoor measurements and ~0.5 s during the calibration done in MIKES. Individual sweeps are

automatically rejected based on statistical rules, such as large deviations from predicted Voigt profile or overall noise.

4.5   Temperature and humidity measurement results

Most spectroscopic temperature and humidity measurements were done in a temperature and humidity controlled laboratory designed for a 30 m long interferometric measurement rail used for length metrology at MIKES [107]. An average of seven fast semiconductor band-gap temperature sensors were used as the reference in the measurements presented in Publication IV. They were positioned very close to the measurement rail. This caused the thermal mass of the heavy measurement rail to induce dynamic errors during rapid temperature adjustments. In the measurements presented in Publications V and VI, an ensemble of eight calibrated Pt-100 sensors was used as a reference. They were distributed evenly over the 30 m rail and positioned close to the beam path approximately one meter above the rail to achieve good spatial overlap. Temperature of the room was adjusted by varying the temperature of the input air. Only moderate temperature adjustments were possible, because the room was used for dimensional calibrations on regular basis. To calibrate the spectroscopic thermometer, which is required because of the uncertainty in the database parameters [104,105], we conducted a 62 hour measurement including three temperature changes using the refined measurement set-up. The results are shown in Fig. 16. The fit is done using three parameters, namely, ΔE, R_0 and pressure coefficient, which is discussed in Publication V. Period from 48 h to 62 h was used to calculate the noise of the measurement. The RMS noise was 7 mK using sample time of 120 s. The pressure varied between 100 kPa and 101.2 kPa during the measurement.
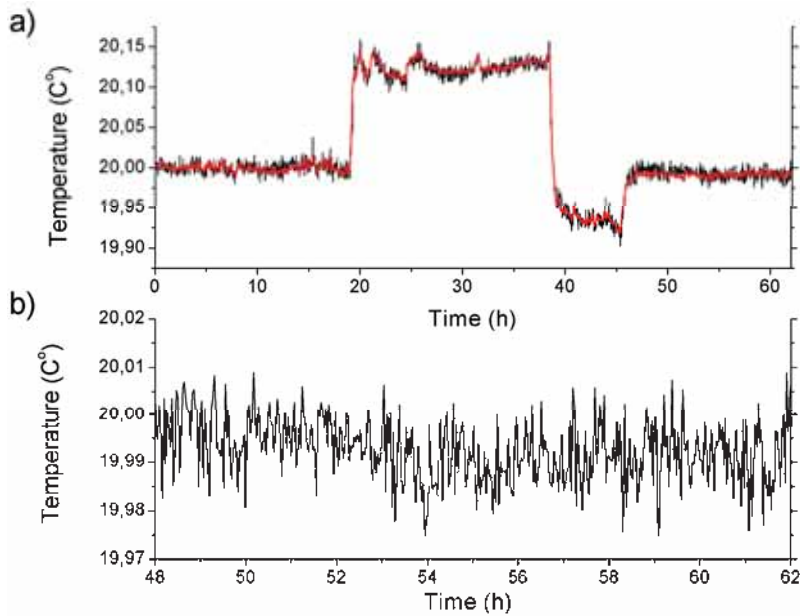
Figure 16. a) Spectroscopic thermometer measurement (black) fitted to the ensemble of Pt-100 sensors (red). b) Spectroscopic temperature from a 12 hour stable period.

The humidity measurement was done in the same laboratory room using the same ensemble of Pt-100 sensors for temperature reference. Four Vaisala HMP45AL were used as the reference humidity sensors, which were calibrated against a primary hygrometer [108], a MBW 373 dew point mirror before the measurement. The expanded uncertainty for the MBW 373 is 0.06 °C, which corresponds to a ~0.17 % in relative humidity at 20 °C and 40 % RH. The humidity measurement set-up was calibrated over a 65 hour period. Humidification of the incoming air was stopped to change the humidity between 20 and 30 hours.

Temperature dependence of the set-up was studied by inducing four temperature steps by adjusting the temperature of the incoming air. Figure 17 shows the result of the fit. The reference humidity and the spectroscopic humidity are marked by black and red lines, respectively. The partial pressure of water vapor can be calculated from the number density using the ideal gas law. The relative humidity was calculated using the partial pressure and temperature by using an empiric equation for the saturation vapor

pressure of water [109]. Reference sensors were mounted close to the ceiling approximately 1 meter above the beam path. This may have caused an error since the air flow in the laboratory is downward. Therefore, local humidity sources such as humans are not seen by the reference sensors. The maximum difference between the spectroscopic measurement and the reference occur at the point of the minimum humidity and right before the temperature variations. This is likely due to faster response time of the spectroscopic sensor. In both cases, the difference is approximately 0.4 %. The average deviation (RMS) from the reference sensors for a 21 hour period just before the ambient humidity change at 23 hour mark was ~0.04 % RH. The sample time of the humidity sensor was 38 s.
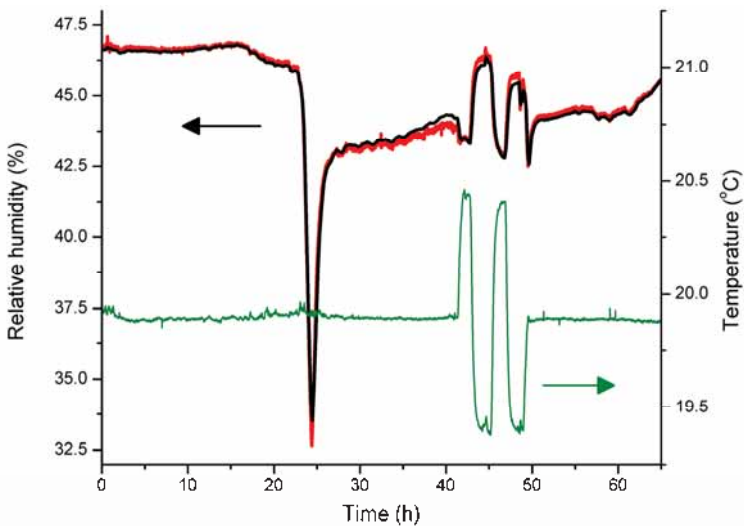
Figure 17. Spectroscopic humidity measurement (red) fitted to the ensemble of reference sensors (black). The ambient temperature is shown in green.

An outdoor test of the refined set-up was performed at Nummela geodetic standard baseline in October 2010. The measurement head was located outside under a roof for protection against rain. The measurement system was kept in a heated room with no temperature control. The end mirror was mounted on a pillar 65 m from the measurement head making the total measurement distance 130 m. An ensemble of ten

Pt-100 sensors was used as a temperature reference. Both humidity and temperature were measured simultaneously using a sample time of 135 s.

The results are shown in Fig. 18. Spectroscopic temperature and reference temperature are marked with red and black lines, respectively. Spectroscopic humidity is marked with blue line and the blue circles represent the reference humidity values. Parameters obtained from the laboratory measurements were used for both humidity and temperature measurements.

The sun was still shining at the beginning of the measurement period, which has likely affected the values during the first hour. Otherwise, the approximately 200 mK offset remains stable for the rest of the measurement period. The offset is most likely caused by the transportation of the setup, which was observed after the outdoor measurements. One major factor causing the offset could be non-ideal collimation of the laser beams, which we could not verify in the outdoor conditions. The 200 mK offset corresponds to ~1.7 x 10^{-3} difference in the line intensity ratio R. Due to these reasons, the temperature of the ten Pt-100 sensors were used to calculate the spectroscopic relative humidity shown in Fig. 18.

The spectroscopic relative humidity is on average ~1.5 % higher as compared to the reference value measured from a single point using Vaisala PTU200. The results are in good agreement, because the accuracy of the reference sensor is ±3 % at high relative humidity range.
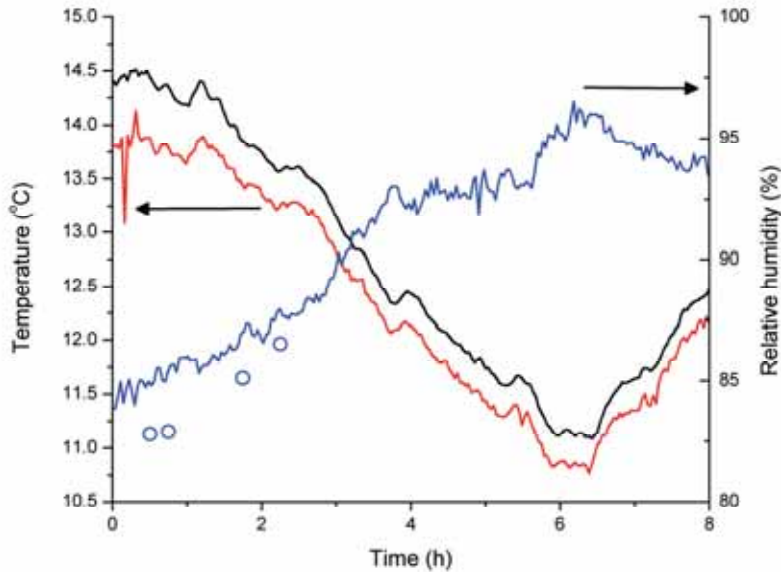
Figure 18. Spectroscopic humidity (blue) and temperature (red) measurement performed at Nummela baseline. The reference temperature measurement is shown in black. Blue circles represent the reference humidity measurement.

The simplified set-up was calibrated in laboratory conditions before it was tested at the BEV geodetic baseline in Innsbruck. The RMS noise using 12 s sample time was 140 mK. The total measurement distance was 240 m using a double-pass scheme. Unfortunately we had to use a different transition at 769.13 nm for the outdoor thermometry, because of stability problems with temperature controller in outdoor environment. The reference temperature was measured with Vaisala DMP248 probe close to the measurement head. We used digital low-pass filtering for the raw data to simulate the long response time of the reference sensor.

The sample time in the outdoor measurements was ~20 s. Each sample consisted of an average of eight individual sweeps. The sample time was considerably higher than the time required to measure eight individual sweeps due to delay in the data transfer. A sample is shown in Fig. 19 including a Voigt fit and a residual plot.
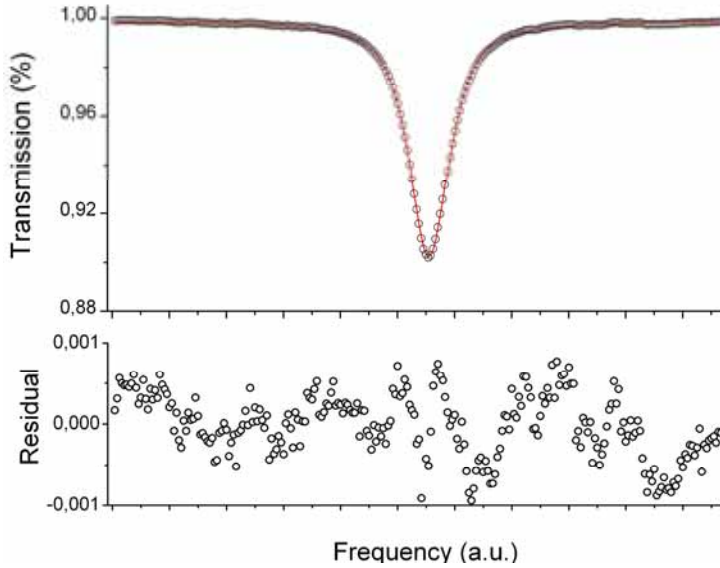
Figure 19. A typical transmission measurement using the simplified spectroscopic thermometer. The 256-point measurement data is marked with black circles and the Voigt fit using a red line. The measurement was done at the BEV geodetic baseline in Innsbruck using a path length of 240 m.

The temperature measurement results are shown in Fig. 20. The fit is done using $S_{\eta\eta}(T_{ref})$ and ΔE as the free parameters, because we could not use the calibration data. The baseline is situated between a river and a busy highway very close to a base of a mountain. These factors combined with a changing weather likely induce rapid variations in the temperature. The slightly increased noise around 40 minutes is explained by light rain during that period. The measurement distance was limited by size of the beam input aperture at long distances due to beam divergence.
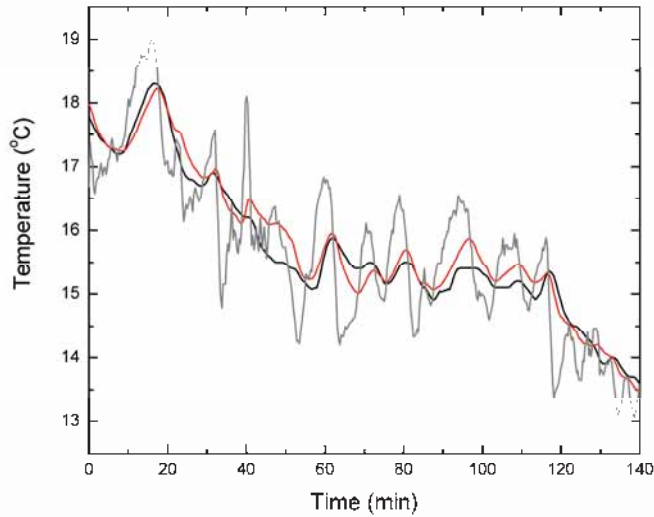
Figure 20. Spectroscopic temperature measurement performed at the Innsbruck baseline. The spectroscopic temperature using 20 s sample time is shown in grey. The low-pass filtered spectroscopic temperature and reference sensor data are marked with red and black lines, respectively.

4.6 Effective compensation of the refractive index of air in an interferometric length measurement

The spectroscopic temperature measurement set-up was combined with a commercial interferometer to test compensation of a real interferometer and to compare the results obtained with conventional sensors. The system was configured to measure only temperature, which is by far the most crucial component in determining the refractive index of air when using Edlen or Ciddor equations [11,12,13]. For example, to reach an uncertainty of 10^{-7}, the ambient average temperature over the measurement path has to be known with an accuracy of 110 mK. On the other hand humidity measurement is especially important when using sophisticated two-colour interferometry, which cancels out the contribution of temperature, pressure and CO_2 concentration on the refractive index if humidity is accurately known [17].

To simulate harsh industrial or outdoor environment, a combination of a heater and a fan were used to induce local temperature variations. The reference value for the refractive index was calculated using the temperature measured by the same ensemble

of eight Pt-100 sensors that were used in the calibrations and using the calibrated spectroscopic sensor. Part b in Fig. 21 shows the average temperature measured by spectroscopic method (red) and by the ensemble of Pt-100 sensors (black). The compensated interferometric reading is shown in part a of Fig. 21. It is evident that the spectroscopic method is able to effectively compensate the refractive index of air even when local temperature gradients are present. This also shows that even fairly closely positioned Pt-100 sensors are not able to compensate local variations. The transients during the temperature changes can be partly explained by the 120 s sample time. The long term drift in the displacement is likely caused by real mechanical displacements of the interferometer. The temperature determined by the spectroscopic system was approximately 10 mK lower than the reference temperature between the heating periods. This could be caused by the realignment of the optics during the assembly of the interferometric system.
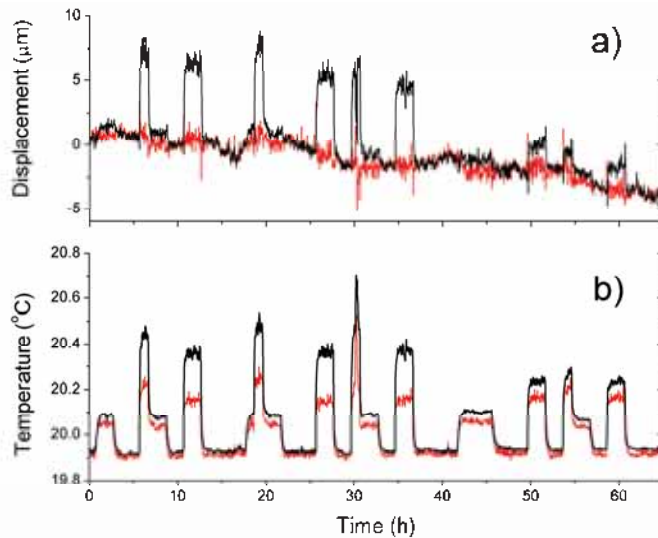
Figure 21. Part a shows the results of interferometric length compensated by using Pt-100 sensors (black) or by using spectroscopic temperature measurement (red). Part b shows the average temperatures along the path length with local temperature variations measured by Pt-100 sensors (black) and by spectroscopic system (red).

The accuracy of the temperature measurement system is difficult to evaluate. Re-evaluation of the data presented in Publication IV showed a 20 mK offset when changes

were made to the system during a measurement. Considering the 10 mK offset that was observed in our refined temperature measurement system during the interferometric tests, we believe that, with the refined system and calibration, we are able to determine the air temperature with an accuracy high enough to safely reach an uncertainty smaller than 10^{-7} in the refractive index of air. Based on the maximum differences of ~0.4 % RH in the long term measurement and the ~0.04 % RH RMS noise, the humidity measurement part of the system safely enables the determination of the refractive index of air with an uncertainty smaller than 10^{-7} even when using the two-colour interferometry as discussed in Publication VI.

The performance of the integrated set-up is tested both in laboratory environment and in outdoor environment over distances up to 130 m. The compensation of the refractive index of air in interferometric measurement was found excellent compared to a reference method using conventional sensors. The second set-up constituting a simpler sensor, developed for long distance measurements, is useful in long distance geodetic applications, where simple and robust sensors are needed.

5 Conclusions

In this work, measurement of fiber nonlinearity, external-cavity diode lasers and spectroscopic temperature and humidity measurements were studied and developed.

The widely used and reliable continuous-wave self-phase modulation technique to measure the nonlinear coefficient of single-mode fibers was improved by including the effects of dispersion. The performance of the developed simulation tool based on numerical analysis of the Nonlinear Schrödinger equation was found to be effective in single-mode fiber measurements. The flexible simulation method is readily implemented to existing measurement set-ups and it is not dependent on fiber length or other measurement parameters. To further increase the accuracy of the CW-SPM method, an integrated sphere with low measurement uncertainty was characterized and applied to the crucial fiber optic power measurement. The developed measurement set-up is capable of measuring the nonlinear coefficient of a standard single-mode fiber with an expanded uncertainty of 2.0 %.

Further analysis of the measurement conditions was needed in measurement of amplifying erbium-doped single-mode fibers. The same CW-SPM method was used to measure a fiber of only some meters long. The difficulties of measuring erbium-doped fibers as an amplifying fiber were discussed. The complex nature of signal amplification and spectral hole burning would induce significant uncertainty to the total measurement uncertainty if not taken into account. A more straightforward approach to measure the erbium-doped fiber in passive mode was adopted resulting in good results. By carefully analyzing all the components in the measurement set-up, the nonlinear coefficient of the erbium-doped single-mode fiber was determined with an expanded uncertainty of 3.0 %.

The high accuracy measurements of both standard single-mode fibers and erbium-doped fibers using standard laboratory equipment will greatly improve the possibilities to determine fiber nonlinearity in laboratories worldwide.

An external-cavity diode laser based on volume holographic grating was developed and characterized. It is shown that it is possible to design simple ECDLs using the grating at

normal incidence. In the presented design, the beam directional variations are virtually nonexistent as compared to the conventional Littrow ECDL designs when the angle feedback element is changed. The applicability of the inherently non-dispersive grating as a wavelength selective feedback with common diode laser is demonstrated for the first time. The narrow bandwidth of the grating ensures that the wavelength is more reproducible as compared with designs using diffraction gratings. A mode-hop free tuning range of 28 GHz and a practical 1-s linewidth of 900 kHz were achieved, which are sufficient in most application in e.g. molecular spectroscopy and metrology. A previously presented short cavity ECDL based on VHG at close proximity of the laser diode was characterized. The broad mode-hop free tuning range and robust design make it suitable for industrial broadband molecular spectroscopy.

The final part of the work done at MIKES was aimed to effectively compensate the refractive index of air, which is crucial in dimensional metrology. A complete system using diode laser spectroscopy to measure average humidity and temperature over a long path was developed and tested both in laboratory and outdoor environment. The beam of the spectroscopic system can be aligned very close to the beam used by the dimensional measurement devices enabling very good spatial overlap.

A total of five diode lasers are used in the system. Three are used to measure the temperature, which is deduced from the ratio of the peak absorptions of two oxygen transitions. Two lasers are use to measure the peak absorption and the baseline to determine the absolute humidity. In a stable laboratory environment, the noise of the spectroscopic temperature measurement over a 67 m path was 7 mK using a sample time of 120 s. The humidity part of the system was tested against calibrated humidity sensors is a laboratory with changes in humidity and temperature. Both the humidity and temperature can be measured within an uncertainty that is sufficient to compensate changes of the refractive index of air well below the 10^{-7} level. The measurement system was demonstrated in outdoor environment over a 130 m path with good results. A method is proposed for decreasing the sample time in the next stage by locking the wavelengths of the lasers to oxygen absorption peaks using e.g. the third harmonic scheme. The refined set-up could find applications e.g. in the dimensional

characterisation of nuclear waste repositories or in the dimensional surveillance and characterisation of large work pieces in the production process.

A robust and portable spectroscopic temperature system was developed for long range measurements. The system using only one laser measuring the temperature from a single oxygen transition was tested both in indoor and outdoor environment. The simple system was successfully demonstrated over a path length of 240 m in harsh outdoor environment. The simplicity in the data analysis and the robustness make it a potential choice for long distance measurements e.g. in geodetic applications.

The final demonstration of the performance of the integrated system was done in a laboratory to compensate the refractive index of air in a long term interferometric distance measurement. Local temperature variations were induced to simulate harsh industrial conditions. The compensation done by the spectroscopic system was close to perfect, when the properly set ensemble of conventional reference sensors failed. The system can be added to already existing measurement systems and it will greatly improve the accuracy especially in industrial dimensional measurements.

References

[1] H. Ishio, J. Minowa and K. Nosu, "Review and status of wavelength-division-multiplexing technology and its application," IEEE J. Lightwave Tech. **2**, 448-463 (1984).

[2] R. J. Mears, L. Reekie, M. Jauncey and D. N. Payne, "Low-noise erbium-doped fiber amplifier operating at 1.54 μm", Electron. Lett. **26**, 1026-1028 (1987).

[3] E. Desurvire, J. R. Simpson and P. C. Becker, "High-gain erbium-doped traveling-wave fiber amplifier," Opt. Lett. **12**, 888-890 (1987).

[4] D. Marcuse, A.R. Chraplyvy and R.W. Tkach, "Effect of fiber nonlinearity on long-distance transmission," IEEE J. Lightwave Tech. **9**, 121-128 (1991).

[5] G. P. Agrawal, "Nonlinear Fiber Optics," 3rd ed., Academic Press 2001, ISBN 9780120451432.

[6] A. Boskovic, S. V. Chernikov, J. R. Taylor, L. Gruner-Nielsen and O. A. Levring, "Direct continuous-wave measurement of $n2$ in various types of telecommunication fiber at 1.55 μm," Opt. Lett. **21**, 1966-1968 (1996).

[7] T.H. Maiman, "Stimulated optical radiation in ruby masers," Nature **187**, 493-494 (1960).

[8] M. Fleming and A. Mooradian, "Spectral characteristics of external-cavity controlled semiconductor lasers", IEEE J. Quantum Electron. **17**, 44-59 (1981).

[9] C. E. Wieman and L. Hollberg, "Using diode lasers for atomic physics," Rev. Sci. Instrum. **62**, 1-20 (1991).

[10] R. Wyatt and W.J. Devlin, "10 kHz linewidth 1.5 μm InGaAsP external cavity laser with 55 nm tuning range," Electron. Lett. **19**, 110-112 (1983).

[11] G. Bonsch and E. Potulski, "Measurement of the refractive index of air and comparison with modified Edlén's formulae," Metrologia **35**, 133-139 (1998).

[12] B. Edlen, "The Refractive Index of Air," Metrologia **2**, 71-80 (1966).

[13] P.E. Ciddor, "Refractive index of air: new equations for the visible and near infrared," Appl. Opt. **35**, 1566-1573 (1996).

[14] Personal communication with Antti Lassila.

[15] K.B. Earnshaw and E.N. Hernandez, "Two-Laser Optical Distance-Measuring Instrument that Corrects for the Atmospheric Index of Refraction," Appl. Opt. **11**, 749-754 (1972).

[16] H. Matsumoto and T. Honda, "High-accuracy length-measuring interferometer using the two-colour method of compensating for the refractive index of air," Meas. Sci. Technol. **3** 1084-1086 (1992).

[17] K. Meiners-Hagen and A. Abou-Zeid, "Refractive index determination in length measurement by two-colour interferometry," Meas. Sci. Technol. **19**, 084004(5pp) (2008).

[18] V. Korpelainen and A Lassila, "Acoustic method for determination of the effective temperature and refractive index of air in accurate length interferometry," J. Opt. Eng. **43**, 2400-2409 (2004).

[19] M.P. Arroyo and R.K. Hanson, "Absorption measurements of water vapor concentration, temperature and line-shape parameters using a tunable InGaAsP diode laser," Appl. Opt. **32**, 6104-6116 (1993).

[20] J. Silver, D. J Kane, "Diode laser measurements of concentration and temperature in microgravity combustion," Meas. Sci. Technol. **10**, 845–852 (1999).

[21] V. Ebert, T. Fernholz, C. Giesemann, H. Pitz, H. Teichert, J. Wolfrum, and H. Jaritz, "Simultaneous diode-laser-based in-situ detection of multiple species and temperature in a gas-fired power-plant," Proc. Combust. Inst. **28**, 423–430 (2000).

[22] R.H. Stolen and C. Lin, "Self-phase-modulation in silica optical fibers," Phys. Rev. A **17**, 1448–1453 (1978).

[23] F. Forghieri, R.W. Tkach, A.R. Chraplyvy and D. Marcuse, "Reduction of four-wave mixing crosstalk in WDM systems using unequally spaced channels," IEEE Photon. Technol. Lett., **6**, 754–756 (1994).

[24] M.N. Islam, L.F. Mollenauer, R.H. Stolen, J.R. Simson and H.T. Shang, "Cross-phase modulation in optical fibers," Opt. Lett. **12**, 625-627 (1987).

[25] R.G. Smith, "Optical power handling capacity of low loss optical fibers as determined by stimulated Raman and Brillouin scattering," Appl. Opt. **11**, 2489–2494 (1972).

[26] R. Billington, "Effective area of optical fibres—definition and measurement techniques," Tech. Rep. (National Physical Laboratory, Teddington, Middlesex, UK, 2003).

[27] K. Petermann, "Constraints for fundamental-mode spot size for broadband dispersion-compensated single-mode fibers," Electron. Lett. **19**, 712–714 (1983).

[28] C. Pask, "Physical interpretation of Petermann's strange spot size for single-mode fibres," Electron. Lett. **20**, 144–145 (1984).

[29] Y. Namihira, "Relationship between nonlinear effective area and mode field diameter for dispersion shifted fibers," Electron. Lett. **30**, 262-263 (1994).

[30] Y. Namihira, "Wavelength dependence of the correction factor on effective area and mode field diameter for various single-mode optical fibers," Electron. Lett. **33**, 1483-1485 (1997).

[31] M. Young, "Mode-field diameter of single-mode optical fiber by far-field scanning", Appl. Opt. **37**, 5605-5619 (1998).

[32] M. Artiglia, G. Coppa, P. Di Vita, M. Potenza and A. Sharma, "Mode-field diameter measurements in single mode optical fibers," IEEE J. Lightwave Tech. **7**, 1139-1152 (1989).

[33] International Telecommunication Union, "Definitions and test methods for statistical and non-linear related attributes of single-mode fibre and cable," ITU-T Recommendation G.650.2 (07/2007).

[34] F.M. Mitschke and L.F. Mollenauer, "Discovery of the soliton self-frequency shift," Opt. Lett. **11**, 659–661 (1986)

[35] D. Anderson and M. Lisak, "Nonlinear asymmetric self-phase modulation and self-steepening of pulses in long optical wave- guides," Phys. Rev. A **27**, 1393–1398 (1983).

[36] E. Bourkoff, W. Zhao, R.I. Joseph and D.N. Christodoulides, "Evolution of femtosecond pulses in single-mode fibers having higher-order nonlinearity and dispersion," Opt. Lett., vol. **12**, 272-274 (1987).

[37] M.N. Islam, "Raman amplifiers for telecommunications," IEEE Select. Topics. Quant. Electron. **8**, 548-559 (2002).

[38] P. Urquhart, "Review of rare-earth doped fiber lasers and amplifiers," IEE Proc. **135,** 385-407 (1988).

[39] E. Desurvire, "Erbium-doped fiber amplifiers - principles and applications", John Wiley 1994, ISBN 9780471264347.

[40] Y. Sun, J.L. Zyskind and A.K. Srivastava, "Average inversion level, modeling, and physics of erbium-doped fiber amplifiers," IEEE J. Select. Topics Quantum Electron., **3**, 991-1007 (1997).

[41] A.A.M. Saleh, R.M. Jopson, J.D. Evankow and J. Aspell, "Modeling of gain in erbium-doped fiber amplifiers," IEEE Photon. Technol. Lett., **2**, 714-717 (1990).

[42] Y. Namihira, "ITU-T round robin measurement for nonlinear coefficient (n2/Aeff) of various single mode optical fibers," in Tech. Dig. Symp. Opt. Fiber Meas., 33-36 (2004).

[43] K. Nakajima, T. Omae and M. Ohashi "Conditions for measuring nonlinear refractive index n2 of various single-mode fibre using CW-SPM method", IEE Proc. Optoelectron. **148**, 209-214 (2001).

[44] J.-C. Antona, S. Bigo and S. Kosmalski, "Nonlinear index measurements of various fiber types over C+L bands using four-wave mixing," Proc. ECOC 2001, 27th Eur. Conf. on Optical Comm. (Amsterdam, The Netherlands, Sept. 30-Oct. 4, 2001), 270-271.

[45] L. Prigent and J.P. Hamaide, "Measurement of fiber nonlinear Kerr coefficient by four-wave mixing," IEEE Photon. Technol. Lett. **5**, 1092-1095 (1993).

[46] S.V. Chernikov and J.R. Taylor, "Measurement of normalisation factor of n_2 for random polarization in optical fibers," Opt. Lett. **21**, 1559-1561 (1996).

[47] R.H. Stolen and C. Lin, "Self-phase-modulation in silica optical fibers," Phys. Rev. A **17**, 1448-1453 (1978).

[48] Y. Namihira, A. Miyata and N. Tanahashi, "Nonlinear coefficient measurements for dispersion shifted fibres using self-phase modulation method at 1.55 µm," Electron. Lett. **30**, 262-264 (1994).

[49] K.S. Kim, R.H. Stolen, W.A. Reed and K.W. Quoi, "Measurement of the nonlinear index of silica-core and dispersion-shifted fibers", Opt. Lett., **19**, 1006-1012 (1994).

[50] T. Kato, Y. Suetsugu, M. Takagi, E. Sasaoka and M. Nishimura, "Measurement of the nonlinear refractive index in optical fiber by the cross-phase-modulation method with depolarized pump light," Opt. Lett. **20**, 988-990 (1995).

[51] M. Artiglia, E. Ciaramell, and B. Sordo, "Using modulation instability to determine Kerr coefficient in optical fibers," Electron. Lett. **31**, 1012-1013 (1995).

[52] C. Vinegoni, M. Wegmuller and N. Gisin, "Determination of nonlinear coefficient

(n2/Aeff) using self-aligned interferometer and Faraday mirror," Electron. Lett. **26**, 886-888 (2000).

[53] M. Artiglia, R. Caponi, F. Cisterninno, C. Naddeo and D. Roccato, "A new method for the measurement of the nonlinear refractive index of optical fiber," Opt. Fiber Technol. **2**, 75-79 (1996).

[54] H. Garcia, A.M. Johnson, F.A. Oguama and S. Trivedi, "New approach to the measurement of the nonlinear refractive index of short (<25 m) lengths of silica and erbium-doped fibers," Opt. Lett. **28**, 1796-1798 (2003).

[55] S.V. Chernikov and J.R. Taylor, "Measurement of normalization factor of n2 for random polarization in optical fibers", Opt. Lett. **21**, 1559-1561 (1996).

[56] E.L. Buckland and J.W. Boyd, "Electrostrictive contribution to the intensity-dependent refractive index of optical fibers", Opt. Lett. **21**, 1117-1119 (1996).

[57] A. Melloni, M. Frasca, A. Garavaglia, A. Tonini and M. Martinelli, "Direct measurement of electrostriction in optical fibers," Opt. Lett. **23**, 691-693 (1998).

[58] A. Lamminpää, T. Niemi, E. Ikonen, P. Marttila and H. Ludvigsen, "Effects of dispersion on nonlinearity measurement of optical fibers," Opt. Fiber Technol. **11**, 278-285 (2005).

[59] J. Envall, P. Kärhä and E. Ikonen, "Measurement of fibre optic power using photodiodes with and without integrating sphere," Metrologia **41**, 353-358 (2004).

[60] A. Carrasco-Sanz, F. Rodriguez-Barrios, P. Corredera, S. Martin-Lopez, M. Gonzalez-Herraez and M.L. Hernanz "An integrating sphere radiometer as a solution for high power calibrations in fiber optics," Metrologia **43** 145-150 (2006).

[61] E.F. Zalewski and J. Geist, "Solar cell spectral response characterization," Appl. Opt. **18**, 3942-3947 (1979).

[62] M. Bolstyansky, "Spectral hole burning in erbium-doped fiber amplifiers," IEEE J. Lightwave Tech. **21**, 1032-1038 (2003).

[63] H. Garcia, A.M. Johnson, F.A. Oguama and S. Trivedi, "Pump-induced nonlinear refractive index change in erbium- and ytterbium-doped fibers: Theory and experiment," Opt. Lett. **30**, 1261-1263 (2005).

[64] J.F. Massicott, R. Wyatt and B.J. Ainslie, "Low noise operation of Er3+ doped silica fiber amplifier around 1.6 μm," Electron. Lett. **28**, 1924-1925 (1992).

[65] Y. Sun, J.W. Sulhoff, A.K. Srivasta, J.L. Zyskind, T.A. Strasser, J.R. Pedrazzani, C. Wolf, J. Zhou, J.B. Judkins, R.P. Espindola and A.M. Vengsarkar, "80 nm ultra-wideband erbium-doped silica fiber amplifier," Electron. Lett. **33**, 1965-1967 (1997).

[66] P. Bhattacharya, "Semiconductor Optoelectronic Devices," 1st ed. Prentice-Hall 1994, ISBN 0138057486.

[67] W.W. Chow and S.W. Koch, "Semiconductor Laser Fundamentals," 1st ed. Springer-Verlag 1999, ISBN 9783540641667.

[68] L. Mercer, "1/f Frequency noise effects on self-heterodyne linewidth measurements," J. Lightw. Technol. **9,** 485-493 (1991).

[69] C.H. Henry, "Theory of the linewidth of semiconductor lasers," IEEE J. Quantum Electron. **18**, 259-264 (1982).

[70] M. Osinski and J. Buus, "Linewidth broadening factor in semiconductor lasers — An overview," IEEE J. Quantum Electron. **23**, 9-28 (1987).

[71] L. Hsu, A. Mooradian and R.L. Aggarwal, "Spectral linewidth of a free-running continuous-wave single-frequency external-cavity quantum-well InGaAs/AlGaAs diode laser," Opt. Lett. **20**, 1788-1790 (1995).

[72] R.W. Tkach and A.R. Chraplyvy, "Regimes of feedback effects in 1.5-µm distributed feedback lasers," IEEE J. Lightwave Tech. **4**, 1655-1661 (1986).

[73] K.C. Harvey and C.J. Myatt, "External-cavity diode laser using a grazing-incidence diffraction grating," Opt. Lett. **16**, 910-912 (1991).

[74] A.S. Arnold, J.S. Wilson and M.G. Boshier, "A simple extended-cavity diode laser," Rev. Sci. Instrum. **69,** 1236-1239 (1998).

[75] H. Talvitie, A. Pietiläinen, H. Ludvigsen and E. Ikonen, "Passive frequency and intensity stabilization of extended-cavity lasers," Rev. Sci. Instrum. **68**, 1-7 (1997).

[76] R. Lang and K. Kobayashi, "External optical feedback effects on semiconductor injection laser properties," IEEE J. Quantum Electron. **16**, 347-355 (1980).

[77] M. Kourogi, K. Imai, B. Widyatmoko, T. Shimizu and M. Ohtsu, "Continuous tuning of an electrically tunable external-cavity semiconductor laser," Opt. Lett. **25**, 1165-1167 (2000).

[78] J. Struckmeier, A. Euteneuer, B. Smarsly, M. Breede, M. Born, M. Hofmann, L. Hildebrand and J. Sacher, "Electronically tunable external-cavity laser diode," Opt. Lett. **24**, 1573-1574 (1999).

[79] M.G. Littman and H.J. Metcalf, "Spectrally narrow pulsed dye laser without beam expander," Appl. Opt. **17**, 2224-2227 (1978).

[80] M. Merimaa, H. Talvitie, P. Laakkonen, M. Kuittinen, I. Tittonen and E. Ikonen, "Compact external-cavity diode laser with a novel transmission geometry," Opt. Commun. **174**, 175-180 (2000).

[81] Y. Suematsu , S. Arai and K. Kishino "Dynamic single-mode semiconductor lasers with a distributed reflector," J. Lightw. Technol. **1**, 161-176 (1983).

[82] M. Bagley, R. Wyatt, D.J. Elton, H.J. Wickes, P.C. Spurdens, C.P. Seltzer, D.M. Cooper

and W.J. Devlin, "242 nm continuous tuning from a grin-SC-MQW-BH InGaAsP laser in an extended cavity," Electron. Lett. **26**, 267-269 (1990).

[83] P. Mills, R. Plastow, "Single mode operation of 1.55 μm semi-conductor laser using a volume holographic grating," Electron. Lett. **21**, 648-649 (1985).

[84] G.J. Steckman, W. Liu, R. Platz, D. Schroeder, C. Moser and F. Havermeyer, "Volume holographic grating wavelength stabilized laser diodes," IEEE J. Sel. Top. Quantum Electron. **13**, 672-678 (2007).

[85] F. Kroeger, I. Breunig, K. Buse, "Frequency stabilization and output power undulations of diode lasers with feedback by volume holographic gratings," Appl. Phys. B **95**, 603-608 (2009).

[86] G. Blume, C. Fiebig, D. Feise, C. Kaspari, A. Sahm, K. Paschke and G. Erbert, "Room temperature 633 nm tapered diode lasers with external wavelength stabilisation," IET Optoelectron. **3**, 320-325 (2009).

[87] J.W. Goodman, "Introduction to Fourier Optics," 3rd ed. Roberts & company, 2005, ISBN 9780974707723.

[88] C. Moser, L. Ho and F. Havermeyer, "Self-aligned non-dispersive external cavity tunable laser," Opt. Exp. **16**, 16691-16696 (2008).

[89] J.E. Hellstrom, B. Jacobsson, V. Pasiskevicius and F. Laurell, "Finite Beams in Reflective Volume Bragg Gratings: Theory and Experiments," IEEE J. Quantum Electron. **44**, 81-89 (2008).

[90] L.S. Rothman, C.P. Rinsland, A. Goldman, S.T. Massie, D.P. Edwards, J.-M. Flaud, A. Perrin, C. Camy-Peyret, V. Dana, J.-Y. Mandin, J. Schroeder, A. McCann, R.R. Gamache, R.B. Wattson, K. Yoshino, K.V. Chance, K.W. Jucks, L.R. Brown, V. Nemtchinov and P. Varanasi, "The HITRAN Molecular Spectroscopic Database and HAWKS (HITRAN Atmospheric Workstation): 1996 Edition," J. Quant. Spectrosc. Radiat. Transfer **60**, 665-710 (1998).

[91] J. Shao, L. Lathdavong, P. Kluczynski, S. Lundqvist and O. Axner, "Methodology for temperature measurements in water vapor using wavelength-modulation tunable diode laser absorption spectrometry in the telecom C-band," Appl. Phys. B **97**, 727-748 (2009).

[92] L.S. Rothman, I. Gordon, A. Barbe, D. Benner, P. Bernath, M. Birk, V. Boudon, L. Brown, A. Campargue, J.-P. Champion, K. Chance, L. Coudert, V. Dana, V. Devi, S. Fally, J.-M. Flaud, R. Gamache, A. Goldman, D. Jacquemart, I. Kleiner, N. Lacome, W. Lafferty, J.-Y. Mandin, S. Massie, S. Mikhailenko, C. Miller, N. Moazzen-Ahmadi, O. Naumenko, A. Nikitin, J. Orphal, V. Perevalov, A. Perrin, A. Predoi-Cross, C. Rinsland, M. Rotger, M. Simecková, M. Smith, K. Sung, S. Tashkun, J. Tennyson, R. Toth, A. Vandaele and J. Vander Auwera, "The HITRAN 2008 molecular spectroscopic database," J. Quant. Spectrosc. Radiat. Transf. **110**, 533-572 (2009).

[93] W. Demtröder, "Laser Spectroscopy," 2nd ed., Springer 1998, ISBN 9783540571711

[94] Y. Liu, J. Lin, G. Huang, Y. Guo and C. Duan, "Simple empirical analytical approximation to the Voigt profile," J. Opt. Soc. Am. B **18**, 666-672 (2001).

[95] L. Galatry, "Simultaneous effect of Doppler and foreign gas broadening on spectral lines," Phys. Rev. **122**, 1218-1223 (1961).

[96] P. L. Varghese and R. K. Hanson, "Collisional narrowing effects on spectral line shapes measured at high resolution," Appl. Opt. **23**, 2376-2385 (1984).

[97] J.M. Hollas, "Modern Spectroscopy," 4th ed., Wiley 2004, ISBN 9780470844168

[98] A.Y. Chang, E.C. Rea, Jr. and R.K. Hanson, "Temperature measurements in shock tubes using a laser-based absorption technique," Appl. Opt. **26**, 885-891 (1987).

[99] J.T.C. Liu, J.B. Jeffries and R.K. Hanson, "Large-Modulation-Depth 2f Spectroscopy with Diode Lasers for Rapid Temperature and Species Measurements in Gases with Blended and

Broadened Spectra," Appl. Opt. **43**, 6500-6509 (2004).

[100] J. Shao, L. Lathdavong, P. Kluczynski, S. Lundqvist and O. Axner, "Methodology for temperature measurements in water vapor using wavelength-modulation tunable diode laser absorption spectrometry in the telecom C-band," Appl. Phys. B **97**, 727-748 (2009).

[101] Further information on HITRAN available from www.hitran.com

[102] M. Vainio, M. Siltanen, T. Hieta and L. Halonen, "Continuous-wave optical parametric oscillator based on a Bragg grating," Opt. Lett. **35**, 1527-1529 (2010).

[103] X. Zhou, X. Liu, J.B. Jeffries and R.K. Hanson, "Development of a sensor for temperature and water vapor concentration in combustion gases using a single tunable diode laser," Meas. Sci. Technol. **14**, 1459-1468 (2003).

[104] X. Zhou, J.B. Jeffries and R.K. Hanson, "Development of a fast temperature sensor for combustion gases using a single tunable diode laser," Appl. Phys. B **81**, 711-722 (2005).

[105] S.T. Sanders, J. Wang, J.B. Jeffries and R.K. Hanson, "Diode-Laser Absorption Sensor for Line-of-Sight Gas Temperature Distributions," Appl. Opt. **40**, 4404-4415 (2001).

[106] R. Benedetti, K. Giulietti and M. Rosa-Clot, "Line shape analysis of O2 in air as a way to measure temperature using a DFB-diode-laser at 761 nm," Opt. Commun. **154**, 47-53 (1998).

[107] A. Lassila, M. Kari, H. Koivula, U. Koivula, J. Kortstrom, E. Leinonen, J. Manninen, J. Manssila, T. Mansten, T. Merilainen, J. Muttilainen, J. Nissila, R. Nyblom, K. Riski, J. Sarilo and H. Isotalo, "Design and performance of an advanced metrology building for MIKES," Measurement, **44**, 399-425 (2011).

[108] M. Heinonen and L. Uusipaikka, "An apparatus for testing humidity sensors at low temperatures," in Proc. Tempmeko 2004, Vol. 1 ed. by D. Zvizdic (LPM/FSB, Zagreb, 2005) 669-675.

[109] A.L. Buck, "New equations for computing vapor pressure and enhancement factor," J. Appl. Meteorol. **20**, 1527-1532 (1981).

I

Publication I

A. Lamminpää, T. Hieta, J. Envall and E. Ikonen, "Reliable Determination of Optical Fiber Nonlinearity Using Dispersion Simulations and Improved Power Measurements", IEEE J. Lightwave Tech. **25**, 527-532 (2007).

Reliable Determination of Optical Fiber Nonlinearity Using Dispersion Simulations and Improved Power Measurements

Antti Lamminpää, Tuomas Hieta, Jouni Envall, and Erkki Ikonen

Abstract—We have improved the accuracy of the continuous-wave self-phase modulation method for measuring the nonlinearity of optical fibers. Evaluation of the measurement uncertainty shows that the most significant source of uncertainty is the measurement of fiber-optic power. However, chromatic dispersion can also have a significant effect on the apparent results if it is not taken properly into account. We demonstrate means to achieve an expanded uncertainty of 2% (coverage factor $k = 2$) for the measurement of the nonlinear coefficient n_2/A_{eff}. Also, the metrological aspects related to the determination of the nonlinear coefficient and the measurement uncertainty are discussed.

Index Terms—Optical fiber dispersion, optical fiber measurements, optical Kerr effect, photodetectors.

I. INTRODUCTION

THE NONLINEAR refractive index n_2 is one of the key parameters that define the data transmission rate limits for modern optical telecommunication systems in terms of used optical power and spacing of wavelength channels in wavelength-division-multiplexed systems [1], [2]. The interest for studying the nonlinear properties of optical fibers has now also been extended to various types of single-mode fibers (SMFs) [3]–[7], where dispersion and nonlinear properties can differ significantly from one type to another.

As the severity of the nonlinear effects is dependent on the intensity distribution inside the fiber, it is convenient to use the nonlinear coefficient n_2/A_{eff} to represent the magnitude of this phenomenon. For the time being, the methods to standardize the nonlinearity measurements of optical fibers are under study [8]. The direct continuous-wave self-phase modulation (CW SPM) method is the measurement that is applied most. Also, the need for careful uncertainty analysis in the determination of n_2/A_{eff} is evident, since, for instance, the deviations in the final report of the International Telecommunication Union, Telecommunication Standardization Sector (ITU-T) intercomparison were on the order of several percents [6]. Even the four laboratories, all using the CW SPM method, did not succeed in having a remarkably better agreement between one another.
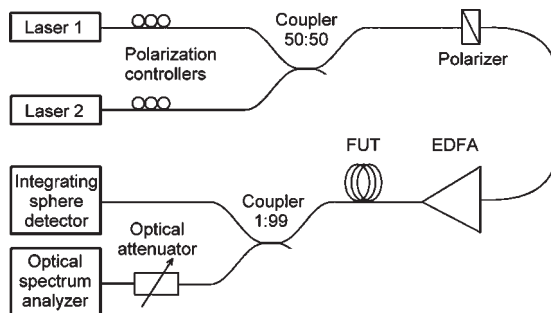
Fig. 1. Measurement setup of CW SPM method.

The recent development of various techniques has not brought the results of participating laboratories any closer to one another as the agreement levels of earlier comparisons [8]–[15] have not improved significantly. The common problem for these comparisons is that the measurement uncertainties of the participating laboratories are not evaluated.

In this paper, we present improvements on the CW SPM method in order to increase its accuracy and repeatability. The major source of uncertainty is typically the determination of optical power launched into the fiber under test (FUT). For this purpose, we have built and characterized a Spectralon-coated integrating sphere detector for high fiber-optic power [16]. Second, in order to take the effects of dispersion into account, we have combined measurements of the CW SPM method with numerical simulations [17]. This brings improvements by a factor of three in the uncertainty of the determination of n_2/A_{eff} [5], [7]. As a final outcome, we demonstrate a measurement setup for n_2/A_{eff} with an expanded uncertainty of 2% ($k = 2$) and discuss issues related to the accurate determination of fiber nonlinearity.

II. OPERATIONAL PRINCIPLE OF CW SPM METHOD

In our measurements, we utilize the CW SPM method outlined in Fig. 1. Two continuous-wave external cavity diode lasers are operated around 1550 nm with wavelength spacing of 0.3 nm. The laser beams are set to have the same linear polarization using polarization controllers and a polarizer after the beams are combined. The signal is then amplified and launched into the FUT. The optical power is measured at the end of the tested fiber using the 99% branch of the coupler.

The total attenuations of the coupler, splice connection, and tested fiber are taken into account by carefully characterizing their attenuation as well as the reflection from the fiber end.

When a high optical power at the two laser wavelengths is launched into the FUT, sidebands lying symmetrically around fundamental wavelengths are generated due to self-phase modulation. The nonlinear phase shift φ_{SPM} of the signal can be obtained from the measurement of the intensity ratio I_0/I_1 of the fundamental wavelength to the first-order sideband [4], [5], i.e.,

$$\frac{I_0}{I_1} = \frac{J_0^2(\varphi_{\mathrm{SPM}}/2) + J_1^2(\varphi_{\mathrm{SPM}}/2)}{J_1^2(\varphi_{\mathrm{SPM}}/2) + J_2^2(\varphi_{\mathrm{SPM}}/2)}. \tag{1}$$

In (1), J_n is the Bessel function of nth order. The nonlinear coefficient n_2/A_{eff} can then be found from the relation [4], [5]

$$\frac{n_2}{A_{\mathrm{eff}}} = \frac{\lambda_0 \text{ (in meters)}}{4\pi L_{\mathrm{eff}} \text{ (in meters)}} \left(\frac{\varphi_{\mathrm{SPM}} \text{ (in radians)}}{P_{\mathrm{AVG}} \text{ (in watts)}} \right) \tag{2}$$

where λ_0 is the center wavelength in a vacuum, L_{eff} is the effective fiber length, and P_{AVG} is the average optical power. The above analysis does not take into account that the apparent values for n_2/A_{eff} depend on the measurement conditions in the presence of fiber dispersion. It neglects the effects of dispersion by assuming that the nonlinear coefficient can be solved directly from the slope of the nonlinear phase shift as a function of optical power [4], [7]. In order to take dispersion into account, simulations based on the nonlinear Schrödinger equation (NLSE) [2] are combined with measurements. This approach is suitable for various measurement conditions and fiber types in order to attain high measurement accuracy.

III. POWER MEASUREMENTS

The measurement of optical power launched into the FUT is the major source of uncertainty in the determination of fiber nonlinearity. In (2), P_{AVG} is the most demanding quantity, directly affecting the value of n_2/A_{eff}, to be accurately determined. With many commercial power meters, it is possible to reach uncertainty levels of only a few percents at the best. For instance, in our previous measurement setup, the total expanded uncertainty $(k=2)$ of 6.4% was dominated by the uncertainty of 5.4% in power measurement [7]. Therefore, it is important to pay special attention to the design or selection of the optical power meter in order to reach satisfactory uncertainty levels.

The improvement in optical power measurement is achieved by using a precision fiber-optic detector built and characterized in our laboratory [16]. The detector consists of a Spectralon-coated integrating sphere (diameter of 50.8 mm) equipped with a fiber adapter and an InGaAs photodiode. The power responsivity of the sphere detector is traceable to the cryogenic radiometer. The angular and spatial variations in power responsivity as well as the aging of the sphere in high power use have been found negligible. In order to extend the scale realization of high fiber-optic power up to 650 mW, the linearity of the power responsivity of the sphere detector was studied using the ac/dc method [18]. The ac/dc method determines the derivative
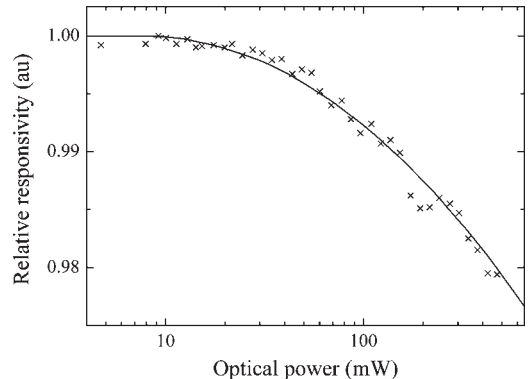

Fig. 2. Nonlinearity of spectral power responsivity of the integrating sphere detector at 1550-nm wavelength. Crosses indicate measured nonlinearities at each power level, and the second-order polynomial curve is fitted to the measurement data.

of the response versus power curve at each dc power level using a small-amplitude sinusoidal ac modulation.

Test measurements with different aperture diameters in front of the InGaAs photodiode revealed that the nonlinear power responsivity of the integrating sphere detector, presented in Fig. 2, is almost completely originating from the properties of the InGaAs photodiode. Although the nonlinearity could be reduced by using a smaller aperture in front of the InGaAs photodiode [19], it was decided to apply the correction in Fig. 2 instead since a smaller detector aperture would reduce the signal levels.

The expanded uncertainty $(k=2)$ in high fiber-optic power measurements is 0.93% at power levels below 100 mW [16], [20], and for higher power levels, up to 650 mW, it is 1.3%. As the power measurement is performed after passage through the FUT, the attenuations of the fiber connection, coupler, and studied fiber have to be taken into account. This adds an additional uncertainty component in the determination of fiber-optic power, which is highly dependent on the repeatability of the optical connectors. With splices, the repeatability can be, depending on the fiber type, in the order of ~0.01 dB (0.23%) compared to, e.g., FC/PC optical connectors with repeatability of ~0.3 dB (7.1%). Therefore, splices are used for all connections between the power meter and the forward end of the FUT to minimize the uncertainty originating from the determination of the attenuation between the optical power meter and the fiber front end.

IV. SIMULATIONS OF FIBER DISPERSION

A. Simulations of Light Propagation in Optical Fiber

Originally, the CW SPM method neglects the effects of dispersion [4]. It has been concluded that this can cause a measurement error of several percents, depending on the measurement conditions [5], [7]. To overcome this problem, we have combined measurement results with numerical simulations. In this modeling of light propagation in the fiber, we use NLSE [2], [21] to calculate the nonlinear phase shift experienced by the fundamental dual-frequency signal. Our implementation
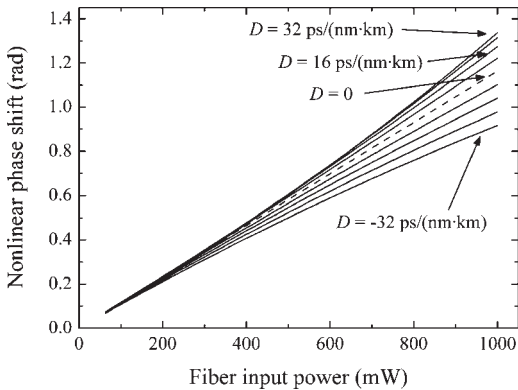
Fig. 3. Simulated effects of dispersion on nonlinear phase shift. The dashed straight line represents the condition where the fiber dispersion is set to zero. In all simulations, fiber length was set to 500 m, wavelength difference to 0.3 nm, and $n_2/A_{\text{eff}} = 2.9 \cdot 10^{-10}$ W^{-1}. Only the dispersion parameter is either increasing or decreasing with steps of 8 ps/(nm · km) from one simulation to another.

Fig. 4. Fit to the nonlinearity data of 500-m-long SMF when dispersion ($D = 16$ ps/(nm · km)) is taken into account (solid black line). If the dispersion is neglected in simulations, the result of fitting is significantly worse, as presented by the dashed dark grey curve. The dotted grey curve, using the right-hand side scale, represents the relative difference between the two simulated phase shifts with and without dispersion.

[17] in MATLAB is based on the split-step Fourier method [2], allowing flexible adjustment of various measurement parameters such as chromatic dispersion, attenuation, fiber length, wavelength difference, and launched optical power. Finally, the best-fit solution for n_2/A_{eff} is found using the least-squares method in the comparison of simulated and measured phase shift curves.

The magnitude of dispersion effects on the results of nonlinearity measurement depends on other measurement parameters. Therefore, it is impossible to generate a straightforward correction factor, even for well-known fiber types. For instance, the simulated effect of fiber dispersion on nonlinear phase shift curves is presented in Fig. 3. The dashed straight line represents the condition where the fiber dispersion is set to zero. This condition is also equal to the assumption on which the equations of the conventional CW SPM method are based. The simulated phase shift curves lying around the zero-dispersion curve differ from the adjacent simulations only by the value of the dispersion parameter by steps of 8 ps/(nm · km). In all simulations, the fiber length was set to 500 m, the wavelength difference to 0.3 nm, and $n_2/A_{\text{eff}} = 2.9 \cdot 10^{-10}$ W^{-1}. If the curve with $D = 16$ ps/(nm · km) is further inspected, we can clearly see that fiber parameters corresponding to standard SMFs can already differ significantly compared to the case where dispersion is neglected. Also, in different measurement conditions, the effect of fiber dispersion on nonlinear phase shift curves will be different. However, by comparing measured nonlinear phase shift values with simulated ones, calculated with NLSE, reasonably better agreement can be achieved as compared with the conventional CW SPM method that neglects the effects of fiber dispersion.

B. Combination of Simulations and Measurements

In the CW SPM method, phase shift is measured as a function of fiber input power. In the conventional approach of the CW SPM 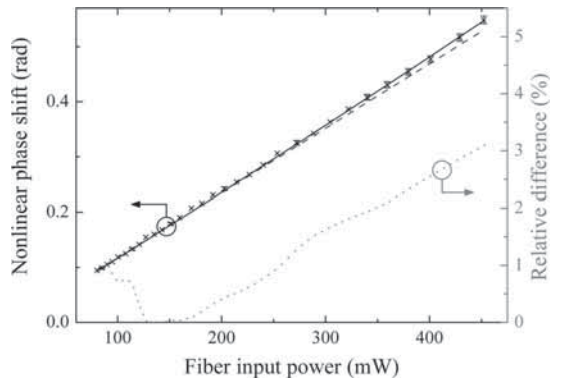method, nonlinear phase shift curves are expected to be straight lines, and therefore, the apparent value of n_2/A_{eff} should not depend on the applied optical power. However, in the presence of fiber dispersion, the measurement conditions will affect the apparent results of n_2/A_{eff}, causing significant deviation between apparent and true values. This effect can be taken into account by determining the fiber dispersion and using the appropriate dispersion model in simulations for the FUT.

With SMFs having anomalous dispersion, phase shift curves bend upward [7]. This is the case in Fig. 4, where the measured phase shift curve at different power levels is bending upward.

The solid black curve in Fig. 4, representing the best fit for the measurement results, is plotted with the measurement results (crosses) by using the values $n_2/A_{\text{eff}} = 2.9 \cdot 10^{-10}$ W^{-1} for the nonlinear coefficient and $D = 16$ ps/(nm · km) for the dispersion parameter. If the dispersion is neglected, and only (1) and (2) are used, the fitting of measurement results will lead to an error of a few percents in n_2/A_{eff}. For comparison, the dashed dark grey curve is simulated with the same value of $n_2/A_{\text{eff}} = 2.9 \cdot 10^{-10}$ W^{-1} but with $D = 0$. This clearly shows that without taking dispersion into account, we end up overestimating the values of n_2/A_{eff} with fibers having anomalous dispersion. The opposite effect will occur in the case of normal dispersion.

For example, if the effects of dispersion would be neglected in the results presented in Fig. 4, the value of n_2/A_{eff} is overestimated by 2.3%. Also, clearly better agreement by 60% between measured and calculated phase shift curves can be achieved in the least-square sense if the measurement results are combined with simulations utilizing NLSE instead of calculations neglecting the effects of dispersion.

V. MEASUREMENT RESULTS AND UNCERTAINTY ANALYSIS

A. Uncertainty Analysis

The reliability of the uncertainty analysis [22] is based on the traceability of the individual quantities and estimations of the

TABLE I
UNCERTAINTY BUDGET (95% LEVEL OF CONFIDENCE) FOR THE CW SPM
METHOD WITH RELIABLE MEASUREMENTS OF HIGH FIBER-OPTIC
POWER AND APPROPRIATE CORRECTION FOR THE
EFFECTS OF DISPERSION

Uncertainty component	Uncertainty (%)
Power measurement P_{AVG}	1.5
Simulated effects of fiber dispersion	0.5
Optical spectrum analyzer $I_0/I_1 \rightarrow \varphi_{\text{SPM}}$	1.2
Wavelength uncertainty λ_0	0.1
Fiber length L	0.4
Expanded uncertainty ($k = 2$)	2.0

relative errors of the measurement instruments. For instance, in the case of optical power, the traceability chain limits the minimum uncertainty of transfer and working standards. If uncalibrated instruments are used, significant systematic errors can occur in the determination of fiber nonlinearity as the nonlinear phase shift is directly proportional to the value of the optical power (2). The fiber-optic power can be measured directly from the output end of the fiber with expanded uncertainty ($k = 2$) of 0.93% up to 100 mW [16], [20] and 1.3% up to 650 mW. The uncertainty component due to the determination of the attenuation of the splice and coupler, between the optical power meter and the front end of the FUT, is 0.7%. This results in the total power measurement uncertainty component of 1.5% in Table I.

The value of n_2/A_{eff} is determined by comparing the measured and simulated phase shifts using the least-squares method. The main advantage of this technique is that the effects of dispersion can be taken into account, and because of this, a systematic error of couple of percents can be avoided. Determination of the fiber dispersion, dispersion slope, and the fitting itself is thus estimated to induce an uncertainty component of only 0.5%. The accuracy in the determination of fiber dispersion is not directly transferred to the uncertainty in n_2/A_{eff} but depends also on other measurement parameters. Simulations utilizing NLSE provide a tool to take the effects of dispersion into account. Otherwise, with especially long fibers or high optical power, the errors can be remarkable. If special fibers with greatly different dispersion properties are studied, uncertainty contributions as low as 0.5% might be difficult to achieve.

Also, other sources of uncertainty need consideration while the measurement results are analyzed. The relative measurement capability of the optical spectrum analyzer (OSA) can become critical. If the linearity of the spectral power responsivity of the OSA is not considered, it can also cause systematic errors that may easily become significant. This is important especially in measurements where the nonlinear sideband signal I_1 is weak compared with the fundamental signal I_0, and practically the whole dynamic range of the OSA is used. As an outcome, the uncertainty component of 1.2% is introduced by measurement of the intensity ratio.

A reasonable accuracy in the determination of the used wavelength and fiber length can be obtained by various means. For the determination of wavelength, we use a wavelength

meter that is traceable to molecular transitions of rubidium and iodine. The corresponding uncertainty in Table I is 0.1%. For the fiber length, mechanical measurement has been found to be most convenient. If the method is used for deployed fibers, another way to determine fiber length is needed. This has to be taken into account while the uncertainty budget is evaluated. For mechanical length measurements, the corresponding uncertainty of 0.4% is included in the determination of n_2/A_{eff}.

The total expanded uncertainty in Table I has been improved from 6.4% ($k = 2$) in [7] to 2.0% by replacing the commercial power meter with a more reliable detector and utilizing NLSE simulations of fiber dispersion with the measurement results.

B. Measurements for SMFs With Different Fiber Parameters

We performed test measurements for two SMFs (ITU-T G.652) having different dopants in the core and cladding. With these modifications in the composition of fibers, their nonlinear properties were slightly altered. Between repetitive measurements, the measurement setup was completely dismounted, and fibers were respliced to the measurement setup.

When dispersion is taken into account, the results of the measurements are found to be insensitive to the measurement conditions, such as fiber length and wavelength spacing. The data in Table II show that if dispersion is not taken into account, the apparent results for n_2/A_{eff} depend on sample lengths, and we will have systematic errors of over 2% in the determination of the nonlinear coefficient. Both fibers have a dispersion parameter of 16 ps/(nm · km) and a dispersion slope of 0.08 ps/(nm² · km). Due to dispersion, values for nonlinear phase shift φ_{SPM} and nonlinear coefficient n_2/A_{eff} vary, depending on the measurement parameters. Only for ∼1000-m-long SMFs did the apparent results of the two techniques intersect [7]. This is also visible in Fig. 5, where especially the result for the 500-m-long SMF is affected, as the linear fit differs significantly from the case when dispersion is present. The accuracy of the simulation based on NLSE in the determination of n_2/A_{eff} is relatively insensitive to the error in the determination of fiber dispersion. For instance, even a 5% error in the determination of fiber dispersion affects by less than 0.1% the apparent value of n_2/A_{eff} with SMFs.

VI. CONCLUSION

At the moment, the determination of the nonlinear coefficient n_2/A_{eff} of optical fibers is mainly limited due to optical power measurement and fiber dispersion. The issues related to power measurement traceability and uncertainty analysis need careful consideration, when the aim is better agreement between different laboratories and measurement methods.

It is evident that high-accuracy fiber-optic detectors are needed to improve uncertainty in the determination of fiber nonlinearity. A good solution for this problem is a fiber-optic detector based on the integrating sphere and a mounted InGaAs photodiode. It is capable of measuring high optical power without any external attenuator and therefore offers better repeatability as the number of fiber connections is reduced.

TABLE II
RESULTS FOR TWO SMFs WITH DIFFERENT CORE AND CLADDING COMPOSITIONS

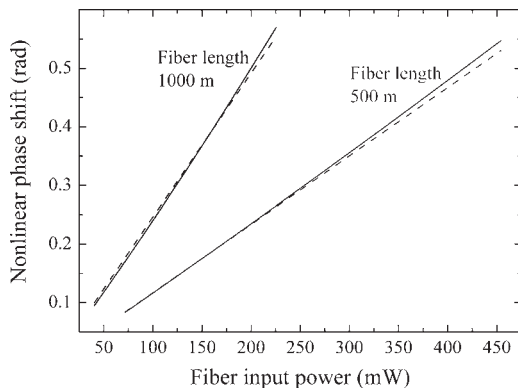|	Nonlinear coefficient n_2/A_{eff} ($10^{-10} \cdot$ W^{-1})		
	Dispersion taken into account	Dispersion neglected	Difference for analysis techniques (%)
Fiber 1 sample 500 m	2.78 ± 0.03	2.85	2.27
Fiber 1 sample 1000 m	2.74 ± 0.03	2.74	0.12
Fiber 2 sample 500 m	2.91 ± 0.03	2.97	1.99
Fiber 2 sample 1000 m	2.93 ± 0.03	2.93	-0.15

Fig. 5. Simulated phase shift curves for fiber lengths of 500 and 1000 m having $n_2/A_{\mathrm{eff}} = 2.9 \cdot 10^{-10}$ W^{-1}. Solid curves are simulated with dispersion parameter $D = 16$ ps/(nm · km) and for the dashed curves $D = 0$.

We also demonstrate a method that can be easily used to take into account the effects of dispersion during data analysis by using NLSE to model the nonlinear phase shift and the nonlinear coefficient. These improvements do not modify the basic idea of the direct CW SPM method but are easily implemented to already existing measurement setups. The technique also allows flexible adjustment of the measured fiber length, wavelength spacing of the dual-frequency signal, fiber dispersion, and launched optical power. Therefore, the method could possibly be exploited with other types of fibers if appropriate dispersion equations are selected. However, this can significantly affect the uncertainty component arising from dispersion effects. It is also reasonable to expect that the same approach would improve the accuracies of other techniques used to measure the nonlinearity of optical fibers.

REFERENCES

[1] D. Marcuse, A. R. Chraplyvy, and R. W. Tkach, "Effect of fiber nonlinearity on long-distance transmission," *J. Lightw. Technol.*, vol. 9, no. 1, pp. 121–128, Jan. 1991.

[2] G. P. Agrawal, *Nonlinear Fiber Optics*, 3rd ed. San Diego, CA: Academic, 2001.

[3] L. Prigent and J.-P. Hamaide, "Measurement of fiber nonlinear Kerr coefficient by four-wave mixing," *IEEE Photon. Technol. Lett.*, vol. 5, no. 9, pp. 1092–1095, Sep. 1993.

[4] A. Boskovic, S. V. Chernikov, J. R. Taylor, L. Gruner-Nielsen, and O. A. Levring, "Direct continuous-wave measurement of n_2 in various types of telecommunication fiber at 1.55 μm," *Opt. Lett.*, vol. 21, no. 24, pp. 1966–1968, Dec. 1996.

[5] K. Nakajima, T. Omae, and M. Ohashi, "Conditions for measuring nonlinear refractive index n_2 of various single-mode fibres using cw-SPM method," *Proc. Inst. Electr. Eng.—Optoelectron.*, vol. 148, no. 5/6, pp. 209–214, Oct. 2001.

[6] Y. Namihira, "ITU-T round robin measurement for nonlinear coefficient (n2/Aeff) of various single mode optical fibers," in *Tech. Dig. Symp. Opt. Fiber Meas.*, 2004, pp. 33–36.

[7] A. Lamminpää, T. Niemi, E. Ikonen, P. Marttila, and H. Ludvigsen, "Effects of dispersion on nonlinearity measurement of optical fibers," *Opt. Fiber Technol.*, vol. 11, no. 3, pp. 278–285, Jul. 2005.

[8] ITU, *Definitions and Test Methods for Statistical and Non-Linear Attributes of Single-Mode Fibre and Cable*. ITU-T Rec. G.650.2 (01/2005).

[9] A. Fellegara, M. Artiglia, S. B. Andreasen, A. Melloni, F. P. Espunes, and S. Wabnitz, "COST 241 intercomparison of nonlinear refractive index measurements in dispersion shifted optical fibres at $\lambda = 1550$ nm," *Electron. Lett.*, vol. 33, no. 13, pp. 1168–1170, Jun. 1997.

[10] Y. Namihira, M. Suzuki, R. S. Khera, S. V. Chernikov, and J. R. Taylor, "Interlaboratory fiber nonlinear coefficient measurements of various dispersion shifted fibers at 1550 nm," in *Tech. Dig. 5th Opt. Fibre Meas. Conf.*, 1999, pp. 66–69.

[11] Y. Namihira, "KDD nonlinear coefficient round robin measurements for various dispersion shifted fibres in Japan and U.K.," in *Proc. Symp. Opt. Fiber Meas. Conf.*, 2000, pp. 49–52.

[12] ——, "Nonlinear coefficient round robin measurements for various dispersion shifted fibres in Japan and U.K.," in *Proc. 26th Eur. Conf. Opt. Commun.*, 2000, pp. 97–98.

[13] Y. Namihira and R. Alexander, "Interim report of ITU-T nonlinear coefficient (n_2/A_{eff}) round robin measurement results in Japan," in *Tech. Dig. 6th Opt. Fibre Meas. Conf.*, 2001, pp. 63–66.

[14] Y. Namihira, K. Miyagi, K. Kaneshima, M. Tadakuma, C. Vinegoni, G. Pietra, and K. Kawanami, "A comparison of six techniques for nonlinear coefficient measurements of various single mode optical fibers," in *Tech. Dig. 12th Symp. Opt. Fiber Meas.*, 2002, pp. 15–18.

[15] Y. Namihira, "ITU-T nonlinear coefficient (n_2/A_{eff}) round robin measurements for various optical fibers in Japan, USA, Switzerland and Italy," in *Proc. 29th Eur. Conf. Opt. Commun. and 14th Int. Conf. Integr. Opt. and Opt. Fibre Commun.*, 2003, pp. 636–637.

[16] J. Envall, P. Kärhä, and E. Ikonen, "Measurement of fibre optic power using photodiodes with and without integrating sphere," *Metrologia*, vol. 41, no. 4, pp. 353–358, Aug. 2004.

[17] T. Hieta and A. Lamminpää, *Matlab Source Code for NLSE Simulations*, Jun. 2006. [Online]. Available: http://metrology.tkk.fi/nlse/

[18] E. F. Zalewski and J. Geist, "Solar cell spectral response characterization," *Appl. Opt.*, vol. 18, no. 23, pp. 3942–3947, Dec. 1979.

[19] A. Carrasco-Sanz, S. Martín-López, P. Corredera, M. González-Herráez, and M. L. Hernanz, "High-power and high-accuracy integrating sphere radiometer: Design, characterization, and calibration," *Appl. Opt.*, vol. 45, no. 3, pp. 511–518, Jan. 2006.

[20] J. Envall, A. Andersson, J. C. Petersen, and P. Kärhä, "Realization of the scale of high fiber optic power at three national standards laboratories," *Appl. Opt.*, vol. 44, no. 24, pp. 5013–5017, Aug. 2005.

[21] T. I. Lakoba and G. P. Agrawal, "Effects of third-order dispersion on dispersion-managed solitions," *J. Opt. Soc. Amer. B, Opt. Phys.*, vol. 16, no. 9, pp. 1332–1343, Sep. 1999.

[22] ISO/IEC/OIML/BIPM, *Guide to the Expression of Uncertainty in Measurements*, Jun. 1992, Geneva, Switzerland: Int. Org. Standardizations.

Antti Lamminpää was born in Helsinki, Finland, in 1979. He received the M.Sc. degree in electronics and communications engineering from the Helsinki University of Technology in 2003. His doctoral dissertation was published in December 2006.

In September 2002, he joined the Metrology Research Institute, Helsinki University of Technology, as a Research Assistant. He is currently a Research Scientist and a Project Manager. His research interests include spectroradiometry and nonlinear fiber optics.

Tuomas Hieta was born in Helsinki, Finland, in 1981. He received the M.Sc. degree in electronics and communications engineering from the Helsinki University of Technology in 2005. He is currently working toward the Dr.Sc.(Tech.) degree at the Helsinki University of Technology.

His main research interest is focused on the area of nonlinear fiber optics.

Jouni Envall was born in Hämeenlinna, Finland, in 1976. He received the Dr.Sc.(Tech.) degree in electronics and communications engineering from Helsinki University of Technology, Helsinki, Finland, in 2006. His dissertation was on optical radiometry and its applications in fiber-optic measurements and ultraviolet radiometry.

Erkki Ikonen received the M.Sc. and Dr.Sc.(Tech.) degrees in engineering from the Helsinki University of Technology, Helsinki, Finland, in 1982 and 1988, respectively.

Until 1988, he was with the Department of Technical Physics, Helsinki University of Technology, where he was engaged in basic research of experimental physics. From 1988 to 1989, he was with the Electrical Engineering Laboratory, Technical Research Center of Finland. Since 1989, he has been with the Metrology Research Institute, Helsinki University of Technology, where he has been a Professor of measurement science and technology since 1995. His research for the last 15 years has been directed toward development of laser-based measurements, high-accuracy instruments for interferometric length determination, and improved methods for radiometric and photometric measurements.

II

Publication II

T. Hieta and E. Ikonen, "Measurement of Er-Doped Fiber Nonlinearity Using Continuous-Wave Self-Phase Modulation Method", IEEE J. Lightwave Tech. **27**, 2977-2982 (2009).

Measurement of Er-Doped Fiber Nonlinearity Using Continuous-Wave Self-Phase Modulation Method

Tuomas Hieta and Erkki Ikonen

Abstract—The intensity-dependent nonlinear coefficient n_2/A_{eff} of a short Er-doped, amplifying fiber is determined using a method thoroughly studied for measurements of passive fibers. Measurement uncertainty of 3.0% is achieved using modified continuous-wave self-phase modulation method. In addition to metrological aspects, we also discuss limitations and conditions imposed by the Er-doped fiber as compared with the measurement of a pure silica core fiber. The used measurement method is advantageous as compared with other techniques due to its reliability and ease of implementation.

Index Terms—Er, optical fiber measurements, optical propagation in nonlinear media, nonlinear optics.

I. INTRODUCTION

E r-doped fiber amplifiers (EDFAs) have been the standard device for amplification of optical signals in long-haul wavelength-division multiplexed systems after their discovery in the late 1980s. When pushing the limits of current technology by means of increased optical power and tighter wavelength spacing in wavelength multiplexing systems (WDMs), it is evident that nonlinear interactions will become more significant and limiting factors. As a result, the fiber parameters related to nonlinearities of other than standard single-mode fibers have become increasingly important as their properties can vary considerably [1], [2].

Self-phase modulation (SPM), cross-phase modulation (XPM), and four-wave mixing (FWM) are a consequence of intensity-dependent refractive index, also referred as the nonlinear refractive index n_2. It is conventional to express the magnitude of the nonlinearity as nonlinear coefficient n_2/A_{eff}, where A_{eff} is the effective area of the fiber core. Various methods have been used to measure the nonlinear coefficient of a standard single-mode fiber with uncertainty levels reaching 2% [1], [3]. Although there is no good agreement between the results obtained in the study of nonlinear effects originating from EDFAs [4], [5], it is evident that the nonlinearity of Er can have a significant effect on the total system performance [4]. Because of the short interaction length in the EDFA, the conventional measurement methods seem to be insufficient to measure the nonlinear coefficient. So far, a novel method based

on induced grating autocorrelation (IGA) has been the most promising method having an uncertainty at a level of 5% [6].

In this paper, we demonstrate a measurement based on the continuous-wave (CW-SPM) method [3], with some modifications, to determine the nonlinear coefficient of an Er-doped fiber. Several constraints are also discussed when compared to the measurement of standard single-mode fiber. Our final outcome is an easily implemented setup capable of measuring very short Er-doped fiber with standard laboratory equipment with an expanded uncertainty of 3.0% ($k = 2$).

II. MEASUREMENT CONFIGURATION

A. CW-SPM Method

In determining fiber nonlinearity, the easily implementable and accurate CW-SPM has been the most used measurement method since its discovery in 1996 [7]. When two signals with a small wavelength gap, which is usually around 0.3 nm, are launched into a fiber, SPM generates sidebands around the fundamental wavelengths with equal spacing. Equation (1) shows how the nonlinear phase shift φ_{SPM} (in radians) is related to the ratio of the intensity of the first sideband I_1 to the intensity of the fundamental wavelength I_0 [7]

$$\frac{I_1}{I_0} = \frac{J_1^2(\varphi_{\text{SPM}}/2) + J_2^2(\varphi_{\text{SPM}}/2)}{J_0^2(\varphi_{\text{SPM}}/2) + J_1^2(\varphi_{\text{SPM}}/2)} \tag{1}$$

where J_n is the Bessel function of nth order. Using only the first-order factors from the Taylor expansion, (1) can be expressed more illustratively for small φ_{SPM}

$$\frac{I_1}{I_0} \cong \frac{\varphi_{\text{SPM}}^2}{16}. \tag{2}$$

The relative error in the approximation is less than 10^{-4} for φ_{SPM} values up to 0.08, which was not exceeded in our measurements. After determining φ_{SPM}, the nonlinear coefficient can be found from the linear relation

$$\varphi_{\text{SPM}} = \frac{4\pi}{\lambda_0} \frac{n_2}{A_{\text{eff}}} L_{\text{eff}} P_{\text{AVG}} \tag{3}$$

where λ_0 is the center wavelength in vacuum, L_{eff} is the effective fiber length, and P_{AVG} is the average optical power of the dual-frequency beat signal. The fiber length L is related to the effective length by $L_{\text{eff}} = (1 - e^{-\alpha L})/\alpha$, where α is the absorption coefficient of the fiber. Effects of dispersion are completely omitted in (1), (2), and (3), but they can be modeled using nonlinear Schrödinger equation (NLSE) and compensated using simulation [3], [8]. However, when measuring very short fibers with close to normal dispersion properties, the dispersion effects are insignificant [9].
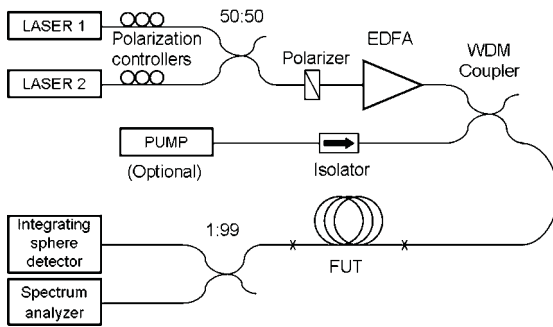
Fig. 1.　CW-SPM measurement setup. Crosses indicate splices between fibers.

B. Measurement Setup

Fig. 1 illustrates our implementation of the CW-SPM method with some additions to the conventional setup. Two tunable commercial external cavity diode lasers (ECDLs) were used as the sources. After combining and setting their outputs to the same polarization state, the signal is amplified using an EDFA. A high-power pump laser at 1480 nm was introduced to this setup to test whether the use of pumped Er-doped fiber would enable more accurate measurement. After the fiber under test (FUT), 99% of the signal is led to the detector. The ratio of the sideband intensities is obtained from the optical spectrum analyzer, which is connected in the 1% arm of the coupler. Splices were used before and after the FUT for better repeatability. The studied Er-doped fiber is manufactured by Liekki Oy.

III. Er-Doped Fiber Characteristics

A. Er-Doped Fiber Nonlinearity Contribution

Although the length of the Er-doped fiber in telecommunication systems is generally short, it can still have an impact on system performance. First of all, the nonlinearity is more severe in Er-doped amplifiers than in normal fiber due to the higher value of the nonlinear coefficient [2]. In addition, L-band optical amplifiers with fiber lengths of over 100 m [10] are needed to have access to longer wavelengths in modern systems. L-band amplifiers have significantly higher contribution to the overall nonlinearity than common EDFAs with fiber lengths ranging from meters to tens of meters. In the case of FWM in WDM systems, studies have shown that the crosstalk in Er-doped fiber is strongly affected by channels far from the original wavelength [4], whereas for a standard fiber, the crosstalk is mainly due to the contribution of the neighboring channels. Considering all of these facts, it is likely that the Er-doping-related nonlinearities will have more significant impact when moving to dense systems and L-band amplification.

B. Fiber Characteristics

Large mode area (LMA) Er-doped fiber Er16-8/125 from Liekki was the fiber under study. The values measured by the manufacturer for the mode-field diameter (MFD) at 1.55 μm

and peak core absorption at 1.53 μm are 9.7 μm and 16.5 dB/m, respectively. Our first approach to measure the nonlinear coefficient of the fiber was to use numerical methods to estimate the signal and pump propagation along the fiber based on a widely used model [11]. The original motivation to measure the Er-doped fiber as an amplifier was to be able to compensate for the high losses of the fiber. To be able to test the model, values of the absorption coefficient α_k and intrinsic saturation power P_k^{IS} were deduced from input–output power measurements at wavelengths between 1510 and 1580 nm with 2 nm spacing and for the pump wavelength of 1480 nm. Although the measurements were done with high-accuracy fiber optic power meters [12], we were unable to fit the model and the actual measurement results of the nonlinear phase shifts well enough, which could be partly caused by omitting pump-induced nonlinear refractive index change [13]. We did not carry out extensive comparison between the difference of the measured and simulated values, but we believe that the difference would be in the order of several percents, which would increase the total uncertainty significantly.

In addition to the modeling problems, spectral hole burning (SHB) could cause major uncertainty if the measurements would be made with the pumped fiber. At the room temperature, SHB is proportional to gain compression and used wavelength [14]. SHB reduces the intensity of the sidebands that directly affects the apparent value of the nonlinear coefficient. Since the depth of the SHB is dependent on the gain compression, the error would be significant because the measurement principle requires high optical power at the fundamental wavelength, and therefore, high compression. As a consequence, it was decided to conduct the measurements only with the high-power input signal at 1.55 μm.

IV. Measurements

A. Measurement Procedure

Contrary to the measurement of standard fibers where the fiber lengths are normally from 100 m up to 1 km, the measurement of an Er-doped fiber has to be made for a relatively short fiber because of the high losses. In addition, the losses vary in the Er-doped fiber depending on the doping concentration and the doping materials, and of course, they vary as a function of the ground-state population along the fiber length. We measured Er-doped fibers with lengths between 1 and 20 m by shortening the fiber with 1 m steps. Narrow spectra around the fundamental wavelengths, fiber optic power, and broadband spectrum for noise analysis were recorded at every fiber length. To study the possible wavelength gap effects, the narrow spectrum was measured with 0.2, 0.3, and 0.4 nm wavelength spacings at every step. The output power of the EDFA was set from 23.5 to 28.5 dBm with 0.25 dB steps. Lower power levels would have been insufficient to create measurable sidebands. Our measurement procedure is based on the discovery that despite the nonlinear behavior of the fiber losses, the nonlinear coefficient of an Er-doped fiber can be determined by using simple relations between measured parameters.
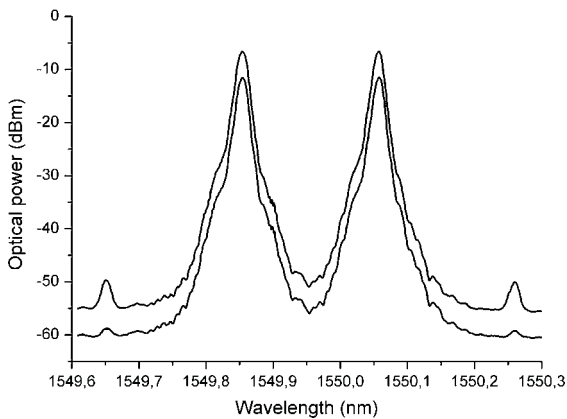
Fig. 2. Measured spectra indicating the fundamental wavelengths and the first sidebands with a 0.2 nm wavelength spacing for 1 m Er-doped fiber. The upper curve represents the spectrum at the maximum input power and the lower at the minimum input power.
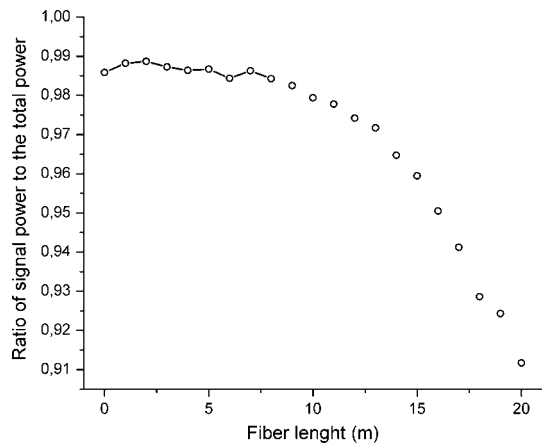

Fig. 3. Ratio of the signal power to the total optical power as a function of Er-doped fiber length. The broadband noise contribution is less than 1.5% up to 8 m.
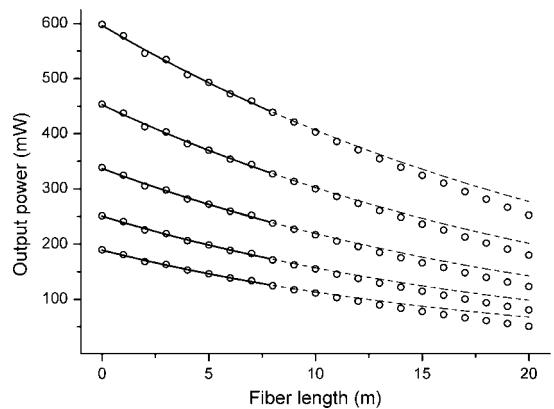

Fig. 4. Power evolution inside the Er-doped fiber for different input powers. Circles indicate measured optical power and the solid lines represent exponential fits up to 8 m. Extrapolated exponential curves based on the parameters obtained from the data up to 8 m are illustrated by the dashed lines.

B. Noise

Narrow-band spectra for 1 m fiber are presented in Fig. 2 obtained from ANDO 6317B spectrum analyzer with a wavelength spacing of 0.2 nm and with high sensitivity. The upper curve is the spectrum at the maximum power of 28.5 dBm and the lower curve at the minimum power of 23.5 dBm. The base noise level was determined at both sides of the first sidebands for each output power level and fiber length. The contribution of noise was removed when calculating the intensity ratio I_1/I_0.

Broad-band noise over the gain band of the Er-doped fiber plays an important role in determining the fiber optic power at signal wavelengths, and therefore affecting the determination of the nonlinear coefficient. As the fiber length is increased, the power from the signal wavelength is absorbed, and is used to amplify noise at wavelengths determined by the Er parameters α_k and P_k^{IS}. Fig. 3 presents the signal power divided by the total power over a broad spectrum at Er gain band using 28.5 dBm output power from the EDFA. Broadband noise measurements were made between 1540 and 1580 nm with a spectrally characterized coupler and power meter. The signal band was determined to include the fundamental wavelengths and the first sidebands. In order to get reliable results, we only used for nonlinear coefficient measurement data up to 8 m, which is marked by the solid line in Fig. 3. After 8 m, the noise starts rapidly increasing, making it hard to compensate for. Since the idea of the measurement procedure was to operate in the passive mode rather than in the active mode, this limit guarantees that no major amplification of the sidebands occurs and that the pump refractive index reduction caused by the charge redistribution is insignificant [13]. At lower output power levels, the ratio starts to drop at shorter fiber lengths but at 8 m; the ratio is still close to the ratio at the maximum output power.

C. CW-SPM Method for Amplifying Fibers

The signal power evolution inside the Er-doped fiber was modeled by exponential functions up to the length of 8 m, which is marked by the solid line in Fig. 4. The fitted values of the

absorption coefficient α_0 range from 0.039 to 0.052 m^{-1}. At longer distances, the exponential fit based on the parameters obtained from the data up to 8 m differs significantly from the measured values due to increasing ground-state population in the Er-doped fiber, and therefore, higher power losses. The five curves represent the loss with EDFA output power ranging from 23.5 to 28.5 dBm with an equal step of 1.25 dB. Although in Fig. 4, the displayed power is the total power inside the fiber, it is spectrally located mainly within a small wavelength window around the fundamental wavelength so that it can be considered to consist almost entirely of the signal power up to the length of 8 m, as shown in Fig. 3.

Clearly, the closer we are to the front end of the fiber, the more it will influence the total measured nonlinearity. By simulating the nonlinear phase shift based on (3) and by using the measured data from Fig. 4, we can determine the nonlinear phase shift as a function of fiber length at different input power levels. The
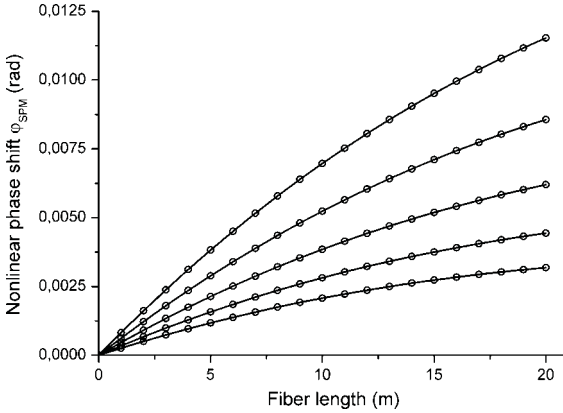
Fig. 5. Simulated nonlinear phase shifts using different fiber input powers with $n_2/A_{\text{eff}} = 3.5 \times 10^{-10}$ W^{-1}. Input power levels are the same as the measured power levels in Fig. 4 for the different curves.
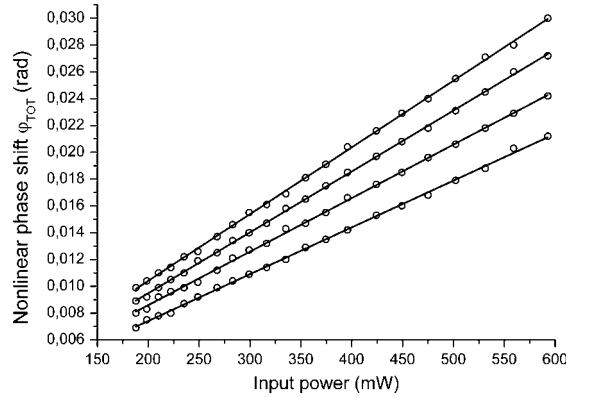

Fig. 6. Measured nonlinear phase shifts at different Er-doped fiber lengths as a function of the optical input power in the Er-doped fiber. Fiber lengths of 0, 2, 4, and 6 m were used where the nonlinear phase shift increases with the fiber length. The wavelength gap is 0.3 nm. Solid lines are fitted by using (9).

simulation results are illustrated in Fig. 5 using the same five input power values as in Fig. 4. In the case of standard fiber, these curves would be very close to straight lines from which the nonlinear coefficient could be easily determined. Despite the highly nonlinear behavior of the nonlinear phase shift as a function of the fiber length, we found out that the nonlinear phase shift as a function of the average input power P_{IN} to the Er-doped fiber shows an almost linear behavior from which the nonlinear coefficient can be determined.

The nonlinear phase shifts determined from the intensity ratio I_1/I_0 by (1) or (2) consist of contributions of each fiber component where the high-power signal propagates. The total measured nonlinear phase shift can be decomposed as

$$\varphi_{\text{TOT}} = \varphi_{\text{SYS}} + \varphi_{\text{FUT}} + \varphi_{\text{END}} \tag{4}$$

where

$$\varphi_{\text{SYS}} = 2\Gamma_{\text{SYS}} P_{\text{IN}} \tag{5}$$

$$\varphi_{\text{FUT}} = 2\gamma_{\text{FUT}} L_{\text{eff,FUT}} P_{\text{IN}} \tag{6}$$

$$\varphi_{\text{END}} = 2\gamma_{\text{END}} L_{\text{eff,END}} P_{\text{IN}} e^{-\alpha_0 L_{\text{FUT}}} \tag{7}$$

and the nonlinear coefficient is now included in the nonlinear parameter defined as

$$\gamma = \frac{2\pi}{\lambda_0} \left(\frac{n_2}{A_{\text{eff}}} \right). \tag{8}$$

Phase shift φ_{SYS} includes all contributions before the FUT starting from the EDFA, and it is linearly dependent on the input power P_{IN} to the Er-doped fiber. The corresponding proportionality coefficient Γ_{SYS} is constant for all the measurements as the contribution of the system before the FUT is independent of the length of the Er-doped fiber. The nonlinear phase shift φ_{FUT} is the contribution due to the Er-doped fiber. The fiber after the FUT and before the 1:99 coupler determines φ_{END}, which depends on the output power of the Er-doped fiber. The output power in (7) is expressed by P_{IN}, the absorption coefficient α_0, and the Er-doped fiber length L_{FUT}. Unlike in

the case of a standard fiber where the absorption coefficient is constant, now it must be determined for each input power level based on the data presented in Fig. 4. By varying the length of the Er-doped fiber, the contribution of the other fibers can be eliminated and the nonlinear coefficient $(n_2/A_{\text{eff}})_{\text{FUT}}$ related to the Er-doped fiber can be determined from the following equation obtained from (4)–(7)

$$\varphi_{\text{TOT}} = \left[\Gamma_{\text{SYS}} + \gamma_{\text{END}} L_{\text{END}} + \gamma_{\text{FUT}} \frac{\left(1 - e^{-\alpha_0 L_{\text{FUT}}}\right)}{\alpha_0} \right.$$
$$\left. + \gamma_{\text{END}} L_{\text{END}} \left(e^{-\alpha_0 L_{\text{FUT}}} - 1\right) \right] P_{\text{IN}} \tag{9}$$

where $L_{\text{END}} = L_{\text{eff,END}}$ for a short piece of fiber after FUT.

D. Measurement Results

The measured nonlinear phase shifts φ_{TOT} as a function of input power P_{IN} for fiber lengths $L_{\text{FUT}} = 0, 2, 4$, and 6 m are illustrated in Fig. 6 including fits to the data obtained by using (9). The input power was corrected for the losses of the splices and for the 1:99 coupler as well as for the broadband noise, as presented in Fig. 3. Also, the power reflected from the fiber end at the power detector due to the mismatch of the refractive indexes was taken into account. The slopes of the fits in Fig. 6 include contributions from (5)–(7) since each of these phase shifts is proportional to P_{IN}. The dependence of α_0 on P_{IN} is taken into account in (9). The sum of the first two terms in (9) is determined by the result with $L_{\text{FUT}} = 0$, after which γ_{FUT} can be solved from (9). The fitted horizontal lines in Fig. 7 give the resulting nonlinear coefficient of the Er-doped fiber. Measurement results with varying wavelength spacing are presented numerically in Table I. We obtain $n_2 = 2.53 \times 10^{-16}$ cm^2/W by taking the average of the nonlinear coefficient values from Table I and by using the MFD given by the manufacturer to calculate the effective area. It is higher than the average value obtained by the ITU-T comparison for silica fiber ($n_2 = 2.16 \times 10^{-16}$ cm^2/W,
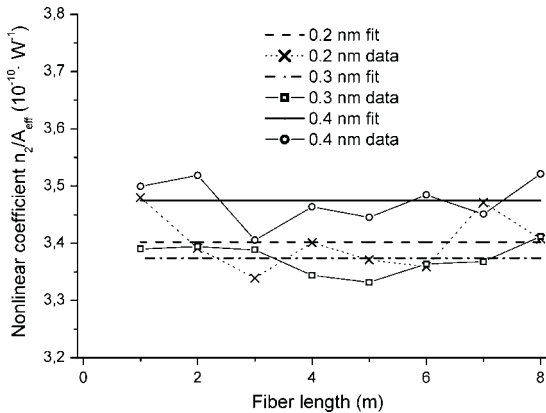
Fig. 7. Measurement results of the nonlinear coefficient for the Er-doped FUT as a function of the fiber length $L_{\rm FUT}$.

TABLE I
RESULTS FOR DIFFERENT WAVELENGTH SPACINGS

Wavelength gap (nm)	Nonlinear coefficient $n_2/A_{\rm eff}$ $(10^{-10} \cdot {\rm W}^{-1})$	Difference from the mean value (%)
0.2	3.402	-0.44
0.3	3.374	-1.26
0.4	3.475	1.70

[1]) as expected due to the doping [2]. Previously values between 1.8×10^{-16} and 3.0×10^{-16} cm²/W for n_2 have been obtained with fibers having various Er, Ge, and Al dopant concentrations [2]. Our result is close to the middle of the range of values reported in [2].

V. UNCERTAINTY ANALYSIS

Generally, the measurement of the fiber optic power produces the dominant uncertainty component [3], [6] in the measurements of the nonlinear coefficient. In order to lower the uncertainty due to the splices, we conducted measurements of the splice loss compared with the estimated splice loss from the Sumitomo T-37 fusion splicer. The measurements showed good correlation between the estimates and the measured values with a small offset that needed to be added to the estimated splice loss. This correction was applied at each fiber length independently. Fig. 4 indicates that the power values at 2 and 4 m are lower than the trend line that can be explained by the estimated losses being 0.04 and 0.06 dB, respectively, while the estimated losses given by the splicer for the other fiber lengths are typically between 0.00 and 0.02 dB.

Our power measurement procedure is similar to our earlier research [3] except for the splice loss uncertainty part. The measured splice loss repeatability was ~0.03 dB (~0.7%) for the splices between the Er-doped fiber and the standard fiber, which is larger than the repeatability for the splices between standard fibers ~0.01 dB (~0.23%) [3]. This results in a slightly higher

TABLE II
UNCERTAINTY BUDGET ($K = 2$) FOR ACCURATE DETERMINATION OF THE NONLINEAR COEFFICIENT OF AN ER-DOPED FIBER

Uncertainty component ($k=2$)	Uncertainty (%)
Power measurement $P_{\rm AVG}$	1.6
Optical spectrum analyzer $I_1/I_0 \rightarrow \varphi_{\rm SPM}$	2.5
Erbium doped fiber length L	0.5
End fiber nonlinear coefficient	0.15
Wavelength uncertainty	0.02
Expanded uncertainty ($k = 2$)	3.0

total expanded uncertainty ($k = 2$) of 1.6% for the power measurement, which includes the uncertainty components of the splice loss and the coupler loss after the FUT (see Table II).

The most difficult part of this measurement method is to accurately determine the relative intensity of the first sidebands. In both cases, the intensity ratio of the carrier and the first sideband is over 40 dB. It is demanding to evaluate the uncertainty of the optical spectrum analyzer including noise originating from the fiber, but an estimate of 2.5% seems to be reasonable even at the lowest power levels considering the linearity of ± 0.05 dB specified by the manufacturer.

When measuring short fibers, the uncertainty of fiber length becomes important. After each 1 m piece cut from the fiber, the length of the remaining fiber was measured as well as the part that needed to be cut from the output port of the WDM coupler. At each step, the passive fiber part was shortened by approximately 1 cm. Fortunately, the nonlinear coefficient of the standard fiber is only ~70% of that of the Er-doped fiber in our measurements, and therefore, the error it produces is also reduced. We conclude that a conservative estimate of 0.5% uncertainty related to the fiber length would be appropriate, since accurate measurements within a couple of millimeters can be easily made with conventional tools.

The nonlinear coefficient of the fiber before the coupler is estimated to be 2.5×10^{-10} W^{-1} based on earlier research on standard fibers [1]. The length of the fiber before the coupler was 70 cm at the final stage when the length of the FUT was 0. An error of 10% in the nonlinear coefficient will produce an error of ~0.15% in the measured nonlinear coefficient of the Er-doped fiber, which is small as compared to other uncertainty components. The contribution of the exponential power drop is ~1.3% to the nonlinear coefficient.

The uncertainty in determining the center wavelength λ_0 is very small with respect to other uncertainty components. A conservative estimate of 0.02% corresponds roughly to ± 0.3 nm variation in λ_0. We achieved a total expanded uncertainty of 3.0% ($k = 2$) from the uncertainty budget presented in Table II.

VI. DISCUSSION AND CONCLUSION

While the measurement technology for silica fiber nonlinearity has matured, and consists of several methods [1], the methods to determine the nonlinear coefficient of an Er-doped fiber are still mostly unexplored. Clearly, the methodology used with silica fibers can be used to study also Er-doped fibers, but this is the first time when a reliable result is presented using

a method which can be implemented with standard laboratory equipment.

The measurement of fiber optic power is also a major uncertainty component when measuring Er-doped fibers. In addition, one must take several constraints into account that are related to Er-doped fibers. One major difference is the high attenuation due to Er at 1.55 μm, which limits the usable fiber length. We showed that the noise induced by the fiber can be harmful in two different ways. In long fibers, the Er begins to act as an amplifier, increasing unwanted signals out of the wavelength band of interest. Noise can induce error in the intensity of the first sideband when measuring short fibers with low power levels if it is not taken into account. One possible solution to overcome the problem with the high dynamic range requirement for the spectrum analyzer would be to insert a passive fiber spool between the EDFA and the FUT to increase the amplitude of the first sidebands to a level where the measurement would be more reliable. The fiber before the 1:99 coupler should be kept short to decrease the uncertainty originating from the power drop. We have also shown that using a pumped fiber, modeling difficulties and spectral hole burning could induce significant uncertainty to the total uncertainty if they are not characterized accurately.

We managed to measure the nonlinear coefficient of the Er-doped fiber with an uncertainty of 3.0% ($k = 2$). Although a lot of time consuming measurements were made in our study, a reasonable uncertainty can be attained with much less measurements in terms of fiber lengths and used power levels. The developed method could be also implemented as a part of a fiber characterization procedure, since most fibers need to be measured anyway at different lengths to obtain other crucial fiber parameters such as loss and effective area.

ACKNOWLEDGMENT

REFERENCES

[1] Y. Namihira, "ITU-T round robin measurement for nonlinear coefficient (n_2/A_{eff}) of various single mode optical fibers," in *Tech. Dig. Symp. Opt. Fiber Meas.*, 2004, pp. 33–36.

[2] F. A. Oguama, A. M. Johnson, and W. A. Reed, "Measurement of the nonlinear coefficient of telecommunication fibers as a function of Er, Al, and Ge doping profiles by using the photorefractive beam-coupling technique," *J. Opt. Soc. Amer. B*, vol. 22, pp. 1600–1604, Aug. 2005.

[3] A. Lamminpaa, T. Hieta, J. Envall, and E. Ikonen, "Reliable determination of optical fiber nonlinearity using dispersion simulatuions and improved power measurements," *J. Lightw. Technol.*, vol. 25, no. 2, pp. 527–532, Feb. 2006.

[4] Y. Liu, S. Burtsev, S. Tsuda, S. P. Hegarty, R. S. Mozdy, M. Hempstead, G. G. Luther, and R. G. Smart, "Four-wave mixing in EDFAs," *Electron. Lett.*, vol. 35, no. 24, pp. 2130–2131, 1999.

[5] K. Song and M. Premaratne, "Effects of SPM, XPM, and four-wave-mixing in L-band EDFAs on fiber-optic signal transmission," *IEEE Photon. Technol. Lett.*, vol. 12, no. 12, pp. 1630–1632, Dec. 2000.

[6] H. Garcia, A. M. Johnson, F. A. Oguama, and S. Trivedi, "New approach to the measurement of the nonlinear refractive index of short (< 25 m) lengths of silica and erbium-doped fibers," *Opt. Lett.*, vol. 28, no. 19, pp. 1796–1798, Oct. 2003.

[7] A. Boskovic, S. V. Chernikov, J. R. Taylor, L. Gruner-Nielsen, and O. A. Levring, "Direct continuous-wave measurement of n_2 in various types of telecommunication fiber at 1.55 μm," *Opt. Lett.*, vol. 21, pp. 1966–1968, Dec. 1996.

[8] G. P. Agrawal, *Nonlinear Fiber Optics*, 3rd ed. San Diego, CA: Academic Press, 2001.

[9] A. Lamminpää, T. Niemi, E. Ikonen, P. Marttila, and H. Ludvigsen, "Effects of dispersion on nonlinearity measurement of optical fibers," *Opt. Fiber Technol.*, vol. 11, pp. 278–285, Jul. 2005.

[10] G. J. Pendock, S. Y. Park, A. K. Srivastava, S. Radic, J. W. Sulhoff, C. L. Wolf, K. Kantor, and Y. Sun, "The contribution to cross-phase modulation in L-band WDM systems from erbium-doped fiber amplifiers," *IEEE Photon. Technol. Lett.*, vol. 11, no. 12, pp. 1578–1580, Dec. 1999.

[11] A. A. M. Saleh, R. M. Jopson, J. D. Evankow, and J. Aspell, "Modeling of gain in erbium-doped fiber amplifier," *IEEE Photon. Technol. Lett.*, vol. 2, pp. 714–717, Oct. 1990.

[12] J. Envall, P. Kärhä, and E. Ikonen, "Measurement of fibre optic power using photodiodes with and without integrating sphere," *Metrologia*, vol. 41, pp. 353–358, Jul. 2004.

[13] H. Garcia, A. M. Johnson, F. A. Oguama, and S. Trivedi, "Pump-induced nonlinear refractive index change in erbium- and ytterbium-doped fibers: Theory and experiment," *Opt. Lett*, vol. 30, no. 11, pp. 1261–1263, Jun. 2005.

[14] M. Bolstyansky, "Spectral hole burning in erbium-doped fiber amplifiers," *J. Lightw. Technol.*, vol. 21, no. 4, pp. 1032–1038, Apr. 2003.

Tuomas Hieta was born in Helsinki, Finland, in 1981. He received the M.Sc. degree in electronics and communications engineering in 2005 from Helsinki University of Technology, Espoo, where he is currently working toward the Ph.D. degree.

His current research interests include nonlinear fiber optics and laser spectroscopy.

Erkki Ikonen received the M.Sc. and Dr. Tech. degrees in engineering from the Helsinki University of Technology, Espoo, Finland, in 1982 and 1988, respectively.

Until 1988, he was with the Department of Technical Physics, Helsinki University of Technology, where he was engaged in basic research of experimental physics. From 1988 to 1989, he was with the Electrical Engineering Laboratory, Technical Research Center of Finland, where he has been a Professor of measurement science and technology at the Metrology Research Institute, Helsinki University of Technology, since 1995. His current research interests include the development of laser-based measurements, high-accuracy instruments for interferometric length determination, and improved methods for radiometric and photometric measurements.

III

Publication III

T. Hieta, M. Vainio, C. Moser and E. Ikonen, "External-cavity lasers based on a volume holographic grating at normal incidence for spectroscopy in the visible range", Opt. Commun. **282**, 3119-3123 (2009).

External-cavity lasers based on a volume holographic grating at normal incidence for spectroscopy in the visible range

T. Hieta [a,b,*], M. Vainio [b,c], C. Moser [d], E. Ikonen [a,b]

[a] Helsinki University of Technology, Metrology Research Institute, Otakaari 5 A, P.O. Box 3000, FI-02015 TKK, Espoo, Finland
[b] Centre for Metrology and Accreditation (MIKES), FI-02151, Finland
[c] Frequency and Time Group, Institute for National Measurement Standards, National Research Council of Canada, 1200 Montreal Road, Ottawa, Ontario, Canada K1A 0R6
[d] Ondax Inc., Monrovia, CA 91016, USA

ARTICLE INFO

ABSTRACT

We present two external-cavity diode lasers that utilize a volume holographic grating as the frequency selective feedback element. By using the grating at normal incidence, it is possible to design simple and compact external-cavity diode lasers that have sufficient tunability for molecular spectroscopy. The first design utilizes a long-cavity designed for narrow linewidth and good long-term stability. The laser operates near 635 nm and it has a PZT-controlled tuning range of 28 GHz and a 1-s linewidth of 900 kHz. The second design utilizes a grating attached very close to the laser diode, making the laser compact, robust and easy to operate. The short external-cavity laser operates near 658 nm and it has a linewidth of 30 MHz. Continuous and mode-hop free tuning range of 145 GHz can be obtained by using a simple temperature tuning method.

1. Introduction

Compared to most other lasers, diode lasers are simple to use, inexpensive and small in size. They have become fundamental tools in many fields of optical technology and experimental physics [1], such as optical communications, spectroscopy, and atom optics. In these applications, single longitudinal mode operation, narrow linewidth, broad tuning range and low drifts are generally favorable characteristics. Often these characteristics cannot be met with solitary laser diodes that tend to have broad linewidth, poor frequency stability and limited tuning characteristics. A common technique to improve diode laser properties is to expose the laser to strong and controlled optical feedback from an external reflector. By using external feedback it is possible to increase the laser cavity length and thus decrease the spectral linewidth by a factor of 100–1000 compared to that of a solitary diode laser. Side mode suppression ratio (SMSR) of 30–50 dB and accurate frequency tuning can be achieved by using a frequency selective feedback element, which is usually a diffraction grating in Littrow configuration [2,3] or more conveniently a partly transmitting grating in a similar configuration [4]. It is also possible to use separate optical elements for feedback and frequency selection, e.g., by having an interference filter in an external cavity formed by a mirror [5,6]. Such approach can help to reduce alignment sensitivity of the laser, however at the expense of increased complexity of mode-hop free frequency tuning.

A remaining challenge related to external-cavity diode lasers (ECDL) is to find a design that provides good frequency stability, accuracy and reproducibility without compromising the well-defined tuning characteristics. In general, these favorable properties can be achieved only if mechanical and thermal drifts of the laser cavity are carefully suppressed. Most of the reported ECDL geometries lead to a large mechanical structure, which makes the laser susceptible to mechanical vibrations and thermal gradients. To avoid these problems, we have designed a new external-cavity diode laser based on a compact volume holographic grating (VHG) [7].

While the focus of using the VHGs in laser applications has been in locking and narrowing the linewidth of high-power diode laser bars [8,9], their applicability to spectral narrowing of low-power diode lasers was demonstrated already over 20 years ago [10]. With the introduction of long-term stable holographic grating materials, the interest in VHG-based external-cavity diode lasers has recently re-emerged [7,11].

In this paper we demonstrate that the VHG technology is well suited for designing narrow-linewidth, long-term stable ECDLs that have large mode-hop free frequency tuning range. The basic principle of the laser cavity is schematically shown in Fig. 1a, and the detailed description and characterization of the laser are presented in Sections 2 and 3, respectively. We also discuss a

* Corresponding author. Address: Helsinki University of Technology, Metrology Research Institute, Otakaari 5 A, P.O. Box 3000, FI-02015 TKK, Espoo, Finland.
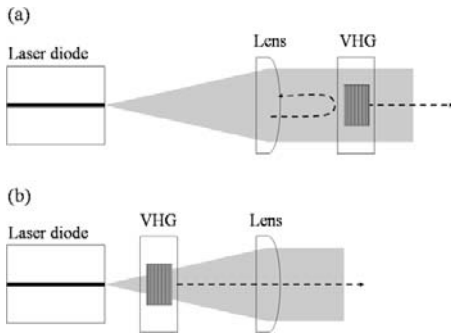E-mail address: tuomas.hieta@tkk.fi (T. Hieta).

Fig. 1. Schematic drawings of the operation principles of the ECDLs. The volume holographic grating (VHG) provides strong feedback for the collimated beam in long-cavity design (a), while in short-cavity design (b), the VHG is placed at close proximity (few tens of micrometers) of the laser diode being able to provide feedback to only small portions of the diverging output beam. The short-cavity laser is compact enough to fit into a standard 9-mm TO-can.

previously introduced compact external-cavity laser in which the VHG is placed in close proximity of the laser diode facet [7]. This design is schematically depicted in Fig. 1b. The suitability of both ECDLs in molecular spectroscopy is demonstrated. The main results are summarized in Section 4, in which we also discuss the possible limitations of this approach.

2. Laser configuration

2.1. Volume holographic grating

Volume holographic gratings are Bragg reflectors that are fabricated by recording the interference pattern of two coherent light fields into a thick photosensitive media that maintains long-term stability of the recorded pattern. (For detailed description of VHGs and their long-term stability, see, e.g., Ref. [7].) The VHGs used in this work are fabricated in the bulk of a glass substrate. The resulting grating is thus protected from contamination and its optical surfaces can be cleaned with the same precautions as ordinary optics. When a light beam is directed into the VHG, it is reflected according to the Bragg condition,

$$\lambda = 2nD\cos(\theta), \tag{1}$$

where λ is the wavelength, n is the bulk refractive index of the VHG media, D is the grating period, and θ is the incidence angle relative to the grating normal. Note that VHG is not a dispersive grating – it simply reflects the light beam at the wavelength that satisfies the condition of Eq. (1). Unlike in the case of diffraction gratings, the wavelength selected by a VHG does not depend on the refractive index of the surrounding air at normal incidence. This feature can help to sustain good long-term stability of an ECDL when operating it in an environment where temperature, pressure, and composition of the laser cavity air may vary [12,13].

Normal incidence ($\theta = 0$) is a convenient choice when using a VHG as the frequency selective component of an ECDL. The laser diode output beam hitting the VHG is reflected directly back to the diode and no additional optical elements, such as mirrors, are needed in the external cavity. (A collimating lens is often used to maximize the beam volume that satisfies the Bragg condition, see Fig. 1.) The wavelength reflected back to the laser diode in the normal-incidence configuration is $\lambda = 2nD$. An advantage of this configuration is that the external cavity can be made simple and symmetrical relative to the optical axis. Symmetrical structure helps to reduce laser's sensitivity to external disturbances and to

mechanical drifts [12]. In Section 3 we will also show that the normal-incidence configuration makes it possible to achieve large mode-hop free frequency tuning range with an ECDL.

One of the most important parameters of VHGs and diffraction gratings is their spectral resolution. Unlike in the case of diffraction gratings, whose resolution is inversely proportional to the beam diameter, the resolution of a VHG is inversely proportional to the interaction length L [14].

$$\Delta\lambda = \frac{\lambda^2}{\pi L} \tag{2}$$

In this work we have used two different VHGs, one designed for 635 nm center wavelength and the other one for 658 nm. Both VHGs have a physical length of 1.5 mm. The effective interaction length is slightly shorter corresponding to a nominal reflection bandwidth (FWHM) of 75 GHz, which is narrow enough to reliably suppress the characteristic longitudinal modes of the solitary diode laser. For comparison, the spectral resolution of the VHGs used in this work is similar to (or better than) that of a typical diffraction grating in the Littrow configuration, and approximately three times better than what can be obtained with narrow-band interference filters [6].

Another important parameter of the VHG is its peak reflectivity, which depends on the modulation depth of the VHG's refractive index pattern [7]. The VHGs can be fabricated with high absolute reflection efficiency, reaching 95% for a 1.5 mm thick VHG. The efficiency does not depend on the light polarization, which simplifies the ECDL design. (Diffraction efficiency of a typical diffraction grating depends on the light polarization and the laser diode orientation has to be adjusted accordingly. Sometimes an intracavity half-wave plate is needed to simultaneously optimize the diffraction efficiency and the diffraction bandwidth [12]). Reflectivity of the front facet of a typical laser diode is high, sometimes up to 30%, which means that a high reflection efficiency of the VHG is required to overcome the oscillations of the solitary laser. On the other hand, if a laser diode with an antireflection-coated front facet is used, a grating reflectivity of 15–25% is often sufficient to ensure reliable operation in a cavity mode determined by the grating. It is worth noting that usually it is not desirable to use grating reflectivity much higher than that required for stable ECDL operation, since high reflectivity compromises the ECDL output power (output beam is extracted through the VHG) and exposes the laser diode output facet to high intensities that can damage the diode.

Because the properties of a VHG, such as its peak reflectivity and reflection bandwidth, are independent of the other parameters of ECDL they can be tailored for a particular application more easily than those of diffraction gratings. For instance, the parameters can be optimized in order to achieve narrow linewidth operation of an ECDL [15]. The possibility of using a small laser beam is particularly interesting, since a small beam size makes the ECDL less sensitive to misalignment of the optical feedback element [5]. However, if the beam is very small, increased divergence reduces reflectivity, increases bandwidth, and can cause a slight deviation in the peak wavelength. Ultimate alignment stability can be obtained by applying a cat's eye configuration, where the feedback strength remains essentially constant for small misalignments of the feedback element. A drawback of the configuration is increased complexity that also makes it more difficult to achieve large mode-hop free frequency tuning. The cat's eye configuration has been previously used with interference filters [5,6] and a modified version of it has been recently demonstrated with VHGs [14].

In this work we have not used the cat's eye configuration but we have utilized the possibility for a small beam size otherwise: In addition to improving alignment stability, the small beam size can be used to reduce the physical length of the external cavity (since a collimating lens with a shorter focal length can be used).

Together with the fact that the VHGs can be made very small in size (e.g. 0.6×0.6 mm^2), this has allowed us to design a compact ECDL cavity that is easy to temperature stabilize. This design is discussed next.

2.2. Laser structure

In this section we give a detailed description of the ECDL that is schematically shown in Fig. 1a. To ensure good performance and small drifts, the laser cavity is designed to be robust, rigid and symmetrical with respect to the optical axis. All of the mechanical parts were made of aluminum. The exploded mechanical structure of the laser is presented in Fig. 2. The length of the structure is 68 mm including the $64 \times 64 \times 13$ mm^3 front and back plates. Above the bottom plate lays a 10-W Peltier element, which is used to control the temperature of the laser diode with 10-mK precision. The diode is mounted on a circular plate, which is screwed to the inner enclosure. The diode laser, which is not shown in Fig. 2, is a commercially available antireflection-coated InGaAlP device (SDL-7501-G1) with a nominal power and wavelength of 10 mW and 635 nm, respectively. A collimated beam is produced with an aspheric, antireflection coated lens ($f = 4.5$ mm, NA = 0.55, Thorlabs, C230TM-B).

The VHG (Ondax) is held in a separate mount comprised of three PZT-elements (Thorlabs, AE0203D04F). The antireflection-coated front facet (with residual reflectivity of $\ll 1\%$) of the laser diode allowed us to use a VHG with a rather modest reflectance of $\sim 35\%$. This was proved to be high enough to provide good laser stability and narrow linewidth, and yet low enough to avoid damaging of the laser diode. Since the output beam is transmitted through the VHG (whose input and output ends are parallel), the beam pointing is always parallel to the output beam of the laser diode, independent of the VHG angle. Moreover, as the VHG is oriented at normal incidence with respect to the collimated output beam, also the lateral shift of the beam position can be virtually neglected. For a 1.5 mm thick VHG made from glass ($n = 1.45$) the lateral displacement of the output beam as a function of VHG angle is ~ 0.47 µm/mrad. In our design this effect is negligible since the tilting angle around normal incidence is limited to some tenths of a mrad.

An O-ring is set between the VHG structure and the inner enclosure to provide some level of hermeticity in the laser cavity and to be able to optimize the angle of the VHG by using three adjustment screws mounted trough the front plate. By using the three PZT-ele-

ments for fine tuning, it is possible to synchronize the cavity length tuning with the grating angle tuning in order to get a mode-hop free tuning range that is broader than the free spectral range of the cavity [16]. The optical length of the laser cavity, 15 mm, was selected so that it would be long enough to achieve a narrow linewidth (<1 MHz), while ensuring a large longitudinal mode spacing of ~ 10 GHz, which helps to minimize the probability of cavity mode hops.

The entire laser structure is placed within an outer enclosure that is sandwiched between the end plates. The end plates are connected to each other with four invar rods (not shown in the figure). O-rings are used in between the enclosure and the end plates in order to obtain some level of hermeticity and also to provide a buffer to allow stress-free thermal expansion. The laser output beam is extracted through a window (not shown in the figure), which is antireflection coated and slightly tilted in order to avoid residual optical feedback to the laser. The use of the outer enclosure helps to reduce laser temperature fluctuations and damps the variations due to ambient pressure that could otherwise deform the sealed laser cavity and hence cause laser frequency deviations.

3. Performance

3.1. Long-cavity ECDL

Passive stability (no feedback loop) of the laser design described in Section 2.2 was determined by measuring both the short-term and long-term frequency stability. Low-noise electronics [17] were used for the laser current supply, for temperature control, and for the PZT control voltages throughout the measurements. To determine a practical 1-s linewidth, the laser frequency was recorded in the time domain with an oscilloscope using a Fabry–Perot interferometer (FPI) as the frequency discriminator. Fig. 3 shows the resulting 900 kHz linewidth with a Gaussian fit, indicating good short-term stability. Single-mode operation and good spectral purity of the laser were confirmed using the FPI and a grating spectrum analyzer (Ando 6315). The side-mode suppression ratio was measured to be better than 35 dB when operating the laser close to the center wavelength of the laser diode gain curve.

To determine the long-term stability of the free running laser, the laser frequency was tuned to the linear part of the slope of an iodine absorption line that was used as a frequency-to-amplitude converter. The laser beam passed a 20 cm iodine absorption cell three times, and the cell was at ambient temperature (20 °C)
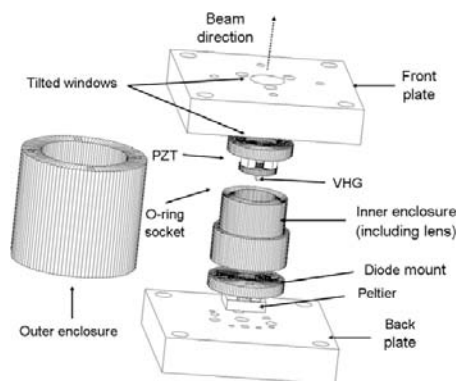

Fig. 2. Exploded view of the long-cavity ECDL structure. The laser diode, the two output windows and four invar rods are not shown in the figure. All the components are in scale.
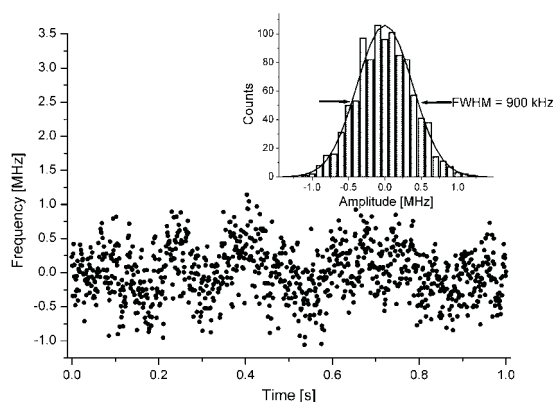

Fig. 3. Practical 1-s linewidth (inset) of the 635 nm ECDL calculated from the laser frequency fluctuations in the time domain including a Gaussian fit.

corresponding to a gas pressure of 30 Pa. Laser frequency, ambient pressure, power and temperature were recorded with 11 s intervals using 150 ms of averaging. An 8-hour measurement result is presented in Fig. 4 showing good passive long-term stability with the maximum deviation of the laser frequency being only 80 MHz. We performed several measurements where ambient pressure variations were in the order of 1 hPa, but no clear pressure dependency of the laser frequency was observed. The measurements were done in a temperature controlled room where the temperature remained stable within 0.1 °C around an average value of 20 °C. No temperature dependency of the laser frequency could be determined in these conditions. Such dependency can be, however, expected to small due to the temperature stabilization of the ECDL cavity. (The inner enclosure of the cavity is in good thermal contact with the laser diode mount that lays on a Peltier element, see Fig. 2. The end plates are connected to each other with invar rods that have small thermal expansion coefficient.)

Fig. 5 shows the measured frequency tuning range of the laser. The tuning was done by tilting the VHG with the three PZT elements, while the relative magnitudes of the voltage signals fed into the PZTs were empirically optimized for mode-hop free operation. The frequency scale was obtained with the FPI peaks and iodine transitions [18]. The continuous mode-hop free tuning range is ~28 GHz, which is almost three times the FSR of the external laser cavity. It is possible that the actual tuning range is even broader since the sweep was limited by the PZT-element displacements. To the best of our knowledge, this is the first demonstration that large mode-hop free tuning can be achieved also with VHGs by tilting the grating angle in a standard ECDL configuration. In principle the feedback would be lost immediately when the VHG is tilted, but in practise beam divergence ensures that there are some rays that satisfy the Bragg condition and that are reflected back to the laser diode when the VHG is slightly tilted.

Broader tuning range can be achieved by varying the drive current and the temperature of the laser. At the ambient temperature of 20 °C, the tuning slopes were −3 GHz/mA (0.004 nm/mA) and −9.3 GHz/K (0.0125 nm/K) for the drive current and temperature, respectively. A total tuning range of ~70 GHz was obtained by varying the temperature and current, which is in agreement with the 75 GHz bandwidth of the VHG. Because the bandwidth of the VHG is relatively small compared to the FSR of the solitary diode laser, the desired wavelength can be obtained with good reproducibility. With certain temperature and current settings, we obtained the same mode and thus the same wavelength every time. This was
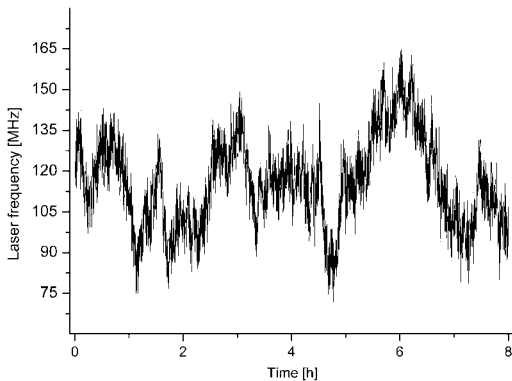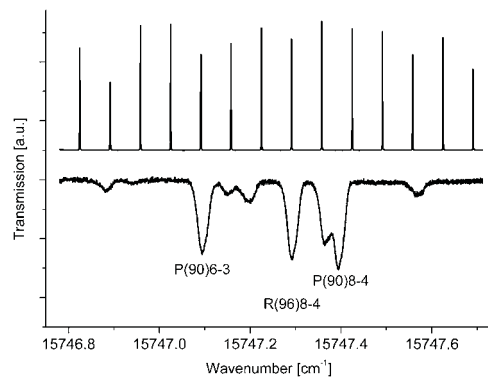

Fig. 5. Continuous and mode-hop free scan of 28 GHz of the long-cavity ECDL including Fabry–Perot interferometer (FSR = 2 GHz) peaks (above). The R(98)8-4 line of I2 absorption spectrum was used as frequency reference in the stability measurement reported in Fig. 4.

verified during the measurement period. Altogether, the reproducibility of the laser was observed to be better than, e.g., with the ECDL reported in [17] (which occasionally jumped to an adjacent mode of the laser diode).

3.2. Short-cavity ECDL

The new ECDL described above in Sections 2.2 and 3.1 is designed especially for metrology and atomic physics. However, in gas detection applications, particularly in industry, larger mod-hop-free frequency scanning ranges are favorable. In such applications it is often desirable to have a laser design that is compact and simple to assemble and use. These requirements can be met with the short-cavity ECDL that is schematically shown in Fig. 1b. The laser consists of a laser diode (Sanyo DL-6147-040) with standard off-the shelf coating, estimated at 15%, that emits at 658 nm, and of a high efficiency VHG (~75%) that is attached a few tens micrometers to the diode. The laser equipped with the VHG fits into a standard 9-mm TO-can. Temperature of the can is controlled to within 10 mK using a Peltier element, and the output beam is collimated using an antireflection coated lens (f = 4.5 mm), which is placed after the VHG. Obviously, the fractional power reflected back to the laser diode by the VHG is smaller in this configuration than in the long-cavity ECDL, since the laser beam incident to the VHG is not collimated and hence only a small portion of the angularly spread output power satisfies the Bragg condition. The feedback is, however, strong enough to ensure reliable laser operation at the frequency determined by the VHG, and the side modes of the laser diode are suppressed by more than 35 dB. Due to the short external cavity the laser linewidth is not significantly narrowed compared to that of a typical single-mode diode laser. We measured a linewidth of ~30 MHz using a scanning FPI with a ~0.5 ms sweep over the laser line.

An advantage of the short external cavity is that the laser frequency can be tuned without mode hops over a large range simply by varying the laser temperature. This tuning method is demonstrated in Fig. 6, which shows an example of the measured Doppler broadened iodine spectrum [18], demonstrating a continuous and mode-hop free scan of ~145 GHz and suitability of the laser for gas detection applications. In addition to the iodine spectrum, an FPI was also used as a frequency marker to confirm the tuning range and to ensure that there are no mode hops during the scan. The observed mode-hop free tuning range is significantly larger than the reflection bandwidth of the VHG. This can be explained

Fig. 4. Measured long-term frequency fluctuations of the free-running 635 nm ECDL. The data were recorded every 11 s using 150 ms averaging. (The noise appears large due to the short averaging time of each sample).
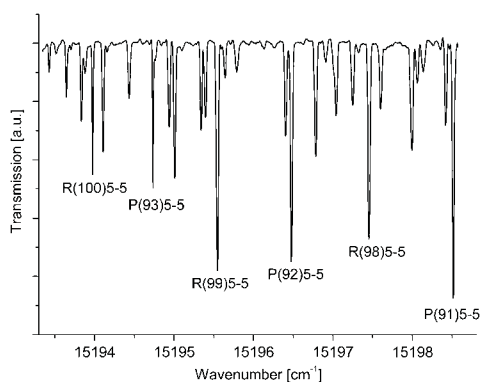
Fig. 6. Iodine spectrum as a function of laser frequency tuning for the short-cavity ECDL, demonstrating a continuous and mode-hop free scan of 145 GHz. Some of the iodine transitions are identified for clarity.

by the fact that the entire laser can, also the VHG, is kept at the same temperature; the temperature scan thus shifts not only the frequency of the laser cavity, but also that of the VHG. Both the laser diode and VHG frequencies have negative temperature coefficients so they tune to the same direction. The mode-hop free tuning range is the largest reported so far for a VHG-stabilized laser diode, and it is equivalent to that of typical DFB and DBR lasers. Since the DFB and DBR lasers are commercially available only for wavelengths longer than ~700 nm, the short-cavity VHG-based ECDL is an interesting choice for applications such as holography and gas detection especially in the visible.

4. Discussion and conclusions

We have presented a novel external-cavity diode laser that utilizes a volume holographic grating as the optical feedback element. The laser was designed for good passive frequency stability and it is insensitive to variations of ambient pressure. The laser has a 1-s linewidth of 900 kHz and it is hence well suited for high resolution spectroscopy. Continuous and mode-hop free tuning range of 28 GHz was achieved, demonstrating that synchronous tuning of the ECDL cavity length and grating angle works well also with VHGs despite their non-dispersive nature (as compared to diffraction gratings).

The new ECDL reported in this paper was designed particularly for applications in metrology and atom physics where a single atomic or molecular transition needs to be reliably addressed. For such applications, the demonstrated total tuning range, 70 GHz, of the laser frequency is sufficient. However, it is obvious that as such the design is not suitable for applications that require wide tuning of the laser wavelength. Although this limitation arises from the narrow reflectance bandwidth and non-dispersive

nature of the VHGs, it can be overcome by different designs. So far two solutions to this tuning problem have been presented: One solution utilizes a VHG in a retroreflector configuration, in which one or more mirrors are needed in the ECDL cavity in addition to the VHG [14,19]. Another possibility is to use a chirped VHG, in which the grating period varies in a direction transversal to the laser beam, hence allowing laser wavelength tuning to be done by simply translating the VHG [20]. Both of these methods can provide wavelength tuning of >1 nm, at least [14,19,20].

A more simple way of extending the frequency tuning range, although at the expense of increased linewidth, is to attach the VHG in immediate proximity of the laser diode output facet. This short-cavity ECDL design makes it possible to keep the laser diode and VHG at the same temperature, hence allowing quasi-synchronous temperature tuning of their frequencies. We have shown that such temperature tuning method can provide continuous and mode-hop free frequency scans of 145 GHz. It is possible that even larger scans are possible with improved matching of the temperature tuning coefficients of the laser diode and VHG, although such possibility was not explicitly studied in this work. The small size, ease of use, and large continuous frequency tuning range make the short-cavity ECDL ideal for spectroscopic applications that require measurement of multiple molecular transitions simultaneously. The ECDLs reported in this work were designed to operate at 635 nm and 658 nm, but the same designs can be adapted to virtually any visible or near-infrared wavelength above 350 nm where diode lasers are available.

References

[1] C.E. Wieman, L. Hollberg, Rev. Sci. Instrum. 62 (1991) 1.
[2] M.W. Flemming, A. Mooradian, IEEE J. Quantum Electron. 17 (1981) 44.
[3] A.S. Arnold, J.S. Wilson, M.G. Boshier, Rev. Sci. Instrum. 69 (1998) 1236.
[4] M. Merimaa, H. Talvitie, P. Laakkonen, M. Kuittinen, I. Tittonen, E. Ikonen, Opt. Commun. 174 (2000) 175.
[5] P. Zorabedian, W.R. Trutna Jr., Opt. Lett. 13 (1988) 826.
[6] X. Baillard, A. Gauguet, S. Bize, P. Lemonde, Ph. Laurent, A. Clairon, P. Rosenbusch, Opt. Commun. 266 (2006) 609.
[7] G.J. Steckman, W. Liu, R. Platz, D. Schroeder, C. Moser, F. Havermeyer, IEEE J. Select. Topics Quantum Electron. 13 (2007) 672.
[8] B.L. Volodin, S.V. Dolgy, E.D. Melnik, E. Downs, J. Shaw, V.S. Ban, Opt. Lett. 29 (2004) 1891.
[9] Y. Zheng, H. Kan, Opt. Lett. 30 (2005) 2424.
[10] P. Mills, R. Plastow, Electron. Lett. 21 (1985) 648.
[11] F. Kroeger, I. Breunig, K. Buse, Appl. Phys. B (2008) 10.1007/s00340-008-3290-1.
[12] H. Talvitie, A. Pietilainen, H. Ludvigsen, E. Ikonen, Rev. Sci. Instrum. 68 (1997) 1.
[13] X. Baillard, A. Gauguet, S. Bize, P. Lemonde, Ph. Laurent, A. Clairon, P. Rosenbusch, Opt. Commun. 266 (2006) 609.
[14] C. Moser, L. Ho, F. Havermeyer, Opt. Express 16 (2008) 16691.
[15] H. Loh, Y. Lin, I. Teper, M. Cetina, J. Simon, J.K. Thompson, V. Vuletić, Appl. Opt. 45 (2006) 9191.
[16] M. de Labachelerie, G. Passedat, Appl. Opt. 32 (1993) 269.
[17] M. Vainio, M. Merimaa, E. Ikonen, Meas. Sci. Technol. 16 (2005) 1305.
[18] S. Gerstenkorn, P. Luc, Atlas du Spectre d'Absorption de la Molécule d'Iode, Editions du CNRS, Paris, 1978.
[19] B. Jacobsson, J.E. Hellström, V. Pasiskevicius, F. Laurell, Opt. Express 15 (2007) 1003.
[20] K. Seger, B. Jacobsson, V. Pasiskevicius, F. Laurell, Opt. Express 17 (2009) 2341.

IV

Publication IV

T. Hieta and M. Merimaa, "Spectroscopic measurement of air temperature", Int. J. Thermophys. **31**, 1710-1718 (2010).

Spectroscopic Measurement of Air Temperature

T. Hieta · M. Merimaa

Abstract   Optical dimensional measurements have to be corrected for the refractive index of air. The refractive index is conventionally calculated from parameters of ambient air using either Edlén or Ciddor equations or their modified versions. However, these equations require an accurate knowledge of ambient conditions and especially the temperature of air. For example, to reach an uncertainty of 10^{-7} in dimensions, the air temperature has to be known at $\sim$100 mK level. This does not necessarily cause problems in a stable laboratory environment. However, if measurements are done outdoors or in an industrial environment, variations in temperature can be very rapid and local temperature gradients can cause significant error if not taken into account. Moreover, if the required distance is long, the temperature over the whole measurement path can be impractical or impossible to determine at sufficient temporal or spatial resolution by conventional temperature measurement techniques. The developed method based on molecular spectroscopy of oxygen allows both lateral spatial and temporal overlap of the temperature measurement with the actual distance measurement. Temperature measurement using spectroscopy is based on a line intensity ratio measurement of two oxygen absorption lines, previously applied for measurements of high temperatures in flames. The oxygen absorption band at 762 nm is a convenient choice for two-line thermometry since the line strengths are practical for short- and long-distance measurements and suitable distributed feedback lasers are commercially available. Measurements done on a 67 m path at ambient conditions demonstrate that the RMS noise of 22 mK, or 7.5×10^{-5}, near 293 K using 60 s measurement time can be achieved, which is to our knowledge the best reported resolution.

T. Hieta · M. Merimaa (✉)
Centre for Metrology and Accreditation (MIKES), 02151 Espoo, Finland
e-mail: mikko.merimaa@MIKES.fi

T. Hieta
Aalto University School of Science and Technology, 02150 Espoo, Finland

1 Introduction

Tunable diode-laser-based gas temperature sensors have been studied extensively during recent years [1–6]. Much of the research has been focused on combustion applications at elevated temperatures. Before room temperature semiconductor diode lasers were available, the laser sensors were based on impractical ring dye lasers and the measurements were performed in the UV range [1]. Nowadays semiconductor lasers provide robust and tunable light sources in the near-infrared (NIR) region and they are often used to probe absorption lines of oxygen or water that are common substances in combustion gases [2–6]. Especially in hot and rapidly changing combustion processes, optical techniques provide several benefits compared to more intrusive methods. Spectroscopic sensors offer fast response, excellent lateral spatial resolution, and overlap with minimal perturbation to the existing system. Acoustic thermometry has similar benefits as laser-based devices, but it cannot be used accurately to measure long path lengths.

Although the previous research has been focused on hot temperature and combustion applications, the same principles apply also to the measurements done in ambient air. One apparent application where good overlap, fast response, and good resolution are needed in temperature measurement is determination of the refractive index of air. Length measurement based on laser interferometry is practical and an accurate technique for dimensional metrology in a stable environment. The length scale is based on the wavelength of the laser which has to be calculated using the vacuum wavelength of the laser and the refractive index of the medium. Most measurements are done at atmospheric conditions where variation in the temperature, pressure, humidity, and CO_2 content affect the refractive index. In a well-controlled laboratory environment, these variations are in general low and measurement uncertainties in the order of 10^{-7}, or better, can be obtained. However, if measurements are done in an industrial environment or outdoors, fluctuations of ambient conditions can be several orders of magnitude larger, thus significantly increasing the measurement uncertainty. The acoustic method based on speed-of-sound measurement of an ultrasound burst signal can be also used to determine the effective air temperature with low uncertainty [7]. Echoes, beam spreading, and absorption, however, make it more suitable for shorter distances compared to the developed spectroscopic method.

This paper presents an experimental realization of a two-line room-temperature thermometer based oxygen A-band $b^1\Sigma_g^+ - X^3\Sigma_g^-$ weak transition near 762 nm. The thermometer is based on a simple and effective wavelength-multiplexed direct absorption method with amplitude modulation and normalized lock-in detection. Accurate and fast temperature measurement is demonstrated over 67 m absorption path. Rationale for the selected transitions is given, and general criteria for optimal line pair selection are discussed briefly. Two distributed feedback (DFB) lasers are used to scan two absorption transitions as well as the absorption free baseline that need to be measured to gain increased accuracy. The measurement system is designed to have a movable measurement head with fiber connections. The normalization scheme used

in the setup effectively cancels small drifts in laser output power and interferences caused by the optics before the measurement head.

2 Theory

The transmission of light through an absorptive medium is governed by the Beer–Lambert law, which is given by

$$I = I_0 \exp(-\alpha), \tag{1}$$

where I is the transmitted intensity and I_0 is the initial intensity. The absorption coefficient α can be written as

$$\alpha = S(T)g(v, T, P)nl, \tag{2}$$

where $S(T)$ is the temperature-dependent absorption transition line strength, $g(v, T, P)$ is the normalized (area = 1) function which describes the shape of the absorption line at a given frequency v, n is the molecular absorber number density, and l is the absorption path length. The total absorption spectrum of the medium is the sum of the spectra of individual molecular transitions. The absorption line-shape function is a function of temperature, pressure, and perturbing molecules (collision broadening). The line broadening effects can be divided into Doppler broadening and pressure broadening. Doppler broadening is dependent on the frequency, mass of the molecule, and on the temperature. At normal temperatures and at low pressures, Doppler broadening is the dominant broadening mechanism resulting in a Gaussian profile of the line-shape function. At atmospheric pressure, the dominant mechanism is pressure broadening. It results in a Lorentzian profile for the line-shape function which is quite close to a Gaussian profile near the center, but having a stronger absorbance far away from the line center. At the region where both broadening mechanisms contribute to the total profile, the line shape must be modeled using a Voigt profile, which is a convolution of Lorentzian and Gaussian profiles. The Voigt profile has been studied extensively, and many accurate analytical approximations have been developed [8,9].

The temperature-dependent absorption transition line strength can be expressed by

$$S(T) = S(T_0)\frac{Q(T_0)}{Q(T)} \exp\left[-\frac{hcE}{k}\left(\frac{1}{T} - \frac{1}{T_0}\right)\right] \times \left[\frac{1 - \exp\left(-hcv_0/(kT)\right)}{1 - \exp\left(-hcv_0/(kT_0)\right)}\right], \tag{3}$$

where $Q(T)$ is the total internal partition sum, E is the lower state energy, h is the Planck constant, k is the Boltzmann constant, and c is the speed of light [10]. The reference temperature, T_0, is 296 K. The center of the spectral-line transition frequency is denoted by v_0. The third term in Eq. 2 accounts for the ratio of Boltzmann populations, and the last term for the effects of stimulated emission, which can be omitted in the visible wavelength region. For two separate absorption transitions having different lower state energies and sharing the same vibrational state, the ratio of the line strengths can be expressed as

$$R = \frac{S_1(T)}{S_2(T)} = \frac{S_1(T_0)}{S_2(T_0)} \exp\left[-\frac{hc\Delta E}{k}\left(\frac{1}{T} - \frac{1}{T_0}\right)\right], \qquad (4)$$

where ΔE is the difference in their rotational state energies. Now the molecular absorber number density can be determined from the measured absorbances and the temperature can be deduced from the ratio of the absorbances using Eq. 4. The molecular number density is not required to determine the temperature if the scale is calibrated with reference temperature sensors, although it can be easily determined from the absorption measurements. The calibration is valid for all measurement devices using the same line pair.

3 Experimental Details

3.1 Line Selection

Fortunately, the center frequencies, line strengths, line-width parameters, and rotational energies for various common atmospheric molecules needed for accurate two-line thermometry are readily available from the HITRAN database [10]. Optimal line selection depends on whether only one laser is used or if it is possible to multiplex two or more lasers to the same absorption path. Additional lasers add complexity and price, but also improve the achievable sensitivity. A single laser limits the available wavelength range, which usually leads to a compromise when selecting lines with high R. The availability of DFB lasers at different wavelengths is also a limiting factor when choosing line pairs in an experimental realization of two-line thermometry. Absorbance of the two lines should be comparable and the absorption over the desirable path length should be in ideal case tens of percents. If the absorbance is higher, the saturation property of Eq. 1 decreases the achievable temperature sensitivity. At low absorbance levels, noise becomes a significant degrading factor to the overall performance. Within the tuning range of the used diode(s), there should be a free spectral window ideally with zero absorbance, which could be used to provide baseline information on internal losses and non-idealities of the system. Free spectral windows are practically nonexistent at ambient conditions when the medium is standard air, but there are still regions where the absorbance is low enough to allow measurement of the baseline with low uncertainty.

The A-band of oxygen near 762 nm is well-suited for two-line thermometry near room temperature at atmospheric pressure. Compared to water, which has multiple strong features in visible and near-IR regions, the oxygen mole fraction can be assumed to stay relatively stable when temperature, humidity, or pressure vary. The A-band has a selection of well-isolated transitions with weak and strong absorbances, making it good for both short- and long-range applications. The band is also practically free from interfering molecular absorptions. Water and hydroxide have some transitions in the region, but they are either out of band or several orders of magnitude weaker than oxygen transitions at standard atmospheric concentrations. Furthermore, high performance DFB and VCSEL lasers are available at this range, thus making it possible to build compact and cost effective measurement systems. The simulated absorption
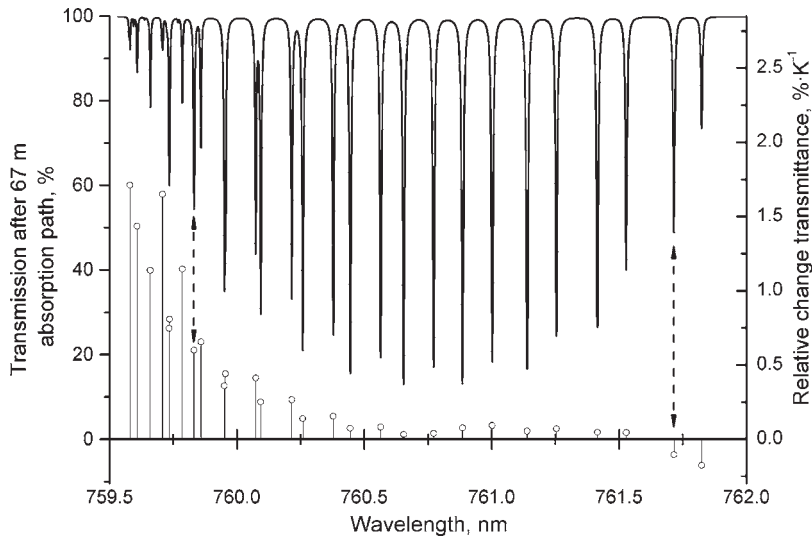
Fig. 1 Oxygen A-band absorption spectrum for a 67 m path in ambient air and relative change in absorption for each transition. Used transitions are marked with *dashed double arrows*

spectrum of the oxygen R-branch is shown in Fig. 1 for a path length of 67 m at standard pressure and temperature (20 °C, 1 atm., 20.95 % O_2). The Voigt profile is used as the line-shape function using an approximation adopted from [8]. The Lorentzian halfwidths are calculated using air broadened halfwidths γ_{air} from HITRAN and by using an approximate equation from [9]. The relative change in absorption for a 1 K increase in temperature is presented for each transition. It can be seen from the figure that the saturated transitions in the middle are not suitable for high sensitivity thermometry when using a 67 m path length. The theoretical sensitivity is $\sim 0.7 \% \cdot K^{-1}$ for the transition marked in the figure, which takes into account the saturation caused by the Beer–Lambert law. The marked transitions are R19-Q20 at 759.831 nm and R1-Q2 at 761.715 nm using HITRAN notation.

3.2 Measurement Setup

The experimental setup is shown in Fig. 2. Two DFB lasers (Eagleyard photonics) are mounted in a thermoelectric cooler used for temperature stabilization. The nominal wavelength for DFB 1 and DFB 2 are 760.7 nm and 761.6 nm, respectively. The tuning range (temperature) for both lasers is $\sim \pm 1$ nm around their nominal wavelengths, making it possible to use almost any line shown in Fig. 1. The half-wave plates before the beam multiplexing are used to match the polarization state of the DFB to the input of the electro-optic intensity modulator (EO-IM, ConOptics). Beam shaping is used to optimize the beam that is focused into a single-mode optical fiber. The light is guided to the measurement head that is located in another laboratory. The output radiation of the fiber is collimated using an achromatic doublet lens (75/f:1.5), which produces a 25 mm low divergence output beam. Part of the output beam is immediately reflected back using a wedged metallic beam splitter. A silicon photodiode (PD B) provides
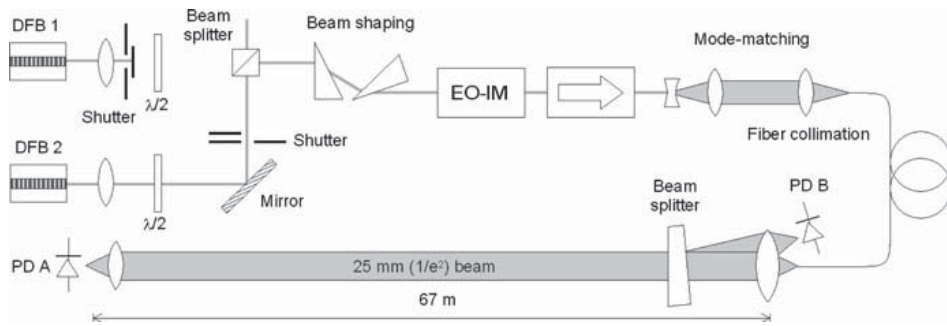
Fig. 2 Schematic of two-line thermometry measurement setup when DFB 2 is active

the reference signal for normalization. The actual absorption is measured with silicon photodiode A (PD A). The optical power at the PD A is ∼1 mW. EO-IM is modulated at 1.4 kHz, and two lock-in amplifiers (SR830) measure the lock-in signal. Each temperature measurement requires a measurement of both absorption peaks and the baseline. The baseline is measured using DFB 2, which is temperature tuned to the free transmission window shown in Fig. 1 just left of the transition used in thermometry. Both lasers are current tuned after each measurement to the center of the absorption peak to compensate for small drifts in electronics or caused by thermal effects. The system is fully automated using Labview software and a data acquisition card.

4 Sensor Demonstration

Temperature measurement is a three-step process. First, the frequency of the DFB 2 is swept by current over the R1-Q2 transition and the peak absorption is determined. Immediately after the sweep, the temperature of the DFB 2 is adjusted to the absorption-free part of the spectrum. Next, the frequency of the DFB 1 is swept over the transition R19-Q20 to determine the corresponding peak absorption. Finally, the frequency of the DFB 2 is swept over the absorption-free part to obtain the baseline for both absorption peaks. The total measurement time for one temperature measurement is close to 60 s. Figure 3 shows a typical result measurement of step one and three using DFB 2. The measurement result from step two is left out for clarity. The time constant of the lock-in amplifier was 30 ms, and the time between consecutive points was ∼50 ms. The frequency sweep of both lasers is set to correspond to approximately ∼0.5 % of the height of the absorption line. The width of the sweep is sufficient to determine the peak value of the absorption line and to allow loose frequency stabilization of the lasers by adjusting the current so that the center of the sweep matches with the line center. A moving average of ten points was used to smooth the data before determining the peak absorption. This causes a small error in the peak value, but the error can be neglected as the measurement is based on a ratio measurement of the two peaks. The small offset is practically the same for both peaks, and we found that the shape of the peaks remained the same over the measurement period of one hundred hours. In theory, a continuous baseline measurement is not necessary in two-line thermometry, but we discovered that the statistical noise of our measurement
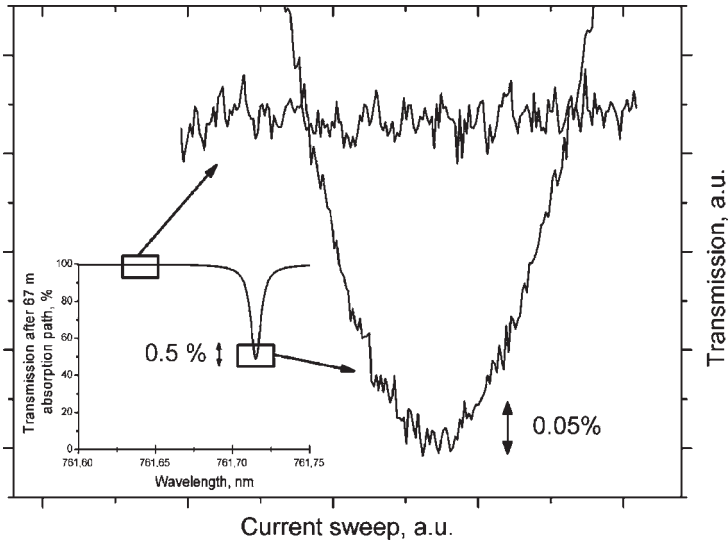
Fig. 3 Typical measurement result of the R1-Q2 transition and the baseline. Two *squares* in the inset are exaggerated for clarity. Portion of the absorption peak height is marked with *vertical double arrows* for scale
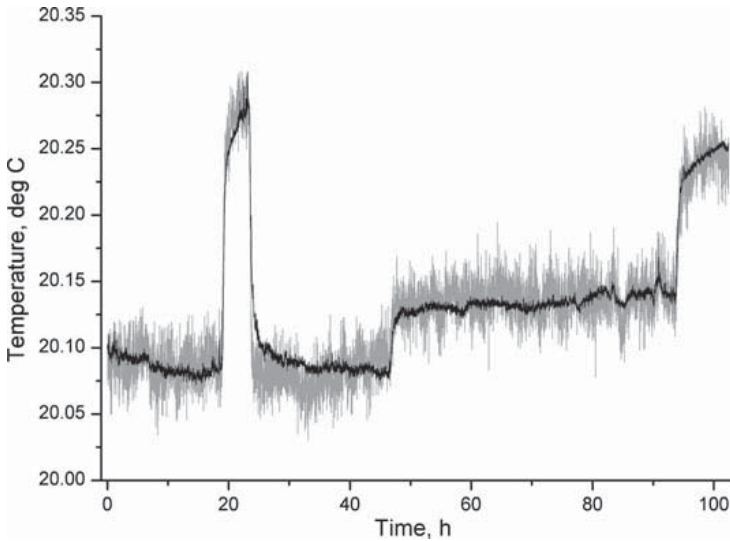
Fig. 4 Result of a 100 h temperature measurement. Raw spectroscopic data are marked with a *gray line*, and an average of seven conventional temperature sensors is marked with a *black line*. Observed temperature changes are made intentionally

system was lower when the baseline information was used. For example, if the ratio R is 1.1, which is close to the ratio of the chosen line pair, a 0.5 % negative offset in the baseline increases the ratio by 0.056 % which is equal to a significant 39 mK increase in temperature.

Raw temperature-measurement data, including all measurement points, for a 100 h measurement period is shown in gray in Fig. 4. The measurement path is placed over

a 30 m long interferometric measurement rail designed for calibration of electronic distance measurement instruments, measuring tapes and poles, and circometers. The laboratory where the 30 m measurement rail is located is approximately 40 m long. To increase the measurement path length, a mirror and double-pass scheme is used to obtain the total 67 m measurement path. We use seven fast conventional temperature sensors distributed evenly over the length of the measurement path as a reference instrument. In principle, the absolute temperature scale could be obtained from the tabulated spectroscopic data. However, the experimental uncertainty in the HITRAN database, which is usually on the order of a few percent for line strength, causes a significant error and therefore the temperature scale is obtained from the reference thermometer. The black line is the average of seven sensors each averaged over 1 s. The laboratory where the measurement was performed has very good temperature control with an adjustable set-point. To investigate the performance of the spectroscopic temperature measurement, we have made step changes to the set-point, that very rapidly affect the temperature of the incoming air. The first step-response test (after 20 h of continuous measurement) was performed to investigate the response speed of the spectroscopic measurement as compared to conventional sensors. There is a significant difference in the response speed, especially when the temperature is adjusted back to the original setting. As expected, the spectroscopic method is much faster compared to the conventional sensors even in the case of a small temperature step to which the conventional sensors react rapidly. The 200 mK step can be considered quite common or even small in environments that are not well temperature controlled. The second and third step-response tests were performed to assess the sensitivity of the system to small temperature changes. The $\sim$40 mK step can be easily resolved, and the calculated RMS noise of the temperature measurement is 22 mK, which may be partially due to actual temperature fluctuations of the air. An empirical pressure correction of -45 mK $\cdot$ mbar^{-1} was used to cancel the variations caused by changes in the ambient pressure.

5 Conclusions

Two-line spectroscopic thermometry has been previously used mainly in high-temperature applications. In this work, we have demonstrated that oxygen can be used as a probe to measure temperature over a relatively long path at normal ambient conditions. The selection of the two absorption lines is discussed, and optimal lines are chosen for the 67 m path length. Well-separated absorption peaks, absorption-free transmission windows, strong- and weak-line strengths, stable concentration, and good sensitivity for temperature changes make oxygen a good choice for a probe molecule. Two DFB lasers were used as laser sources capable of operating at virtually any wavelength of interest thus making it possible to vary the path length while maintaining good sensitivity. We have demonstrated a measurement configuration based on lock-in detection and normalization. A separate measurement head with a fiber connection simplifies measurement arrangements. We have shown that the developed measurement system is capable of measuring rapid changes and small variations in temperature, which are required, for example, in optical dimensional measurements

to compensate for the temperature dependence of the refractive index of air. The RMS noise of the demonstrated measurement system is 22 mK, which corresponds to $\sim 2 \times 10^{-8}$ RMS noise in the refractive index of air.

References

1. A.Y. Chang, M.D. DiRosa, D.F. Davidson, R.K. Hanson, Appl. Opt. **30**, 21 (1991)
2. M.P. Arroyo, R.K. Hanson, Appl. Opt. **32**, 30 (1993)
3. J.T.C. Liu, J.B. Jeffries, R.K. Hanson, Appl. Opt. **43**, 35 (2004)
4. J. Silver, D.J. Kane, Meas. Sci. Technol. **10**, 10 (1999)
5. H. Teichert, T. Fernholz, V. Ebert, Appl. Opt. **42**, 12 (2003)
6. J. Shao, L. Lathdavong, P. Kluczynski, S. Lundqvist, O. Axner, Appl. Phys. B **97**, 3 (2009)
7. V. Korpelainen, A. Lassila, J. Opt. Eng. **43**, 10 (2004)
8. Y. Liu, J. Lin, G. Huang, Y. Guo, C. Duan, J. Opt. Soc. Am. B **18**, 5 (2001)
9. J.J. Olivero, R.L. Longbothum, J. Quant. Spectrosc. Radiat. Transf. **17**, 2 (1977)
10. http://cfa-www.harvard.edu/HITRAN/

V

Publication V

T. Hieta, M. Merimaa, M. Vainio, S. Seppä and A. Lassila, "High-precision diode-laser-based temperature measurement for air refractive index compensation", Appl. Opt. **50**, 5990-5998 (2011).

High-precision diode-laser-based temperature measurement for air refractive index compensation

Tuomas Hieta,[1,2] Mikko Merimaa,[1,*] Markku Vainio,[1,3] Jeremias Seppä,[1] and Antti Lassila[1]

[1]Centre for Metrology and Accreditation (MIKES), Tekniikantie 1, Espoo 02151, Finland

[2]Metrology Research Institute, Aalto University, Otakaari 5 A, Espoo 02150, Finland

[3]Laboratory of Physical Chemistry, Department of Chemistry, A. I. Virtasen aukio 1, University of Helsinki, Helsinki 00014, Finland

*Corresponding author: mikko.merimaa@mikes.fi

We present a laser-based system to measure the refractive index of air over a long path length. In optical distance measurements, it is essential to know the refractive index of air with high accuracy. Commonly, the refractive index of air is calculated from the properties of the ambient air using either Ciddor or Edlén equations, where the dominant uncertainty component is in most cases the air temperature. The method developed in this work utilizes direct absorption spectroscopy of oxygen to measure the average temperature of air and of water vapor to measure relative humidity. The method allows measurement of temperature and humidity over the same beam path as in optical distance measurement, providing spatially well-matching data. Indoor and outdoor measurements demonstrate the effectiveness of the method. In particular, we demonstrate an effective compensation of the refractive index of air in an interferometric length measurement at a time-variant and spatially nonhomogeneous temperature over a long time period. Further, we were able to demonstrate 7 mK RMS noise over a 67 m path length using a 120 s sample time. To our knowledge, this is the best temperature precision reported for a spectroscopic temperature measurement. © 2011 Optical Society of America

OCIS codes: 120.0120, 140.0140, 120.6780, 120.3180, 140.2020.

1. Introduction

The refractive index of a medium, usually air, must be known accurately in optical length measurements, because the length scale is derived from the speed of light. The most accurate method for determination of the refractive index n is an optical refractometer. Optical refractometers determine n by measuring the wavelength difference in vacuum and in ambient air [1,2]. However, refractometers measure the refractive index over a short fixed beam path and usually require a laboratory environment. Thus,

parameter-based Edlen and Ciddor equations are conventionally used and can reach an uncertainty in the 10^{-8} range [2–4]. Parameters affecting the refractive index of air include temperature, pressure, water vapor concentration, and CO_2 concentration. Sensitivity of the refractive index of air at 633 nm under standard ambient conditions is given in Table 1 for these parameters. Ambient pressure is generally homogeneous even over a long path length, and it is not usually the most dominant source of uncertainty [5]. Standard uncertainty of the order of 5 Pa is readily achievable. Also CO_2 concentration can be considered to be homogeneous and stable both in indoor and outdoor environments. Sensors capable of measuring the CO_2 concentration in the parts per million

Parameter Nominal Value	Temperature 20 C	Pressure 101.3 kPa	Relative Humidity 50%	CO_2 Concentration 400 ppm
Difference	−0.11 C	+0.037 kPa	−11.6%	+700 ppm

(ppm) range are commercially available, and can be used when large variations are expected or high accuracy is needed. Water vapor concentration at standard conditions has a relatively small effect on the refractive index of air, but, for example, at 35 °C, which is not uncommon outdoors or in an industrial environment, a measurement uncertainty of less than 5% is necessary to reach refractive index compensation below 10^{-7}.

In most cases, the uncertainty in the air temperature measurement dominates the combined uncertainty of refractive index determination. Under excellent laboratory conditions [6], air temperature can be measured to a high degree of accuracy using an ensemble of conventional temperature sensors. When performing optical distance measurements over tens of meters under industrial or outdoor conditions, air temperature measurement at a level required to reach, e.g., 10^{-7} uncertainty in distance is difficult or impossible, as the accuracy of temperature-sensor-based setups is deteriorated due to temporal and spatial air temperature variations. Thus, a method allowing fast measurement of air temperature over the path used in the optical distance measurement is desired. For a range of a few meters, an acoustic method based on the speed of sound measurement of an ultrasound burst signal can be used [7]. In this work, we have studied refractive index compensation using spectroscopy-based laser thermometry that allows temperature measurements over long path lengths.

Laser spectroscopy has been extensively used for noninvasive temperature sensing in gases [8–20]. Much of the research has been focused on combustion applications at elevated temperatures. Wavelength modulation absorption spectroscopy (WMAS) has recently received the most attention [10–15], but direct absorption spectroscopy measurements have also proven successful [16–19]. WMAS is generally preferred over direct absorption because only the peak values are required for thermometry.

We demonstrate that our system is capable of effectively compensating for the refractive index of air, even when temperature gradients are induced along the measurement path and conventional temperature sensors fail. The developed measurement system is capable of determining relative humidity and temperature over a long distance and along the interferometer beam path, resulting in an uncertainty smaller than 10^{-7} in the refractive index of air within a temperature range extending from 16 °C to 25 °C.

2. Experimental Setup

In a previous work [19] we presented a proof-of-principle on spectroscopic air temperature measurement with a RMS noise of 22 mK, which corresponds to an ∼$2 \cdot 10^{-8}$ RMS noise in the refractive index of air. Since then, the setup and data processing has been refined and an arrangement for relative humidity measurement was combined with our system for more complete refractive index of air compensation. The humidity measurement utilizes the same modulated and normalized absorption technique as the temperature measurement setup, but instead of measuring the ratio of two absorption peaks, only one water transition and baseline determination are required for determining the number density of water. A detailed description of the humidity measurement configuration and results is given in [21].

The combined measurement configuration is schematically shown in Fig. 1. Oxygen spectroscopy is done using two selected distributed feedback (DFB) lasers (Eagleyard EYP-DFB-0760) operating around 762 nm and having integrated temperature controls. Two selected DFB lasers (Sarnoff SAR-815-DFB) near 816 nm are used for water spectroscopy. Each laser has its own shutter and attenuator to optimize
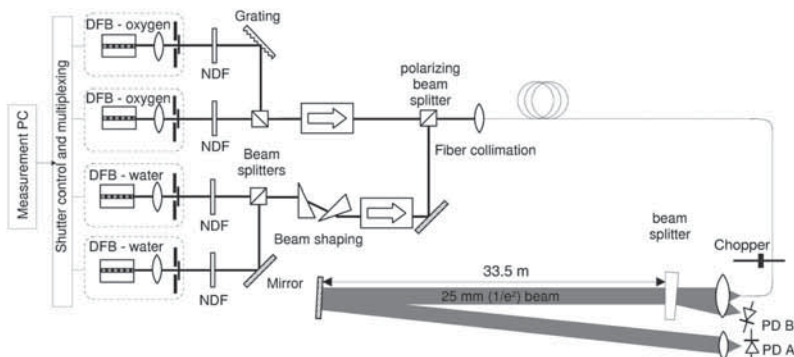

Fig. 1.   Schematic temperature measurement setup using a 67 m path length. Two water spectroscopy lasers are not in use.

the dynamic range of detection. During measurements, the spectral purity of one of the lasers used for oxygen spectroscopy was degraded, although the performance remained within the manufacturer's specification. It is known that diode laser output characteristics change over time, which unfortunately had a significant impact on our system's performance, as broadband emission outside the main mode causes errors in signal normalization. The grating was included in the setup to suppress spurious emission with good results. At the very end of our measurement period, which lasted around six months, the spectral purity of the other oxygen laser also had to be improved using a grating.

A polarizing beam splitter is used to combine light from the lasers for oxygen and water spectroscopy. Beam shaping with a prism pair is used for the SAR-815-DFB lasers to achieve improved fiber coupling efficiency. Low-loss single-mode fiber is used between the fiber coupling lens and measurement head. A high-quality aspheric lens (Asphericon 50-100 LPX-U) collimates the beam coming out from the fiber end. To reach a low sensitivity to polarization rotation in the fiber, a metallic beam splitter nearly perpendicular to the beam is placed close to the collimation lens to sample part of the output beam to photodiode B (PD B), while the other part of the beam is used for spectroscopy and detected with photodiode A (PD A). The normalization scheme used in the setup effectively cancels small drifts in the laser output power, interferences caused by the optics before the measurement head, varying fiber coupling efficiency, and rotation in the light polarization. A double-pass scheme using a dielectric mirror is used for practical reasons. It enables the use of the same measurement head for both transmitting and receiving. The double-pass scheme also compensates reasonably well the effect of absorption-induced power loss that leads to a weighted average. In comparison, in a simple single-pass scheme, the signal intensity can be much higher in the transmitting end than in the receiving end, leading to a weighted average that erroneously gives higher weight closer to the transmitting end. A mechanical chopper and a lock-in amplifier (SR-830) are used for detection of signals A and B at 1.6 kHz. An active control of the beam direction, based on piezoelectric transducers and a position sensitive detector, which is not shown in Fig. 1, close to PD A centers the reflected beam to the detector lens. Active control was found to be important both in outdoor and indoor environments. It compensates the thermal lensing effects caused by nonhomogeneous temperature distributions that otherwise lead to a random clipping of the beam edges. The measurement head electronics were connected to the measurement computer using an Ethernet for improved flexibility.

3. Theory and Line Selection

The widely used HITRAN [22–25] database was used to obtain molecular parameters for calculations and to simulate the transmission spectrum of air. Therefore, notations adopted from HITRAN are used to describe the molecular transmission properties presented in this section. The Beer–Lambert law is the fundamental equation that relates the light intensity I after a sample to the dimensionless optical thickness for a single transition $\tau_{\eta\eta'}$, according to

$$I = I_0 e^{-\tau_{\eta\eta'}}, \tag{1}$$

where I_0 is the intensity before the sample. For a single transition at frequency $\nu_{\eta\eta'}$ between lower and upper states η and η', the optical thickness for a gas at pressure p, temperature T, and at frequency ν, is calculated as

$$\tau_{\eta\eta'}(\nu, T, p) = u S_{\eta\eta'}(T) f(\nu, \nu_{\eta\eta'}, T, p) = u k_{\eta\eta'}(\nu, T, p), \tag{2}$$

where $S_{\eta\eta'}$ is the line intensity, f is the normalized line shape function, and u is the number density of absorbing molecules per unit path length. The monochromatic absorption coefficient $k_{\eta\eta'}$ is the product of a normalized line shape function and the line intensity. The line shape function, which is characterized by line half-width γ, is in general affected by both Doppler and pressure broadening. Doppler broadening is characterized by a Gaussian line profile and pressure broadening by a Lorentzian line profile. The actual line profile is obtained as a convolution of these two, which results into a Voigt line shape. In the lower atmosphere, the oxygen line shape function is dominated by the Lorentzian profile. We have used an approximate solution for the Voigt line shape [26] in the spectral simulations and a convoluted solution in all the calculations in this paper.

The temperature-dependent line intensity $S_{\eta\eta'}(T)$ can be calculated from the tabulated line intensity at reference temperature T_{ref} of 296 K using

$$S_{\eta\eta'}(T) = S_{\eta\eta'}(T_{ref}) \frac{Q(T_{ref})}{Q(T)} \exp\left[-\frac{hcE_\eta}{k}\left(\frac{1}{T} - \frac{1}{T_{ref}}\right)\right]$$
$$\times \left[\frac{1 - \exp(-hc\nu_{\eta\eta'}/kT)}{1 - \exp(-hc\nu_{\eta\eta'}/kT_{ref})}\right], \tag{3}$$

where $Q(T)$ is the total internal partition sum, E_η is the lower state energy, h is the Planck constant, k is the Boltzmann constant (not to be confused with the monochromatic absorption coefficient $k_{\eta\eta'}$), and c is the speed of light. The third term in Eq. (3) accounts for the ratio of Boltzmann populations between temperature T and the reference temperature T_{ref}. The last term accounts for the effects of stimulated emission, which is negligible at the visible wavelength region.

The temperature of air can be spectroscopically determined from the ratio of two oxygen transitions that have different lower state energies [8]. The ratio of the line intensities of the two transitions is given by

$$R = \frac{S_1(T)}{S_2(T)} = \frac{S_1(T_{\text{ref}})}{S_2(T_{\text{ref}})} \exp\left[-\frac{hc\Delta E}{k}\left(\frac{1}{T} - \frac{1}{T_{\text{ref}}}\right)\right]$$

$$= R_0 \exp\left[-\frac{hc\Delta E}{k}\left(\frac{1}{T} - \frac{1}{T_{\text{ref}}}\right)\right], \tag{4}$$

where ΔE is the difference in their rotational energies and R_0 is the ratio of S_1/S_2 at reference temperature. The oxygen transitions at $\lambda_1 = 761,715$ nm $\lambda_2 = 759,831$ nm were used in the measurements reported here and are marked with subindices 1 and 2, respectively. For absolute determination of the temperature, the line intensity ratio at the reference temperature must be known accurately. For example, a 10^{-3} error in the line intensity ratio will change the temperature by $\sim$120 mK when using transitions 1 and 2 at standard temperature and pressure. Based on Eq. (4), the rotational energy difference must be large in order to achieve high temperature sensitivity. Our approach is to use two weak transitions of the oxygen A-band R-branch near 762 nm for thermometry. The oxygen A-band [27–29] has several weak transitions that are well separated and virtually interference free from other molecular transitions, making it well suited for thermometry over long path lengths. In addition, oxygen concentration can be assumed to be very stable over time both in indoor and outdoor environments compared to, for example, water, which is often used in laser thermometry. The relevant parameters obtained from the HITRAN database [23–25] for the two chosen oxygen transitions are shown in Table 2. Hereafter, wavelength λ is used for describing the transition positions. The temperature measurement should be, in principle, independent of the path length according to Eq. (4). In practice, clipping of the beam edges due to poor alignment of the optical components or measuring over long distances will degrade the performance. In addition, the beam collimation is slightly dependent on the wavelength, thus making it impossible to collimate the two laser beams simultaneously over long distances. This will lead to a lead to independent clipping of the beams.

The simulated spectral transmission over a 67 m path length using the standard 20.95% oxygen concentration was calculated using the HITRAN database values and is given in Fig. 2. Figure 2 also shows the calculated relative change in the transmission for 1 K change in temperature. The center of the R-branch of the A-band transition becomes highly saturated at distances beyond tens of meters and,
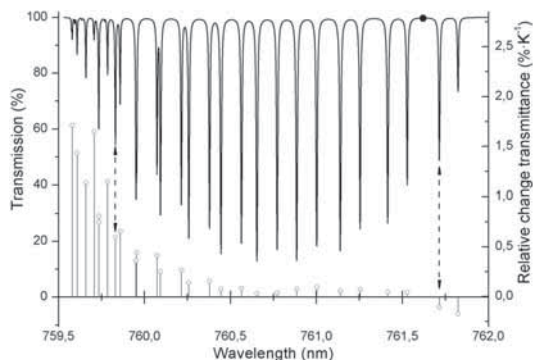

Fig. 2. Oxygen A-band transmission spectrum for a 67 m path in ambient air and the relative change in transmission for the strongest transitions [19]. The transitions used in this work are marked with dashed double arrows and the black dot marks the position of the baseline.

therefore, is not suitable for long-distance high-accuracy thermometry. The transitions used in this work are marked in Fig. 2 together with the point of the baseline measurement. In theory, the absolute temperature could be determined using only the ratio of the line intensities at reference temperature and the rotational energy difference. Although the baseline is not theoretically necessary for thermometry, it can have major impact on the results if omitted [19]. The small absorbance due to the tails of the Voigt profile is hence taken into account in the baseline measurements.

Oxygen concentration can be determined by sweeping the laser frequency over the whole absorption feature and fitting a Voigt profile to the measured absorption. The integrated line area can be calculated from the fit parameters to determine the concentration. Thermometry using the whole absorption feature is relatively straightforward, since broadening effects do not affect the normalized line shape function. Unfortunately, we were unable to achieve low uncertainty using fitting to the whole absorption profile in our very early tests. We aimed at real-time analysis and used a simple Lorentzian profile, which explains the problems we had in the fitting procedure. Therefore, we chose another method in which the peak absorption and baseline are measured. This method proved to be rapid and robust even in an outdoor environment. However, when measuring only the absorption peak, temperature and pressure affect the relative contributions of the Gaussian and Lorentzian components in the Voigt line shape, which changes the peak value of the line shape function. The effect of collisional, or Dicke, narrowing was investigated using a Galatry profile in the calculations [30,31]. The effect was found insignificant when compared to the result obtained using the convoluted Voigt profile.

The Doppler-broadened half-width, which is characterized by a Gaussian profile, depends on the wavelength, temperature, and mass of the molecule.

Table 2. Parameters for the Oxygen Transitions Used in This Work at Reference Pressure of 1 atm and Temperature of 296 K (n Denotes the Temperature Coefficient of the Temperature-Dependent Linewidth)

$\nu_{\eta\eta'}$ (cm^{-1})	λ (nm)	$S_{\eta\eta'}(T_{\text{ref}})$ (cm/molecule)	E_η (cm^{-1})	γ_{air} (cm^{-1})	n (1)
13128.27	761.715	3.583×10^{-24}	2.1	0.0563	0.71
13160.82	759.831	2.246×10^{-24}	544.5	0.0401	0.64

Increased temperature will increase the Doppler half-width and decrease the observed line width depending on the temperature coefficient n of the transition according to the empiric equation $\gamma_{\mathrm{air}}(T) = \gamma_{\mathrm{air}}(T_0) \times (T_0/T)^n$. This will result into a higher peak value of the absorption profile as the Gaussian line profile component becomes more dominant. Since the air broadened half-widths and the temperature coefficients are different for the two oxygen transitions, the temperature will have an effect on the line intensity ratio. For example, for a temperature change of $-10\,\mathrm{K}$ ($296\,\mathrm{K} \to 286\,\mathrm{K}$), the temperature determined from the ratio of the transmission minimums of transition 1 and transition 2 will be $76\,\mathrm{mK}$ higher if the temperature dependence of the line profile is taken into account, compared to the situation where this dependency is omitted. One should note that even small errors in, e.g., the temperature coefficient n can have a major impact on the final results. By using a temperature coefficient of 0.71 for both transitions, the same $-10\,\mathrm{K}$ temperature change would result in a $233\,\mathrm{mK}$ lower temperature. This correction is important especially when measuring very high temperature variations. It affects systems based on the WMAS technique as well.

Varying pressure affects the observed total linewidth in a similar manner as the varying temperature. An increase in the pressure increases the width of the Lorentzian component and decreases the relative contribution of the Gaussian component. As an example, if the pressure is decreased by $1\,\mathrm{kPa}$ ($101.3\,\mathrm{kPa} \to 100.3\,\mathrm{kPa}$), a $58\,\mathrm{mK}$ correction term must be added to the temperature determined by Eq. (4). In this work, a pressure correction factor α_{pres}, which is accurate for typical pressure variations in the ambient air, was used to correct the ratio R according to

$$R\left(1 + \alpha_{\mathrm{press}}\left(\frac{p - p_{\mathrm{ref}}}{p_{\mathrm{ref}}}\right)\right) = R_0 \exp\left[-\frac{hc\Delta E}{k}\left(\frac{1}{T} - \frac{1}{T_{\mathrm{ref}}}\right)\right],$$
(5)

where p_{ref} is the reference pressure ($101.3\,\mathrm{kPa}$). The temperature of the air can be directly calculated according to

$$T(R, p) = \frac{T_{\mathrm{ref}}}{1 - \frac{T_{\mathrm{ref}} k}{hc\Delta E}\ln\left(\frac{R}{R_0}\left(1 + \alpha_{\mathrm{press}}\left(\frac{p - p_{\mathrm{ref}}}{p_{\mathrm{ref}}}\right)\right)\right)}.$$
(6)

4. Obtaining the Parameters of the Model

The parameters for the model presented by Eq. (6), which are given in Table 3, had to be obtained from experimental data mainly for two reasons. First, the values in the HITRAN database are not accurate enough for high-resolution thermometry. The database values for the uncertainty of the line intensity and linewidth are between 1% and 2% for transitions 1 and 2, while the uncertainty in the line intensity

Table 3. Parameters Required for the Presented Spectroscopic Two-Line Thermometry

Data Source	ΔE (cm^{-1})	R_0 (1)	α_{pres} (1)
Database[a]	−542.4	1.1385	0.0500
Fit	−520.0	1.1571	0.0506

[a]HITRAN values are from the 2008 database.

ratio should be of the order of 10^{-4} in order to obtain the temperature with $\sim 12\,\mathrm{mK}$ uncertainty. Second, the wavelength-dependent losses in any of the optical components after the power normalization affect the results. A known source of a systematic error is the wavelength-dependent reflectivity of the dielectric mirror (Thorlabs BB2-E03) that was used as the end mirror in the measurement path. Because the wavelength dependency of the system was not explicitly characterized, the obtained parameters given in Table 3 are valid only for the presented temperature measurement configuration.

The measurement procedure is similar to that in our previous work [19]. A typical measurement of oxygen transmission is shown in Fig. 3. It was done outdoors over a $130\,\mathrm{m}$ path. One-hundred data points were collected for both features. Transition 2 is left out of Fig. 3 for clarity. In the measurements performed in the laboratory environment, the final baseline value is simply the average of all the measurement points. In the measurements done outdoors, we removed all data points that were at least 3 times the standard deviation off the average. We subsequently obtained the baseline by calculating the average of the corrected data. The erroneous data points were not common, which led to the conclusion that they were most likely caused by falling leaves and flying insects that occasionally blocked the laser beam during the measurements, which were done in October. A second-order polynomial fit to the measured transmission data is shown in Fig. 3. It was used in the outdoor measurements
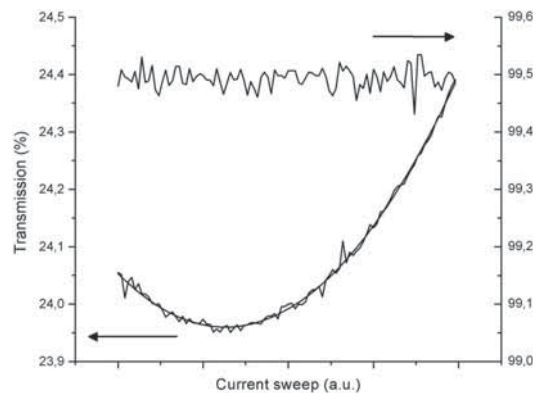

Fig. 3. Typical oxygen transmission measurement of transition 1 and baseline over a $130\,\mathrm{m}$ path measured outdoors including a second-order polynomial fit, which is used to determine the absorption peak.

due to the random erroneous data points. A simple 15-point moving average was used in the indoor measurements, in which case it was found to be the best method to determine the minimum transmission. The laser frequencies were loosely stabilized to the absorption line centers using data of the previous measurement and a relatively wide sweep area had to be used to ensure that the transmission minimum would be always found.

The small absorbance due to the tails of the Voigt profile causes the transmission to drop by approximately 0.5% at the point of the baseline measurement shown in Fig. 3. The intensity of an individual line is then calculated using Eq. (1) from the corrected baseline value and from the value of the minimum transmission. The same baseline is used to calculate the line intensity of both transitions. The air temperature is calculated using Eq. (6), which takes into account the pressure correction term. The temperature correction term, which is not explicitly shown in Eq. (6), is added to the temperature given by Eq. (6) to obtain the final temperature value.

The standard deviations of the baseline and the transition 1 measurement shown in Fig. 3 were 1.83×10^{-4} and 0.82×10^{-4}, respectively. The standard deviation of the sample mean is a factor of 10 lower for the baseline because the whole 100-point sample is used for averaging. In the temperature measurements done indoors, the standard deviation of the sample mean is approximately 4 times lower, because of the 15-point moving average. In the measurement shown in Fig. 3, we estimate that the standard deviation of the sample mean is approximately by a factor of 10 lower, because the fit to the second-order polynomial is good. These values for the standard deviations of the spectroscopic data indicate that the standard deviation of the temperature should be of the order of 3 mK according to Eq. (6) when using a value of 1.3×10^{-5} as the standard deviation of the sample mean for both transitions and for the baseline.

Experiments were done in a temperature- and humidity-controlled laboratory above a 30 m long interferometric measurement rail used for length metrology. Eight calibrated Pt-100 sensors were spaced evenly across the measurement path and their average was used as the reference temperature. Pt-100 sensors were positioned in close proximity of the beam path to ensure good lateral spatial overlap. The sensor closest to the measurement head was at slightly higher temperature than the others, due to heat generated by the electronics of the measurement head. The temperature controller of the laboratory room acts by adjusting the temperature of the incoming air. Temperature variations were induced by adjusting the set point of the controller. The result of a typical 62 h measurement is shown in Fig. 4. The period from 48 to 62 h was used to calculate the noise of the measurement. The RMS noise was 7 mK using a sample a time of 120 s. The black
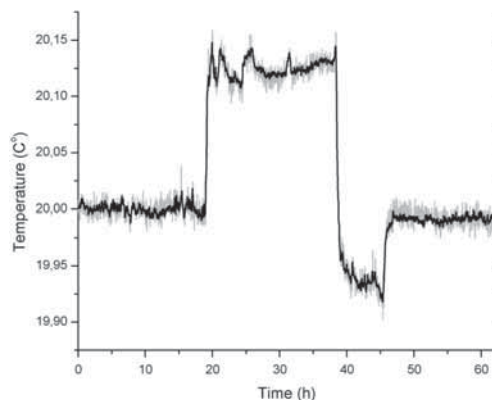

Fig. 4. Parameter calibration results of the spectroscopic thermometer measurement (gray) fitted to the ensemble of Pt-100 sensors (black) spaced evenly over the 67 m path length. The temperature variations were done by adjusting the temperature of the incoming air.

line represents the average of the reference sensors and the gray line shows the fit based on Eq. (6).

Since the temperature measurement is done in open laboratory space, the 7 mK RMS noise, which is larger than the 3 mK RMS estimate based on the transmission measurements, also includes the fluctuations in the air temperature and drifts in the mechanics and electronics. The RMS noise of the ensemble of Pt-100 sensors was 2.5 mK during the same measurement period. However, due to the relatively long time constant of the Pt-100 sensors, part of the rapid fluctuations in the air temperature are low-pass filtered, which likely explains the difference.

The temperature controller of the laboratory operates in a narrow set-point range and we were not able to induce large temperature variations. For such a narrow temperature range, the temperature effects described in Section 3 are insignificant. The pressure varied between 100 and 101.2 kPa during the measurement. The parameters obtained from the fit and the values calculated using the database are given in Table 3. The rotational energy difference and the ratio R_0 of the two absorption lines at the reference temperature and pressure are fairly close to values given in the HITRAN database. The pressure correction factor is in good agreement with the database value. If the database values for rotational energy difference and for the ratio at a reference temperature T_0 are used with the ratio R obtained from the fit, the spectroscopically determined temperature at standard pressure is 22.85 °C instead of the 21.05 °C obtained by using the fitted parameter values.

5. Measurements

To test the capability of the system to compensate the refractive index of air for an interferometric length measurement, we set up a heterodyne laser

interferometer (HP 5518) on top of the measurement rail. The path lengths of the interferometric system and the spectroscopic system were set to within a few centimeters of each other by fixing the corner cube of the interferometer to the measurement head of the spectroscopic measurement. Ideally, the beams should overlap to ensure the most effective compensation of the air refractive index, but for practical reasons the beams were not combined. The beams were at the same height and the separation of the beams was less than 10 cm over the whole measurement path. Two electric heaters and a fan, positioned close to the center of the measurement path and 2 m above the measurement rail, were used to induce rapid local air temperature variations. The heaters caused approximately 2.5 K local temperature rise, changing average temperature over the measurement path by 0.6 K. There was no significant increase in the temperature near the end mirror and the measurement head. The average temperature measured with the spectroscopic system (curve 4) and with the Pt-100 sensor ensemble (curve 3) are shown Fig. 5. A compensated interferometric reading is given in the upper part of Fig. 5 for both spectroscopic temperature measurement (curve 2) and the ensemble average of the Pt-100 sensors (curve 1). The temperature determined by the spectroscopic system was approximately 10 mK lower than the reference temperature between the heating periods. This could be caused by the realignment of the optics during the assembly of the interferometric system.

From the data it is clearly seen that the spectroscopic method compensates very well even local air temperature changes in interferometric displacement measurements. The heating periods are almost

invisible in the interferometer measurement, except for some transients. On the other hand, one can see that even with eight Pt-100 sensors, evenly spaced over a 30 m beam path, it is not possible to reach a good compensation if there are significant temperature gradients. During the measurements, the ambient pressure varied between 99.1 and 100.4 kPa. The 120 s sample time of the spectroscopic system explains transients in compensated displacement when the heating is turned on and off rapidly. The $\sim 5\,\mu m$ long-term drift in the measured displacement is probably caused by a real mechanical displacement of the concrete beams where the interferometer setup was mounted.

Outdoor measurements were conducted at the Nummela baseline of the Finnish Geodetic Institute. The measurement setup, except for the measurement head, was kept in a heated room with no active temperature control. The measurement head was positioned outdoors with no temperature control. The ambient temperature varied between 5 °C and 15 °C during a typical measurement day. The distance between the end mirror and the measurement head was 65 m, making the total measurement distance 130 m. Although the long path length causes decrease in sensitivity due to saturation in the transmission, we chose to use the same two transitions as shown in Fig. 2, because their properties were well characterized in the laboratory. Ten Pt-100 sensors were used as a reference with approximately equidistant spacing and close proximity to the laser beam. The spectroscopically measured temperature and the average of the Pt-100 sensors are shown in Fig. 6. The gray line represents the spectroscopic temperature, which is approximately 200 mK lower than the reference temperature given by the Pt-100 sensors for the last 6 h. Sun was shining for the first 2 h, which could explain the difference in the offset in
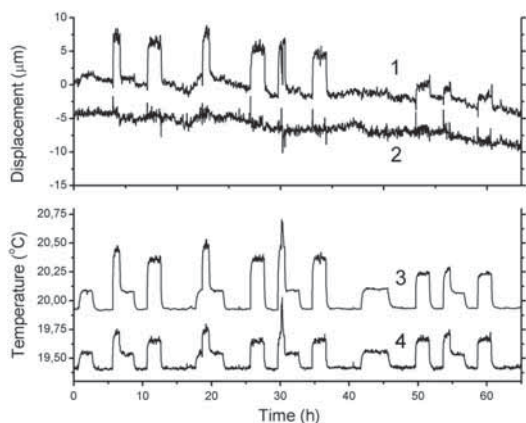

Fig. 5. Top, interferometric length compensated by using Pt-100 sensors (curve 1) and by using the spectroscopic temperature measurement (curve 2). Bottom, average temperatures along the path length with local temperature variations measured by the Pt-100 sensors (curve 3) and by the spectroscopic system (curve 4). For clarity, −5 μm and −500 mK offsets have been added to the spectroscopically compensated displacement (2) and to the spectroscopically determined temperature (4), respectively.
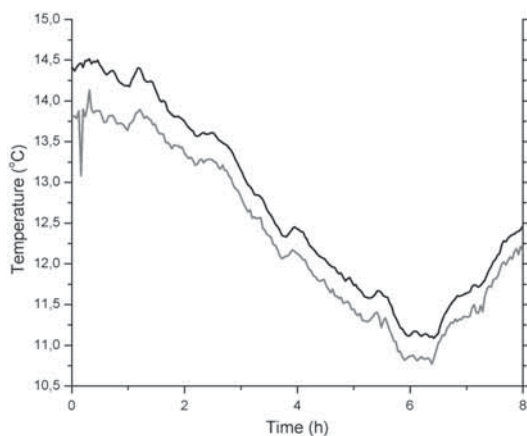

Fig. 6. Average temperature measured at Nummela baseline over a 130 m path length. Average of Pt-100 sensors is marked by black curve. Gray curve represents the spectroscopically measured temperature.

the beginning. The Pt-100 sensors were not protected from direct sunlight.

After the outdoor measurements, we transported the setup back to the laboratory and tested it in a temperature-controlled laboratory room to verify a broader temperature range. A good fit was found between the reference Pt-100 sensors and the spectroscopic method for a temperature range of 16 °C to 25 °C. The parameters of the previous fit could not be used, as we had to use several wavelength-dependent mirrors in order to achieve a path length of 40 m in a small laboratory room. Although we used only a limited temperature range to fit the parameters of Eq. (6), the model was found to be accurate also over a broader temperature range. Therefore, we expect that the temperature offset observed in the outdoor measurements is predominantly affected by the transportation of the setup compared to the uncertainty in the transition parameters discussed in Section 2. For example, the beam splitter had slightly moved during the transportation, which was observed only later. The 200 mK offset corresponds to approximately 1.7×10^{-3} difference in the line intensity ratio. Part of the difference could be also explained by nonideal collimation of the laser beams, which we could not verify in the outdoor environment.

6. Discussion and Conclusions

A spectroscopic method for on-line compensation of air refractive index over longer distances has been described and demonstrated experimentally. The method is capable of measuring average air temperature along approximately the same beam path that is used for optical length measurement. The method provides potentially excellent spatial and temporal overlap and, therefore, accurate air temperature compensation. A drawback of the present setup is the modest time resolution, approximately 120 s. The main reason for the limited time resolution is that just one laser is used to probe the absorption peak and the baseline, which means that the laser wavelength has to be repeatedly tuned between the two wavelengths. The wavelength tuning is done by laser temperature, causing 30 s dead time after each adjustment using our equipment. Another disadvantage of the present setup is the lack of active wavelength stabilization. For this reason, the wavelength scan over an absorption line has to be rather wide to ensure that the peak absorption is captured during each scan. Therefore, the total number of measured points is much larger than what is actually needed for the final analysis. The measurement speed could be significantly improved if a method to stabilize the laser frequency to the absorption peak would be developed. This could be achieved, for example, by using a third-harmonic locking scheme and an external low-pressure oxygen cell or a hollow fiber filled with oxygen. One possibility would be to use the second-harmonic signal at the locked wavelength of the absorption maximum to determine the temperature [11–14]. In this way, there would not be any wasted data points and the time resolution would be determined by the shutter switching time and the lock-in amplifier settling time. We estimate that a time resolution of a few seconds could be possible to achieve without increasing the measurement noise considerably.

We have demonstrated, to our knowledge, the most precise spectroscopic temperature measurement of air. Our system allows measurements over long distances of up to 130 m with a RMS noise of 7 mK for a 120 s averaging time, which corresponds to $\sim 0.7 \times 10^{-8}$ RMS noise in the refractive index of air. The obtained noise level is considerably lower than the 22 mK RMS noise using the 60 s averaging time presented in our previous work [19].

The accuracy of the temperature measurement system is difficult to evaluate. Re-evaluation of the data presented in our earlier study [19] showed a 20 mK offset when changes were made to the system during the measurement. Considering the 10 mK offset that was observed in our current temperature measurement system during the interferometric tests, we believe that, with the current system and calibration, we are able to determine the air temperature with accuracy high enough to safely reach an uncertainty smaller than 10^{-7} in the refractive index of air from a 16 °C to 25 °C temperature range in a laboratory environment.

Compensation of the refractive index of air required for high-accuracy length measurements has been shown to be feasible even when significant local temperature variations are induced. The effect of the line profile composition and the sensitivity of the method to transition parameters have been discussed. Outdoor measurement results are in agreement with the laboratory experiments except for an offset, which can be explained by major alignment changes caused by the transportation and possibly nonideal collimation of the laser beams.

References

1. K. P. Birch and M. J. Downs, "The results of a comparison between calculated and measured values of the refractive index of air," J. Phys. E **21**, 694–695 (1988).
2. G. Bonsch and E. Potulski, "Measurement of the refractive index of air and comparison with modified Edlén's formulae," Metrologia **35**, 133–139 (1998).
3. B. Edlen, "The refractive index of air," Metrologia **2**, 71–80 (1966).
4. P. E. Ciddor, "Refractive index of air: new equations for the visible and near infrared," Appl. Opt. **35**, 1566–1573 (1996).
5. A. Lassila, "Updated performance and uncertainty budget of MIKES' line scale interferometer," in *Proceedings of 4th*

EUSPEN International Conference (EUSPEN, 2004). pp. 258–259.

6. A. Lassila, M. Kari, H. Koivula, U. Koivula, J. Kortstrom, E. Leinonen, J. Manninen, J. Manssila, T. Mansten, T. Merilainen, J. Muttilainen, J. Nissila, R. Nyblom, K. Riski, J. Sarilo, and H. Isotalo, "Design and performance of an advanced metrology building for MIKES," Measurement **44**, 399–425 (2011).

7. V. Korpelainen and A. Lassila, "Acoustic method for determination of the effective temperature and refractive index of air in accurate length interferometry," Opt. Eng. **43**, 2400–2409 (2004).

8. A. Y. Chang, M. D. DiRosa, D. F. Davidson, and R. K. Hanson, "Rapid tuning cw laser technique for measurements of gas velocity, temperature, pressure, density, and mass flux using NO," Appl. Opt. **30**, 3011–3022 (1991).

9. M. P. Arroyo and R. K. Hanson, "Absorption measurements of water-vapor concentration, temperature, and line-shape parameters using a tunable InGaAsP diode laser," Appl. Opt. **32**, 6104–6116 (1993).

10. D. S. Baer, R. K. Hanson, M. E. Newfield, and N. K. J. M. Gopaul, "Multiplexed diode-laser sensor system for simultaneous H_2O, O_2, and temperature measurements," Opt. Lett. **19**, 1900–1902 (1994).

11. J. Silver and D. J. Kane, "Diode laser measurements of concentration and temperature in microgravity combustion," Meas. Sci. Technol. **10**, 845–852 (1999).

12. J. T. C. Liu, J. B. Jeffries, and R. K. Hanson, "Large-modulation-depth $2f$ spectroscopy with diode lasers for rapid temperature and species measurements in gases with blended and broadened spectra," Appl. Opt. **43**, 6500–6509 (2004).

13. X. Zhou, J. B. Jeffries, and R. K. Hanson, "Development of a fast temperature sensor for combustion gases using a single tunable diode laser," Appl. Phys. B **81**, 711–722 (2005).

14. J. Shao, L. Lathdavong, P. Kluczynski, S. Lundqvist, and O. Axner, "Methodology for temperature measurements in water vapor using wavelength-modulation tunable diode laser absorption spectrometry in the telecom C-band," Appl. Phys. B **97**, 727–748 (2009).

15. M. G. Allen, "Diode laser absorption sensors for gas-dynamic and combustion flows," Meas. Sci. Technol. **9**, 545–562 (1998).

16. V. Ebert, T. Fernholz, C. Giesemann, H. Pitz, H. Teichert, J. Wolfrum, and H. Jaritz, "Simultaneous diode-laser-based *in situ* detection of multiple species and temperature in a gas-fired power plant," Proc. Combust. Inst. **28**, 423–430 (2000).

17. S. T. Sanders, J. Wang, J. B. Jeffries, and R. K. Hanson, "Diode-laser absorption sensor for line-of-sight gas temperature distributions," Appl. Opt. **40**, 4404–4415 (2001).

18. H. Teichert, T. Fernholz, and V. Ebert, "Simultaneous *in situ* measurement of CO, H_2O, and gas temperatures in a full-sized coal-fired power plant by near-infrared diode lasers," Appl. Opt. **42**, 2043–2051 (2003).

19. T. Hieta and M. Merimaa, "Spectroscopic measurement of air temperature," Int. J. Thermophys. **31**, 1710–1718 (2010).

20. V. Spagnolo, L. Dong, A. A. Kosterev, D. Thomazy, J. H. Doty III, and F. K. Tittel, "Modulation cancellation method for measurements of small temperature differences in a gas," Opt. Lett. **36**, 460–462 (2011).

21. F. Pollinger, T. Hieta, M. Vainio, N. R. Doloca, A. Abou-Zeid, K. Meiners-Hagen, and M. Merimaa, "Effective humidity in length measurements: comparison of three approaches," Meas. Sci. Technol. (to be published).

22. Further information on HITRAN available from www .hitran.com.

23. D. J. Robichaud, J. T. Hodges, P. Maslowski, L. Y. Yeung, M. Okumura, C. E. Miller, and L. R. Brown, "High-accuracy transition frequencies for the O_2 *A*-band," J. Mol. Spectrosc. **251**, 27–37 (2008).

24. D. J. Robichaud, J. T. Hodges, L. R. Brown, D. Lisak, P. Maslowski, L. Y. Yeung, M. Okumura, and C. E. Miller, "Experimental intensity and lineshape parameters of the oxygen *A*-band using frequency-stabilized cavity ring-down spectroscopy," J. Mol. Spectrosc. **248**, 1–13 (2008).

25. L. R. Brown and C. Plymate, "Experimental line parameters of the oxygen *A* band at 760 nm," J. Mol. Spectrosc. **199**, 166–179 (2000).

26. Y. Liu, J. Lin, G. Huang, Y. Guo, and C. Duan, "Simple empirical analytical approximation to the Voigt profile," J. Opt. Soc. Am. B **18**, 666–672 (2001).

27. Q. V. Nguyen, R. W. Dibble, and T. Day, "High-resolution oxygen absorption spectrum obtained with an external-cavity continuously tunable diode laser," Opt. Lett. **19**, 2134–2136 (1994).

28. V. G. Avetisov and P. Kauranen, "High-resolution absorption measurements by use of two-tone frequency-modulation spectroscopy with diode lasers," Appl. Opt. **36**, 4043–4054 (1997).

29. P. Vogel and V. Ebert, "Near shot noise detection of oxygen in the A-band with vertical-cavity surface-emitting lasers," Appl. Phys. B **72**, 127–135 (2001).

30. L. Galatry, "Simultaneous effect of Doppler and foreign gas broadening on spectral lines," Phys. Rev. **122**, 1218–1223 (1961).

31. P. L. Varghese and R. K. Hanson, "Collisional narrowing effects on spectral line shapes measured at high resolution," Appl. Opt. **23**, 2376–2385 (1984).

VI

Publication VI

F. Pollinger, T. Hieta, M. Vainio, N.R. Doloca, A. Abou-Zeid, K. Meiners-Hagen and M. Merimaa, "Effective humidity in length measurements: comparison of three approaches," MIKES Report J1/2011.

Effective humidity in length measurements: comparison of three approaches

Florian Pollinger[1], Tuomas Hieta[2,3], Markku Vainio[2,4], Nicolae R Doloca[1], Ahmed Abou-Zeid[1], Karl Meiners-Hagen[1], and Mikko Merimaa[2]

[1]Physikalisch-Technische Bundesanstalt, Bundesallee 100, 38116 Braunschweig, Germany

[2]Centre for Metrology and Accreditation (MIKES), Tekniikantie 1, Espoo 02151, Finland

[3]Metrology Research Institute, Aalto University, Otakaari 5 A, Espoo 02150, Finland

[4]Laboratory of Physical Chemistry, Department of Chemistry, A. I. Virtasen aukio 1, University of Helsinki, Helsinki 00014, Finland

Email: Florian.Pollinger@ptb.de

Abstract. Humidity is one of the key atmospheric parameters influencing the refractive index of air. Consequently, humidity influences all length measurements whose scale is derived from the speed of light. In this work we present two laser spectrometers developed for determining the average humidity of air over a long measurement path where local variations may be difficult to measure using conventional sensors. Further, these laser-based systems allow, in principle, good spatial overlap with the beams used in dimensional measurements. The developed systems were compared to each other and to traceable reference sensors during a 65 hour measurement campaign. The performance of the systems was investigated under three different conditions: steady-state, humidity transient, and temperature transient. Both systems were also successfully applied in outdoor environment at distances up to several hundreds of meters. Compared to a capacitive sensor network, significant deviations can be observed under these conditions.

1. Introduction

Laser-based absolute length measurements over distances of several meters up to several hundred meters have been considerably improved in the last decade. Developments were basically driven by the availability of new laser sources [1] and measurement approaches, e.g. femtosecond-based techniques making possible relatively simple measurement schemes with relative uncertainties below 10^{-6} [2 - 6]. Sophisticated schemes to exploit diode laser sources or Nd:YAG lasers for multi-wavelength interferometric distance metres have demonstrated similarly impressive performances under laboratory conditions [7 - 12]. These developments are not only of purely academic interest: Uncertainties below 10^{-6} are required in positioning in space [4], for applications in geodesy, e.g. in the dimensional characterisation of nuclear waste repositories [13], or, increasingly, in the dimensional surveillance and characterisation of large work pieces in the production process [14]. If not applied in vacuum or in well-controlled metrological laboratories, the uncertainty of the measurement is actually not limited by the interferometric measurement, but by the insufficient knowledge of the refractive index n of the medium - the scale of the interferometric measurement being the wavelength of the laser light in the medium.

The refractive index of air is conventionally determined using empirical equations [15 - 17] with temperature, humidity, pressure, and CO_2 concentration as parameters. As the ambient pressure is relatively homogenous even over a long path length, variations are mainly due to the known height profile. Hence, the imperfect knowledge of the air pressure is usually not the most dominant source of uncertainty. The CO_2 concentration has a very small influence. Indisputably, the uncertainty of the temperature has the largest influence on the length measurement, with approximately 1 K corresponding to a relative change in air refractivity of 1×10^{-6}. Local temperature variations induced, e.g., by localized heat sources in indoor environment or by variable land surfaces in outdoor environments can easily induce significant temperature gradients. Consequently, sophisticated schemes have been developed to measure the effective temperature along the beam path. Realized methods are based, e.g., on acoustic density measurements [18], or spectroscopic temperature measurements [19 - 24]. Nevertheless, to achieve overall relative uncertainties of the absolute length measurements in the order of 1×10^{-7}, also the humidity must be taken into account. When using the Edlén equation, however, an uncertainty of 1 % RH corresponds to a relative uncertainty of 10^{-8} L for standard conditions. Hence, if the temperature can be determined with an accuracy of 0.1 K then the humidity measurement is relatively uncritical.

But in practice, due to local variations, a temperature measurement with accuracy better than 0.1 K is almost impossible to realise outdoors. There is, however, a way to circumvent an explicit temperature measurement to compensate the influence of the index of refraction [25, 26] by using the dispersion of two different wavelengths, e.g. at 532 and 1064 nm. The simple compensation scheme neglects however the influence of humidity completely. Using this method in humid environment, the sensitivity of the length measurement to uncertainties of the environmental parameters changes significantly. The dependency to uncertainties in temperature and pressure decreases by at least one order of magnitude [27]. In contrast, the dependency on the relative humidity increases in this method: an uncertainty of 1 % in relative humidity translates into a relative measurement uncertainty of 2.4×10^{-8} L [27]. A targeted relative measurement uncertainty of 1×10^{-7} [13] would therefore require an accuracy of the humidity measurement of better than 4 % in relative humidity in this case. In fact, in an improved version of this method as discussed in reference [27], the length can be derived by the two length measurements and an independent measurement of the partial pressure of water only, without additional information on temperature and pressure. In this case, an uncertainty of 1 hPa in the partial pressure of water corresponds to 10^{-7} in length, which is equivalent to an uncertainty of 4 % RH at standard conditions.

Standard capacitive humidity sensors are localized point sensors and are thus in principle incapable to monitor the effective humidity over longer distances. For applications in the measurement of longer distances several sensors must be used in a dense network. Alternatively, the probe must be delocalised in order to be sensitive to the effective humidity along the beam path which is actually interacting with the interferometric probe. Hence, it is straightforward to apply optical spectroscopic techniques that are compatible with interferometric techniques to determine the water contents of the air. Optical absorption spectroscopy based on tuneable diode lasers (frequently referred to as tuneable diode laser absorption spectroscopy TDLAS) is a widely used tool to measure qualitatively and quantitatively gaseous species in physical chemistry [28]. Due to the commercial relevance and its importance for the understanding of the composition of the atmosphere there have been a significant number of sophisticated experimental realisations of the measurement of the spectroscopic water contents [29 - 34]. Nevertheless, such experiments are designed for well characterised measurement volumes like Herriot cells, i.e. in well-controlled geometries. But an application for long distance measurements requires a flexible sensor design. In this study, two different approaches of optical absorption spectrometers were developed by the national metrological institutes of Finland (MIKES)

and Germany (PTB). Both of these humidity sensors, designed for long-range distance measurements, can be easily integrated in sophisticated length measurement systems.

2. Theory

First the theory of quantitative molecular absorption spectroscopy relevant for the understanding of the measurement principles is briefly reviewed, following the standard notation as defined by the HITRAN database [35].

The optical absorption in a medium can be described by the Beer-Lambert law that relates the transmitted intensity I to the dimensionless optical depth τ, according to

$$I = I_0 e^{-\tau(l)}, \quad (1)$$

I_0 representing the initial intensity.

For a single transition at frequency $\nu_{\eta\eta'}$ between lower and upper states η and η', the optical depth for a gas at pressure p, temperature T, and at frequency ν, is calculated as

$$\tau_{\eta\eta'}(\nu, T, p) = u\, S_{\eta\eta'}(T)\, f(\nu, \nu_{\eta\eta'}, T, p)\, l \qquad (2)$$

in which u is the number density of absorbing molecules, $S_{\eta\eta'}$ the line strength, f the normalized line shape function, and l the absorption path length. The observed halfwidth γ of a transition is broadened by a number of mechanisms. The predominant mechanisms are intermolecular collisions with other water molecules (self-broadening γ_{self}) or other species (air-broadening γ_{air}). For a given temperature T and ambient pressure p, the halfwidth can be described as in [35]

$$\gamma(p, T) = \left(\frac{T_{ref}}{T}\right)^n \left(\gamma_{air}\left(p_{ref}, T_{ref}\right)(p - e) + \gamma_{self}\left(p_{ref}, T_{ref}\right)e\right) \qquad (3)$$

in which n is an empiric coefficient, e the partial pressure of water, p_{ref} the reference pressure of 1013 hPa, and T_{ref} the HITRAN reference temperature of 296 K. A typical value for the empiric coefficient n for water near the used transitions is between 0.6 and 0.7. In the case of water transitions considered in this study the self-broadening width, γ_{self}, is approximately five times larger than the air-broadening width, γ_{air}.

Table 1. Numerical values of the parameters necessary for the quantitative analysis as deduced from the HITRAN 2008 database [36]. The MIKES analysis presented in this paper is based on the analysis of the transition at 12249.38 cm^{-1}. The PTB system uses several transitions of different absorption strengths $S_{\eta\eta'}$ to measure the partial water pressure depending on optical path length and water contents.

$\nu_{\eta\eta'}$ (cm^{-1})	λ (nm)	$S_{\eta\eta'}(T_{ref})$ (cm/molecule)	γ_{air} cm^{-1}	γ_{self} cm^{-1}
12108.32	825.879	2.410x10^{-23}	0.1049	0.4643
12108.36	825.876	3.110x10^{-24}	0.0948	0.4291
12113.88	825.499	6.413x10^{-24}	0.1027	0.4661
12184.64	820.705	1.672x10^{-24}	0.0900	0.4837
12249.38	816.368	2.674x10^{-23}	0.0770	0.4291

The relevant parameters obtained from the 2008 HITRAN database [36] for certain water transitions are shown in table 1. The partial pressure of water vapour can be calculated from the number density u using the ideal gas law. Several empiric equations for the saturation pressure of water e_{sat} can be deployed to derive the relative humidity RH – occurring in the practically relevant compensation formulae - from the partial pressure and temperature [37, 38], e.g. using Wexler's equation as modified by Hardy [38]

$$RH = \frac{e}{e_{sat}} = \frac{uk_B T}{\sum_{i=0}^{6} g_i T^{i-2} + g_7 \ln(T/K)} \qquad (4)$$

with k_B representing Boltzmann's constant, T the temperature in Kelvin (K) and g_1 to g_7 empiric coefficients.

3. Experimental methods

Based on equations (1) to (3), there are different possibilities for a quantitative analysis of spectroscopic absorption data. Two different approaches are considered as shown in the following.
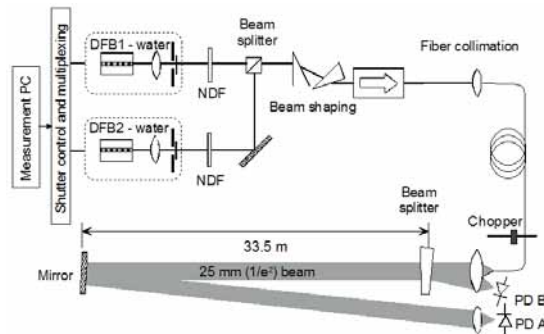
3.1 Peak height analysis

Figure 1. Schematic humidity measurement set-up used by MIKES in the comparison.

The measurement principle deployed by MIKES is based on a direct exploitation of equations (1) to (3). During the measurement, the amplitude of the absorption peak is monitored. This quantity is sufficient to deduce the number density u from if the temperature T, pressure p, and the absorption path l are measured independently. Due to inevitable drifts of the laser frequency, the wavelength must be loosely stabilized. The MIKES measurement configuration is shown in figure 1. Two DFB lasers (Sarnoff SAR-815-DFB) near 816 nm are used to probe the baseline and the transition. Each laser has its own shutter and attenuator (neutral density filter, NDF) to optimize the dynamic range of the detection. Beam shaping using a prism pair was used to achieve an effective fibre coupling. A low loss single-mode fibre is used between the fibre coupling lens and the measurement head. An aspheric lens (Asphericon 50-100 LPX-U) collimates the beam coming out from the fibre end and a metallic beam splitter is placed close to the collimation lens to provide the feedback measured by photodiode B (PD B). A double pass scheme using a dielectric mirror is used for practical reasons enabling the use of the measurement head for both transmitting and receiving beam while simultaneously cancelling out weighing effects on the average due to the exponentially decaying intensity. A mechanical chopper and a lock-in amplifier (SR-830) are used for detection. The active beam position control, consisting of piezoelectric transducers and a position sensitive detector close to PD A, is omitted in figure 1. The measurement head electronics were connected to a computer via Ethernet for more flexibility. One laser is used to probe the transmission minimum and the other measures the baseline.

In principle, the humidity can be determined by the ratio of the measured peak absorption and the baseline transmission. This ratio is however influenced by several additional effects which must be accounted for. For once, increased water vapour pressure increases the observed line width according to Eq. (3) and reduces the peak value of the absorbance. In addition, the increased water vapour pressure alters the relative contributions of the Gaussian and Lorentzian components in the Voigt line shape. In particular, an increased water vapour pressure reduces the effective Gaussian component in the Voigt profile, resulting in a lower peak value of the normalized line shape function f. A linear approximation using only Eq. (3) would induce a significant error on the results. The temperature dependence of the linewidth characterized by the empirical coefficient n influences both, the observed linewidth of the transition, and the composition of the Voigt profile. The effect on the Voigt profile composition can be omitted: it is inherently small compared to the measurement uncertainty and to the sensitivity requirements for the refractivity compensation presented in the first section. Although the analysis is done using an approximate Voigt solution, the overall error compared to the convoluted solution remains small [39]. The measurement principle was also deployed to determine the spectroscopic temperature [23, 24]. In reference [24], further details on the experimental realisation and on the necessary data processing can be found.

Figure 2 shows simulated transmission spectra of ambient air having 50 % relative humidity at 20°C. The used transition and the position of the baseline measurement for the MIKES hygrometer are shown in the upper part of the figure 2 and the relevant parameters for the transition are given in table 1. The lower state energy E_η and the coefficient n for the used transition were 325.3 cm^{-1} and 0.64, respectively. These two parameters are required to calculate the temperature dependent line intensity [35], which has to be taken into account for the analysis. The water transitions around 816 nm are virtually free from interfering molecular transitions and several transitions suitable for long range measurement as well as areas for baseline measurement can be found. Residual absorbance due to Voigt profile tails are taken into account in the baseline measurements.
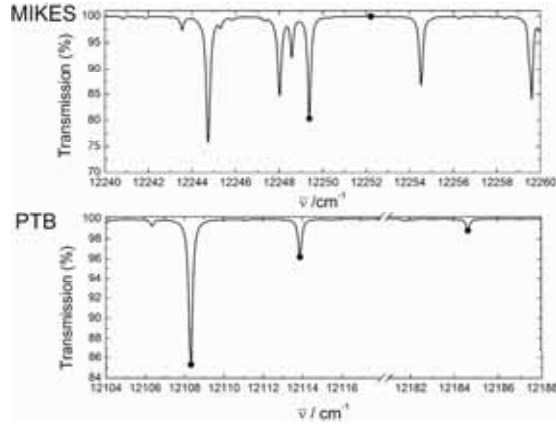
Figure 2. Simulated water transmission spectra for a 67 m absorption path at 50% relative humidity. The MIKES system uses the marked transition's peak intensity with the level of the baseline determined at the second marker. The PTB system uses different transitions for different lengths which are marked in the lower spectrogram. Its analysis is based on the determination of the complete peak area of the marked peaks.

3.2 Integral absorption analysis

The second approach to measure the relative humidity in air followed by PTB is based on a modification of equation (2). To our knowledge it was first proposed by Allen, Sonnenfroh and co-workers [40]. In order to directly exploit equation (2) for a quantitative measurement, the observation of rare well-isolated lines is necessary and assumptions on the functional dependence of the line shape f must be made. Being only interested in the number density u some of these obstacles can be circumvented using the integral form of equation (2)

$$\tau(l) = \int_{\overline{v}_1}^{\overline{v}_2} \sum_j u l S_j(T) f_j(\overline{v}_{0j}, \overline{v}_{\eta\eta'}, T, p) d\overline{v} \, , \qquad (5)$$

$S_j(T)$ representing all transitions in the integration interval $[\overline{v}_1, \overline{v}_2]$. If $\overline{v}_1$ and $\overline{v}_2$ are chosen far enough from all relevant peak centres $\overline{v}_{0j}$, the normalisation of the line shape function makes it possible to approximate the last term of equation (5) by $\int_{\overline{v}_1}^{\overline{v}_2} f_j(\overline{v}_{0j}, \overline{v}_{\eta\eta'}, T, p) d\overline{v} \approx 1$ resulting in

$$\tau(L) = \int_{\overline{v}_1}^{\overline{v}_2} \ln\left(\frac{I_0}{I}\right) d\overline{v} = u l \sum_j S_j(T) \Big|_{\overline{v}_1}^{\overline{v}_2}. \qquad (6)$$

Equation (6) provides a direct recipe for a measurement of the humidity of air from a spectroscopic measurement. In figure 3 the technical realisation is depicted. The spectrometer is divided into two functional units: The spectroscopic head (3a) and the beam preparation unit (3b) which are connected by an optical fibre. A widely tuneable external cavity diode laser (ECDL, Toptica DLpro) is used as optical source making the complete absorption band between 800 and 850 nm accessible. In this band suitable absorption lines can be found for the complete range between 50 and 1000 m. The lines deployed in this study are depicted in figure 2 and table 1. For the correct line identification a commercial optical spectrum analyzer (OSA, Advantest Q8347) was integrated into the beam preparation unit. The relative calibration of the frequency axis during frequency sweeps was performed using a temperature-stabilised Fabry-Perot interferometer (Toptica FPI 100) with a free spectral range (FSR) of 1.0 GHz. For the absolute calibration of the line centre the transition positions
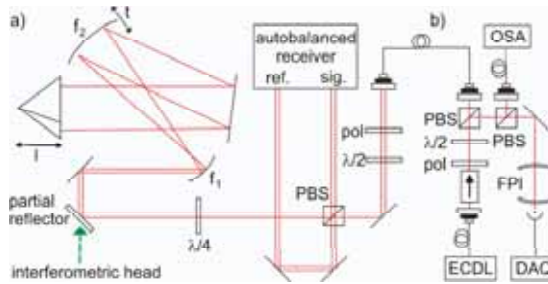
Figure 3. Optical set-up of the PTB integrative absorbance spectrometer. The spectrometer is divided into spectroscopic head (a) and beam preparation unit (b).

given in the HITRAN data base were used [36]. On the spectroscopic head, reference and probe beam are separated. The spectroscopic probe beam can be combined with a length measuring probe beam by a partial reflector. For the targeted long distances, the probe beam is expanded by a reflective telescope and reflected back using a corner cube mirror as target. The spectra are normalised using an auto-balanced detector (New Focus 2007). The signals of the spectroscopic beams and the transmittance of the FPI together with the modulation voltage of the ECDL are sampled by a 16-bit, 8-channel data acquisition card (National Instruments) with 250 000 samples/s. The ECDL was modulated with 27.6 Hz corresponding to a sampling per sweep edge of approximately 4500 points, or 0.014 GHz/sample point. During the comparison ten modulation cycles were sampled every 30 seconds. Due to the increased instability outdoors, 60 sweeps were taken every 20 seconds there. The frequency axis of each sweep was calibrated using the 1.0 GHz frequency markers of the etalon signal. In between, the frequency was linearly interpolated. To measure the humidity within the optical absorption path of 136.43 m in the comparison, the duplet transition at 12108.3 cm^{-1} was investigated because its absorption strength ensures an optimum sensitivity for this range.

A sufficiently wide mode-hop free spectral range (MHFSR) of the laser source is required for analysis of the integrated peak area using equation (6). In addition, the measured spectral feature should be well separated from other absorption features to accurately sample the baseline level. For the envelope of the duplet transition at 12108.3 cm^{-1}, a full width half maximum (FWHM) of approximately 0.22 cm^{-1} was observed in the experimental configuration used. While typically a MHFSR of 1.4 cm^{-1} could be maintained during the experiment, periods of only 1.0 cm^{-1} MHFSR could not be avoided during the 50 hours of comparison. As a consequence, the background level could not be determined consistently for the complete data set on both sides of the transition. Therefore, the analysis was modified: Not the complete spectral feature, as indicated by equation (6), but only the lower energy half of the spectral feature, marked dashed in figure 4a, was analyzed. This spectral region could be observed without mode-hops during the complete experiment. In this case, however, it is not longer possible to simply add the line strengths within the spectral region according to equation (6). The spectral weight of the underlying peaks must be unfolded. According to the HITRAN database, the observed spectral feature at 12108.3 cm^{-1} consists mainly of two transitions. A straightforward decomposition of the observed absorption data based on a peak fitting approach is not stable as the structure on the envelope is relatively weak. As can be seen in figure 4b, there is a large overlap between the transitions. Moreover, the relatively large line strength ratio 7.7 to 1 further reduces the impact of the minor feature on the envelope. Instead, the observed feature was integrated numerically up to the convoluted peak maximum by trapezoid integration. The measured intensity was then interpreted based on a numerical simulation of the single peak transmissions. The HITRAN database was used to fix the line strength ratio of the duplet and the most intense neighbouring five transitions.
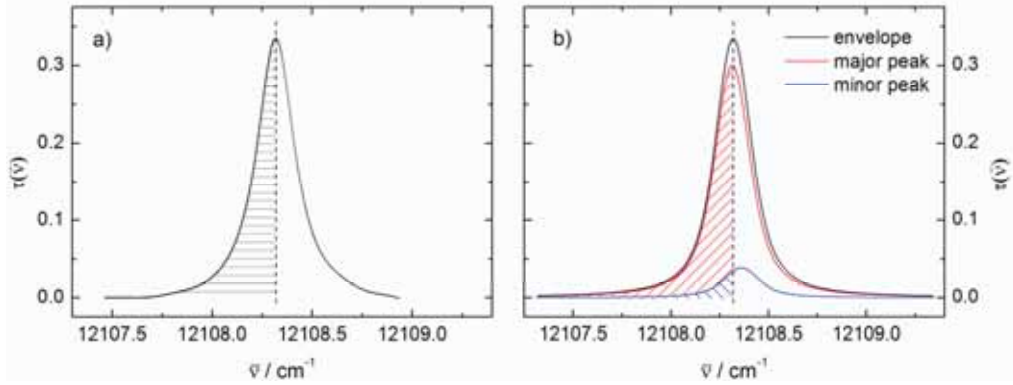
Figure 4. Half integration analysis. The absorption feature at 12108.3 cm^{-1} was used for the integral spectroscopic measurement performed by PTB. Due to limited MHFSR of the source only the shaded peak area was used for the analysis (a). In (b) a simulation of the transmission based on adjusted HITRAN parameters is depicted. The two most intense transitions contributing to the observed spectral feature are depicted in red and blue.

The peak shape, i.e. the height and the width, was adjusted to reproduce the experimentally observed envelope (confirm figures 4a and b). According to these simulations, 91.4 % of the observed absorbance in the spectral region of interest between 12107.57 and 12108.36 cm^{-1} can be attributed to the most prominent transition centred at 12108.32 cm^{-1} indicated red in figure 4b. In this spectral region, 51.0 % of the spectral weight of this transition is located. Finally, the resulting data was low-pass filtered using a weighted parabolic averaging, including data points of the preceding five minutes.

3.3 Indoor comparison

The comparison of both spectroscopic sensors was performed in a temperature and humidity controlled laboratory room at MIKES. The two measurement systems were positioned at the opposite ends of a 30 m interferometry rail used for the calibration of distance measuring devices. A double-pass scheme was used for both systems resulting in a 67 m path length. Four Vaisala HMP45AL sensors, typical capacitive environmental sensors in length metrology, were deployed as reference humidity sensors. They were calibrated against a MBW 373 dew point meter before the comparison. The traceability of the comparison was ensured by calibration of the MBW 373 against the MIKES primary dew-point temperature standard MDFG [41, 42] with an expanded uncertainty of 0.06 °C. The expanded uncertainty in MBW 373 corresponds to approximately 4 Pa of uncertainty in water vapor pressure or 0.17 % in relative humidity at 19.9 °C and 40 % RH.The ambient pressure was measured by an external pressure sensor (Vaisala PTB-200). The average reference temperature over the path length was deduced from an ensemble of eight calibrated Pt-100 sensors spaced evenly along the measurement path.

The performance of the devices was studied for changing temperature and humidity, with a particular interest in the dynamic behaviour of the sensors. The response times of the deployed humidity and temperature sensors are of the order of one minute, for the data of the optical sensors smoothing algorithms based on data of the previous minutes were used. The humidity step was performed continuously over hours, the gradient not exceeding approximately 0.4 % RH per minute. Besides temporal variations, also spatial inhomogeneities can occur due to the long distance of 65 m. Therefore, the experiment was designed to minimize the impact of local gradients of temperature and humidity. In the laboratory, fresh air is injected relatively homogeneously from the ceiling by the air conditioning system. The air flow and, thus, also local gradients in temperature and humidity are

therefore primarily oriented from ceiling to floor. Due to the fast air exchange rate in the facility [43], however, these vertical gradients are negligible as compared to the induced changes over 3 hPa in humidity. Nevertheless, the temperature sensors and optical probes were aligned so that the vertical separation of the probes of all experiments remained below 40 cm for the whole path length. The capacitive humidity sensors were placed approximately 1.5 m above the optical axis. The homogeneity along the experimental axis was demonstrated in a separate experiment described in reference [24]. The effective temperature deduced by the ensemble of the Pt-100 sensors was compared to the temperature probed by an optical spectroscopic thermometer, sensitive to the effective temperature along the complete beam path in similar geometry. The agreement was found to be within a few millikelvins for temperature steps around 20°C [24]. During the comparison, the differences in the readings of the individual temperature and humidity sensors along the optical axis remained smaller than 0.3 K and 0.2 hPa even when the conditions were changed. Nevertheless, small and short perturbations due to personnel in the laboratory could not completely be excluded during the complete 65 hour experiment as the facility could not be completely closed during the whole time.

3.4 Calibration

In order to achieve an agreement in absolute value with the calibrated reference humidity sensors of 4 % in relative humidity, it was necessary to calibrate the line strength *S* to deploy the model equations. This can be explained by several reasons. On one hand, the relative uncertainty of the parameters given in the HITRAN database is estimated to be of the order of 5 %-10% [36]. Furthermore, the quality of the absorption signal in the PTB set-up is strongly dependent on the wavelength dependent absorption of individual optical components. Though both set-ups were designed to avoid beam clipping in any of the apertures, dependencies on alignment remain inevitable. Furthermore, in the outdoor measurements contamination of the optics could not be avoided, resulting in aditional absorbance. To deal with all of these problems, calibrated reference sensors were used on site for calibration. The "effective" value for *S* was deduced by calibration of model parameters to the reference values. The scaling factors were applied to the complete datasets. Thus, relative changes of humidity are scaled accordingly and provide evidence for the validity of the recalibration.

4. Results

4.1 Comparison of instruments

The humidity comparison was performed for approximately 65 hours at MIKES. In this facility, it is possible to change humidity and temperature independently. Three different conditions were simulated during the experiment: stable environment, change of humidity, and change of temperature. Ambient pressure was between 990 hPa and 1010 hPa for the whole measurement period. The ambient temperature was stabilized at 19.9 °C during the whole 65 h period, except for the ±500 mK steps around the 45 hour mark. The humidification of the incoming air was stopped and then restarted to change the humidity between 20 and 30 hours. Figure 5a gives a survey on the complete experiment. The average of four capacitive humidity sensors is treated as a reference and depicted as dashed lines. The equivalent of a 4 % deviation from this reference value is indicated by a shaded band around the reference value. The humidity sensors were calibrated during the stability measurement against the dew point mirror whose response time turned out insufficient for the dynamic comparisons. The spectroscopic data of both devices was analysed as discussed above. The humidity step is zoomed out in figure 5b.
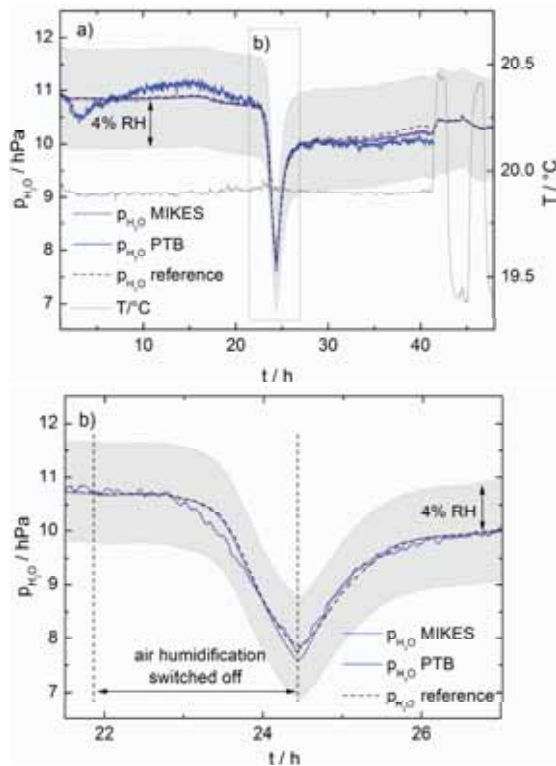
Figure 5. a) Course of comparison. Three different scenarios were investigated: stability, change of humidity, change of temperature. The course of ambient temperature is given in the right scale. b) Zoom in humidity step. Amplitude and dynamics of all sensor systems agree within 4 % relative humidity.

The signal of the initial 15 hours during which the ambient conditions were kept constant was used to deduce the correction for the line strength parameter S. The HITRAN value had to be increased by 2.9 % in the case of the PTB sensor, a value well within the claimed accuracy of the database. Over the whole period of 65 hours, the average deviation from the reference sensor amounts to 0.14 hPa and remains all the time within the 4% deviation band. When changing the humidity, the PTB sensor depicts an earlier onset of the change in humidity than the other two sensor systems as can be seen in figure 5b. The amplitude of the change is in excellent agreement with the reference sensor. In its asymptote, however, the PTB sensor observes a slightly lower level of humidity than the reference and the MIKES sensor. The signal, however, remains well within the 4 % uncertainty band defined by the reference system. In the last phase of the comparison, problems with the automatic direction control occurred which could not be solved within the time of the comparison. Therefore, the PTB data points are missing for this phase.

Similarly to the approach of PTB, the MIKES sensor was calibrated using a fit of the measurement data obtained during the 15 hour stable period in the beginning of the measurement period show in 5 a. The value of the line intensity was increased by 14 % as compared to the database value. It should be noted that this correction also includes the possible errors of the linewidth parameters, which were taken directly from the database. The developed sensor was found to be accurate except for the 10 hour period before the temperature changes. The spectroscopically determined partial pressure was approximately 0.1 hPa lower than the value obtained from the reference sensors right before the first

temperature change. This corresponds approximately to a difference of 0.3 % in relative humidity. During this period the noise was also slightly higher as compared to the average noise over the whole measurement period. The average deviation (RMS) from the reference sensors for a 21 hour period just before the ambient humidity change at 23 hour mark was 0.009 hPa. The averaging time of the MIKES humidity sensor was 38 s. Without using the correction to the total linewidth due to varying water concentration based on equation 3, the minimum measured partial pressure value close to 24.5 hour mark would be 0.1 hPa higher. The varying temperature at the end of the measurement period did not cause significant changes in the measured partial pressure. No changes were made to the MIKES set-up during the measurement period.

The results of the three different phases of the experiment allow conclusions on the performance of all three sensor systems. The stationary phase of the experiment served two purposes: for once, it is used to investigate the stability of the optical set-ups. The MIKES system which is permanently installed in the respective facility shows an excellent stability throughout the complete comparison. The initial problems of the PTB sensor were due to instabilities of the laser source which settled in the course of the experiment. Continuous mode-hop free long-term stability of the source was achieved after approximately 18 hours in the laboratory. For the deployment of the device outdoors this implies that constant surveillance of the performance of the source is necessary. Furthermore, the respective data was used to derive the recalibration of the literary values of the line strength parameters S. As argued in section 3.4, this calibration is necessary due to both experimental influences and the uncertainty of the literature values.

The validity of this recalibration can be seen in the second phase of the experiment in which the humidity of the facility was slowly decreased. Overall, all experiments agree very well within the targeted 4 % uncertainty band. The small deviations in amplitude and onsets can be assigned to different response times of the sensors and also, smaller local gradients due to the air flow from ceiling to floor. The reference sensor system is the system with the largest response time of the three hygrometers. Nevertheless, as discussed in section 3.3 the transient in humidity was chosen so that the response time of the instrument is small enough that the change is within the uncertainty of the sensor system.

The third phase of the experiment, the temperature step was both again a test on stability but also demonstrates the sensitivity of the optical probe to the number density of water molecules. The latter quantity is unchanged by a change in temperature. The MIKES sensor indeed does not show a response to the changing environmental conditions. Unfortunately, the PTB sensor failed this stability test. The responsible beam guiding unit was therefore modified for the outdoor measurements.

4.2 Outdoor measurements
The MIKES measurements in outdoor environment were conducted simultaneously with temperature measurements at the Nummela baseline of the Finnish Geodetic Institute (FGI) [24]. The measurement set-up, except for the measurement head, was kept inside the baseline hut, while the measurement head was positioned outdoors under a waterproof roof with no temperature control. Ten Pt-100 sensors were used as a reference with approximately equidistant spacing and close proximity to the laser beam. A total path length of 130 m with double pass scheme was used for the measurements. An eight hour humidity measurement is shown in figure 6. A sample time of 135 s was chosen in order to enable a simultaneous spectroscopic measurement of the temperature. One Vaisala PTU200 was used as reference humidity sensor. The reference humidity values were logged manually and are marked with open circles in figure 6 during the first 2.5 hours. In this initial period, the reference values are approximately 2 % lower than the spectroscopically measured humidity. This deviation corresponds
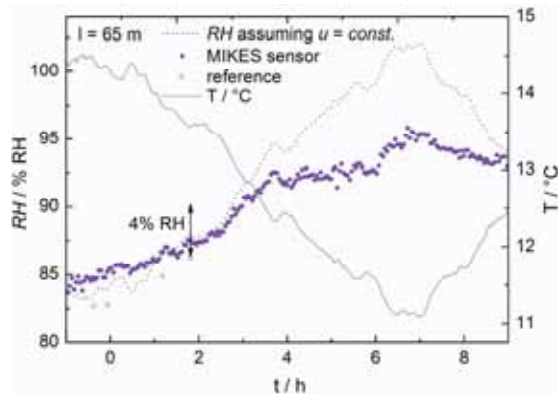
Figure 6. Outdoor measurements as performed with the MIKES spectroscopic sensor in comparison to capacitive reference sensors. The spectroscopic temperature was measured simultaneously, which increased the sample time considerably.

roughly to a 0.15 hPa difference in partial pressure. Beyond 2 hours, no more reference values could be taken as the baseline had to be vacated at night. Statistical filtering was deployed to remove erroneous data points due to falling leaves and flying insects from the optical data.

The PTB optical sensor was investigated in outdoor environment at the geodetic baseline at Innsbruck [44]. The spectroscopic head (comp. figure 3a) was integrated into a four wavelength interferometer to form a refractivity compensated interferometer capable to measure geodetic lengths [45]. The head was placed in front of the first pillar on a standard Leica tripod. A plastic roof above the set-up served as improvised rain and sun protection. The beam preparation unit (figure 3b) was installed in a van parked 5 m away from the spectroscopic head. Thus, there was no possibility to control the ambient conditions under which both systems had to work. The ambient conditions on site were particularly challenging as the baseline is located next to a highway, cars and trucks frequently passing by within a distance of 5 m to beam and equipment. In order to deal with these problems, the number of acquired spectra per observation was increased to 60 spectra, and the observations were repeated every 20 s. The enlarged amount of raw data was then filtered to identify outliers, e.g. caused by dust particles blown into the optical path by passing trucks. Therefore, each single analyzed spectrum was compared to its neighbouring six spectra. In case the standard deviation of this subset exceeded 5.0 % RH, the respective spectrum was discarded. The mean values of each single measurement were furthermore smoothed using a weighted average over the previous five measurements, i.e. approximately the previous 100 s. In figure 7 a data set taken over a distance of 272 m, i.e. an optical absorption path of 544 m is depicted. The duration of the measurement of approximately 14 minutes is determined by the duration of a single length measurement to which it was taken in parallel. As reference, three commercial capacitive humidity sensors (2 Vaisala HMP155, 1 Testo 650) were distributed evenly along the absorption path. Their mean value is given as a dashed line in figure 7. The temperatures were measured using a network of seven Pt-100 sensors distributed along the along the optical path. Because of the longer distance as compared to the comparison, the absorption line at 12113.88 cm^{-1} (comp. table 1) was deployed for the measurement. In this case, an analysis of the complete spectrum around the transition was possible. The line strength S was calibrated by fitting the first five data points in figure 7 to the respective reference value. A reduction of 23 % compared to the literature value of the line strength was necessary. This large deviation can be
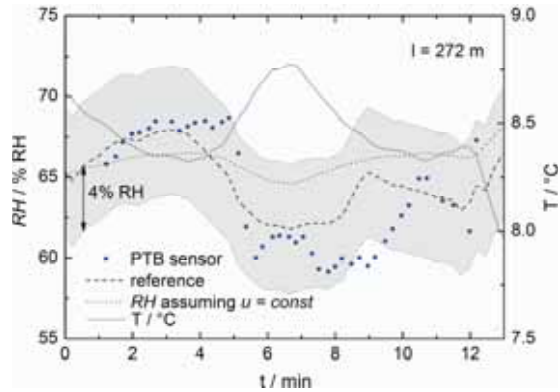
Figure 7. Outdoor measurements performed with the PTB optical sensor in comparison to capacitive reference ensemble. Both sensor systems agree within 4 % RH. The deviations can be explained by the fact that the optical measurement is integrating over the complete optical path, while the reference sensor system measures only at three points.

explained besides inaccuracies of the HITRAN database also in part by inevitable contamination of the optical components in the difficult environment. The recalibrated data are depicted as blue dots in figure 7. During the observation interval, the optical and reference sensor agree qualitatively, the optical data appearing to be slightly shifted. Quantitatively, the deviation remains most of the time within 4 % RH. But it should be noted that the change in humidity around 5 minutes is approximately 40 % larger in the optical measurement compared to the reference measurement. Both deviations, delay and quantitative disagreement, can be explained by the fact that the two measurements do not measure the same quantity. While the three capacitive sensors measure the humidity at three points, the optical measurement simultaneously integrates the water contents along the beam path.

Finally, it should be noted that not only the relative humidity, but also the partial pressure e and, physically most importantly, the number density u of the water molecules change during the depicted experiments. As a consequence of equation (4), the relative humidity RH and temperature T are correlated. In the Hardy-Wexler approximation of the saturation pressure e_{sat} the relative humidity RH changes in first order by -5.1 % RH and -4.2 % RH for a temperature change of 1 K, assuming constant water molecule number density u the ambient conditions in figures 5 and 6. Nevertheless, the observed changes in humidity cannot solely be attributed to changes in the temperature alone. The dotted lines in figures 5 and 6 were calculated assuming u to be constant and identical to the initial value over the complete measurement time. In both cases, the measured value of the relative humidity is significantly smaller than this "projected" value. As an example, the number density u was deduced from the results of the PTB measurements at Innsbruck (figure 7) which were performed in an extremely unstable, fast-changing environment. Figure 8 demonstrates that the temperature-independent number density u changes in qualitative agreement with the measured relative humidity. Quantitatively the number density varies over 12.8 % within the twelve minutes of measurement.
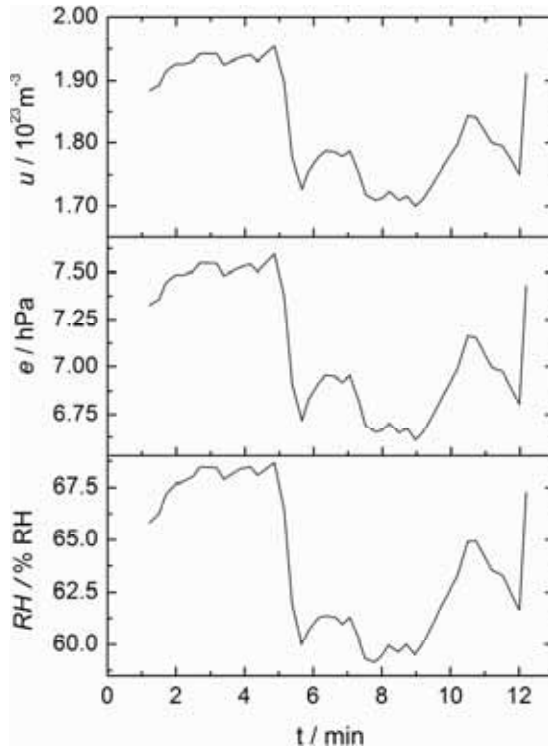
Figure 8. Separation of temperature and humidity influences. Both partial pressure e and number density u of the water molecules change significantly during the outdoor measurement depicted in figure 7.

5. Conclusions

Two different optical hygrometers were realized and their performance was systematically investigated in this study. Both optical hygrometers are based on quantitative absorption spectroscopy, using different observables for the measurement. To validate the developed devices, they were compared to each other and to an independent traceably calibrated sensor network under controlled ambient conditions. The reference sensor network was composed by several localized capacitive sensors, the standard probes for humidity in length metrology.

To achieve quantitative agreement, the optical hygrometers had to be calibrated in advance. Particularly in the case of weaker absorption lines, it is obviously not possible to rely solely on literature values of the absorption strength. The measurement path length and the partial pressure of water were measured with high precision using conventional sensors. To reach an agreement with the spectroscopically measured humidity, the line strengths had to be adjusted in some cases by more than 10%. This leads us to believe that the uncertainty of HITRAN values is likely higher than expected.

After calibration, the comparison has shown that the optical hygrometers agree well with the traceable capacitive sensors. Under slowly-changing laboratory conditions the quantitative agreement of all three systems is significantly better than the targeted 4 % RH. Thus, it has been demonstrated that the developed spectrometers are indeed sufficiently sensitive to small, but also larger changes in the absorbance signal for a relatively large measurement volume. Furthermore, one can conclude that the deployed absorption and analysis models are sufficiently accurate for the targeted measurement

uncertainty. It should be noted that this positive conclusion on the performance of the optical hygrometers is not strictly limited to the range of the tested ambient conditions. By selecting appropriate absorption lines of suitable absorption strengths, similar absorption conditions can be achieved for a completely different humidity or a different absorption length. Thus, in conclusion, this result justifies the application of the optical systems outdoors.

Both systems were then deployed to outdoor measurements up to several hundreds of meters, integrated into advanced distance meters and thermometers. Despite the difficult environmental conditions, both research set-ups performed well at outdoor environment. In contrast to indoor conditions, fast changes in humidity and temperature had to be monitored there. Again, their performance was compared to traceable standard humidity sensors in length metrology. In the extremely harsh environment with fast changing local gradients at the geodetic baseline at Innsbruck, significant deviations between capacitive and optical sensors can be observed. Given the experience of the indoor comparisons, it appears reasonable to assume that these deviations are real. The results clearly demonstrate the benefit of the optical method: The measured quantity in the optical hygrometers is indeed the integral effective humidity rather than the average humidity derived from a number of point sensors. The differences between these two quantities are for longer distances obviously no longer negligible if highest accuracies in length measurement are required.

References
[1] Kim S W 2009 Metrology: Combs rule *Nat. Photon.* **3** 313-314
[2] Minoshima K and Matsumoto H 2000 High-Accuracy Measurement of 240-m Distance in an Optical Tunnel by use of a Compact Femtosecond Laser *Appl. Opt.* **39** 5512-5517
[3] Schuler N, Salvadé Y, Lévêque S, Dändliker R and Holzwarth R 2006 Frequency-comb-referenced two-wavelength source for absolute distance measurement *Opt. Lett.* **31** 3101-3103
[4] Coddington I, Swann C, Nenadovic L and Newbury N 2009 Rapid and precise absolute distance measurements at long range *Nat. Photon.* **3** 351-356
[5] Balling P, Kren P, Masika P and van den Berg S A 2009 Femtosecond frequency comb based distance measurement in air *Opt. Express* **17** 9300-9313
[6] Doloca N R, Meiners-Hagen K, Wedde M, Pollinger F and Abou-Zeid A 2010 Absolute distance measurement system using a femtosecond laser as a modulator *Meas. Sci. Technol.* **21** 115302
[7] Stone J A, Stejskal A and Howard L 1999 Absolute Interferometry with a 670-nm External Cavity Diode Laser *Appl. Opt.* **38** 5981-5994
[8] Kinder T and Salewski K D 2002 Absolute distance interferometer with grating-stabilized tunable diode laser at 633 nm *J. Opt. A* **4** S364-S368
[9] Yang H J, Deibel J, Nyberg S and Riles K 2005 High-precision absolute distance and vibration measurement with frequency scanned interferometry *Appl. Opt.* **44** 3937-3944
[10] LeFloch S, Salvadé Y, Mitouassiwou R and Favre P 2008 Radio frequency controlled synthetic wavelength sweep for absolute distance measurement by optical interferometry *Appl. Opt.* **47** 3027-3031

[11] Pollinger F, Meiners-Hagen K, Wedde M and Abou-Zeid A 2009 Diode-laser-based high-precision absolute distance interferometer of 20 m range *Appl. Opt.* **48** 6188-6194

[12] Azouigi S, Badr T, Wallerand J P, Himbert M, Salgado J and Juncar P 2010 Transportable distance measurement system based on superheterodyne interferometry using two phase-locked frequency-doubled Nd:YAG lasers *Rev. Sci. Instr.* **81** 053112

[13] Wallerand J P *et al.* 2008 Towards new absolute long-distance measurement in air *NCSL Int. Workshop and Symp. (Orlando, USA)* http://www.longdistanceproject.eu/files/towards new absolute.pdf

[14] Peggs G N, Maropoulos P G, Hughes E B, Forbes A B, Robson S, Ziebart M and Muralikrishnan B 2009 Recent developments in large-scale dimensional metrology *Proc. Inst. Mech. Eng. B: J. Eng. Man.* **223** 571-595

[15] Edlén B 1966 The Refractive Index of Air *Metrologia* **2** 71-80

[16] Bönsch G and Potulski E 1998 Measurement of the refractive index of air and comparison with modified Edlén's formulae *Metrologia* **35** 133-139

[17] Ciddor P E 1996 Refractive index of air: new equations for the visible and near infrared *Appl. Opt.* **35** 1566-1573

[18] Korpelainen V and Lassila A. 2004 Acoustic method for determination of the effective temperature and refractive index of air in accurate length interferometry *Opt. Eng.* **43** 2400-2409

[19] Arroyo M P and Hanson R K 1993 Absorption measurements of water-vapor concentration, temperature, and line-shape parameters using a tunable InGaAsP diode laser *Appl. Opt.* **31** 6104-6116

[20] Silver J A and Kane D J 1999 Diode laser measurements of concentration and temperature in microgravity combustion *Meas. Sci. Technol.* **10** 845-852

[21] Teichert H, Fernholz T and Ebert V 2003 Simultaneous In Situ Measurement of CO, H_2O, and Gas Temperatures in a Full-Sized Coal-Fired Power Plant by Near-Infrared Diode Lasers *Appl. Opt.* **42** 2043-2051

[22] Shao J, Lathdavong L, Kluczynski P, Lundqvist S and Axner O 2009 Methodology for temperature measurements in water vapor using wavelength-modulation tunable diode laser absorption spectrometry in the telecom C-band *Appl. Phys. B* **97** 727-748

[23] Hiéta T and Merimaa M 2010 Spectroscopic Measurement of Air Temperature *Int. J. Thermophysics* **31** 1710-1718

[24] Hiéta T, Merimaa M, Vainio M, Seppä S and Lassila A 2011 Air refractive index compensation using laser spectroscopy *accepted by Appl. Opt. (Doc. ID 146931)*

[25] Earnshaw K B and Hernandez E N 1972 Two-Laser Optical Distance-Measuring Instrument that Corrects for the Atmospheric Index of Refraction *Appl. Opt.* **11** 749-754

[26] Matsumoto H and Honda T 1992 High-accuracy length-measuring interferometer using the two-colour method of compensating for the refractive index of air *Meas. Sci. Technol.* **3** 1084-1086

[27] Meiners-Hagen K and Abou-Zeid A 2008 Refractive index determination in length measurement by two-colour interferometry *Meas. Sci. Technol.* **19** 084004

[28] Werle P 1998 A review of recent advances in semiconductor laser based gas monitors *Spectrochimica Acta Part A: Molecular and Biomolecular Spectroscopy* **54** 197-236

[29] Silver J A and Hovde D C 1998 A Comparison of Near-Infrared Diode Laser Techniques for Airborne Hygrometry *Journal of Atmospheric and Oceanic Technology* **15** 29-35

[30] Schirmer B, Venzke H, Melling A, Edwards C S, Barwood G P, Gill P, Stevens M, Benyon R and Mackrodt P 2000 High precision trace humidity measurements with a fibre-coupled diode laser absorption spectrometer at atmospheric pressure *Meas. Sci. Technol.* **11** 382-391

[31] Fried A, Diskin G, Weibring P, Richter D, Walega J, Sachse G, Slate T, Rana M and Podolske J 2008 Tunable infrared laser instruments for airborne atmospheric studies *Appl. Phys. B* **92** 409-417

[32] Sonnenfroh D, Kessler W, Magill J, Upschulte B, Allen M and Barrick J 1998 In-situ sensing of tropospheric water vapor using an airborne near-IR diode laser hygrometer *Appl. Phys. B* **67** 275-282

[33] Gurlit W, Zimmermann R, Giesemann C, Fernholz T, Ebert V, Wolfrum J, Platt U and Burrows J P 2005 Lightweight diode laser spectrometer CHILD (Compact High-altitude In-situ Laser Diode) for balloonborne measurements of water vapor and methane *Appl. Opt.* **44** 91-102

[34] Durry G, Amarouche N, Joly L, Liu X, Parvitte B and Zéninari V 2008 Laser diode spectroscopy of H_2O at 2.63µm for atmospheric applications *Appl. Phys. B* **90** 573-580

[35] Rothman L S *et al.* 1998 The HITRAN molecular spectroscopic database and HAWKS (HITRAN atmospheric workstation): 1996 edition *J. Quant. Spectrosc. Ra.* **60** 665-710

[36] Rothman L S *et al.* 2009 The HITRAN 2008 molecular spectroscopic database *J. Quant. Spectrosc. Ra.* **110** 533-572

[37] Buck A L 1981 New Equations for Computing Vapor Pressure and Enhancement Factor *J. Appl. Meterology* **20** 1527-1532

[38] Hardy B 1998 ITS-90 formulations for vapor pressure, frostpoint temperature, dewpoint temperature, and enhancement factors in the range -100 To 100 C *Proc. Third Int. Symp. Humidity and Moisture*, 214-221

[39] Liu Y, Lin J, Huang G, Guo Y and Duan C 2001 Simple empirical analytical approximation to the Voigt profile *J. Opt. Soc. Am. B* **18** 666-672

[40] Allen M G, Carleton K L, Davis S J, Kessler W J; Otis C E, Palombo D A and Sonnenfroh D M 1995 Ultrasensitive dual-beam absorption and gain spectroscopy: applications for near-infrared and visible diode laser sensors *Appl. Opt.* **34** 3240-3249

[41] Heinonen M and Uusipaikka L An apparatus for testing humidity sensors at low temperatures *in Proc. Tempmeko 2004, Vol. 1 ed. by D. Zvizdic (LPM/FSB, Zagreb, 2005)* 669-675

[42] Heinonen M *et al.* 2011 Investigation of the Equivalence of National Dew-Point Temperature Realizations in the -50 °C to + 20 °C Range *Int. J. Thermophys.*, DOI 10.1007/s10765-011-0950-x, 1-16

[43] Lassila A *et al.* 2011 Design and performance of an advanced metrology building for MIKES *Measurement* **44** 399-425

[44] Jokela J, Häkli P, Kugler R, Skorpil H, Matus M and Poutanen M 2010 Calibration of the BEV Geodetic Baseline, *FIG Congress 2010*

[45] Meiners-Hagen K, Köchert P and Abou-Zeid A 2011 A Multiwavelength Interferometer for Geodetic Lengths *10th IMEKO Symp. Laser Metrology for Precision Measurement and Inspection in Industry (LMPMI) 2011: (VDI-Berichte 2156)* 297-302

MIKES
Mittatekniikan keskus
Centre for metrology
and accreditation